

Washington University in St. Louis

## Washington University Open Scholarship

---

All Theses and Dissertations (ETDs)

---

5-24-2011

### Information Processing for Biological Signals: Application to Laser Doppler Vibrometry

Alan Kaplan

*Washington University in St. Louis*

Follow this and additional works at: <https://openscholarship.wustl.edu/etd>

---

#### Recommended Citation

Kaplan, Alan, "Information Processing for Biological Signals: Application to Laser Doppler Vibrometry" (2011). *All Theses and Dissertations (ETDs)*. 890.

<https://openscholarship.wustl.edu/etd/890>

This Dissertation is brought to you for free and open access by Washington University Open Scholarship. It has been accepted for inclusion in All Theses and Dissertations (ETDs) by an authorized administrator of Washington University Open Scholarship. For more information, please contact [digital@wumail.wustl.edu](mailto:digital@wumail.wustl.edu).

WASHINGTON UNIVERSITY IN ST. LOUIS  
School of Engineering and Applied Science  
Department of Electrical & Systems Engineering

Dissertation Examination Committee:

Dr. Joseph A. O'Sullivan, Chair

Dr. R. Martin Arthur

Dr. Robert E. Morley

Dr. Arye Nehorai

Dr. John W. Rohrbaugh

Dr. Erik Sirevaag

INFORMATION PROCESSING FOR BIOLOGICAL SIGNALS: APPLICATION  
TO LASER DOPPLER VIBROMETRY

by

Alan D. Kaplan

A dissertation presented to the Graduate School of Arts and Sciences  
of Washington University in partial fulfillment of the  
requirements for the degree of

DOCTOR OF PHILOSOPHY

May 2011  
Saint Louis, Missouri

copyright by  
Alan D. Kaplan  
2011

## ABSTRACT OF THE DISSERTATION

Information Processing for Biological Signals: Application to Laser Doppler

Vibrometry

by

Alan D. Kaplan

Doctor of Philosophy in Electrical Engineering

Washington University in St. Louis, May 2011

Research Advisor: Dr. Joseph A. O'Sullivan

Signals associated with biological activity in the human body can be of great value in clinical and security applications. Since direct measurements of critical biological activity are often difficult to acquire noninvasively, many biological signals are measured from the surface of the skin. This simplifies the signal acquisition, but complicates post processing tasks. Modeling these signals using the underlying physics may not be accurate due to the inherent complexities of the human body. The appropriate use of such models depends on the application of interest. Models developed in this dissertation are motivated by underlying physiology and physics, and are capable of expressing a wide range of signal variability without explicitly invoking physical quantities.

An approach for the processing of biological signals is developed using graphical models. Graphical models describe conditional dependence between random variables

on a graph. When the graph is a tree, efficient algorithms exist to compute sum-marginals or max-marginals of the joint distribution. Some of the variables correspond to the measured signal, while others may represent the hidden internal dynamics that generate the observed data. Three levels of hidden dynamics are outlined, which enable models to be constructed that track internal dynamics on differing time scales. Expectation maximization algorithms are used to compute parameter estimates.

Experimental results of this approach are presented for a novel method of recording bio-mechanical activity using a Laser Doppler Vibrometer. The LDV measures surface velocity on the basis of the Doppler shift. This device is targeted on the neck overlying the carotid artery, and the proximity of the carotid to the skin results in a strong signal. Vibrations and movements from within the carotid are transmitted to the surface of the skin, where they are sensed by the LDV. Changes in the size of the carotid due to variations in blood pressure are sensed at the skin surface. In addition, breathing activity may be inferred from the LDV signal.

Individualized models are evaluated systematically on LDV data sets that were acquired under resting conditions on multiple occasions. Model fit is evaluated both within and across recording sessions. Model parameters are interpreted in terms of the underlying physiology. Pressure wave physics in a series of elastic tubes is presented to explore the underlying physics of blood flow in the carotid. Mechanical movements of the carotid walls are related to the underlying pressure, and therefore the cardiovascular activity of the heart and vasculature. This analysis motivates a model that can be estimated from experimental data. Resulting models are interpreted for the LDV signal.

The graphical models are applied to the problem of identity verification using the LDV signal. Identity verification is an important problem in which the claimed identity is either accepted or rejected by an automated system. The system design that is used is based on a loglikelihood ratio test using models that are trained during an enrollment phase. A score is computed and compared to a threshold. Performance is given in the form of False Nonmatch and False Match empirical error rates as a function of the threshold. Confidence intervals are computed that take into account correlations between the system decisions.

# Acknowledgments

I offer thanks to my advisor, Professor Joseph O’Sullivan. Under his guidance and direction I have advanced my intellectual talents tremendously. His breadth and depth of knowledge is inspiring. The group in which I did this work is an exceptional set of engineers and scientists. All of them have contributed to this work, and my development as a researcher. Dr. John Rohrbaugh has been a major part of my experience over the past few years. His expertise and work rate is remarkable. I also thank Dr. Erik Sirevaag for his support, contribution, and display of scientific professionalism.

I thank the members of my committee for their time and attention: Dr. Joseph O’Sullivan, Dr. John Rohrbaugh, Dr. Robert Morley, Dr. R. Martin Arthur, Dr. Arye Nehorai, and Dr. Erik Sirevaag.

The students that I have worked with and shared thoughts with played an important role in the development of the ideas that form this work. A partial list includes Mei Chen, Po-Hsiang Lai, Ikenna Odinaka, and Michael Walker.

Other members of our group, including Dr. Sean Kristjansson, Kenji Truman, Amanda Kay Sheffield, and the technical staff make this undertaking possible.

None of this would be possible without the support and encouragement from my family: Susannah, my parents, my brother and sister, my grandmother, and my uncle.

This work has been supported in part by the Technical Support Working Group, contract number W91CRB-04-C-0030.

Alan D. Kaplan

*Washington University in Saint Louis*  
*May 2011*

To my grandfather.



# Contents

<b>Abstract</b> . . . . .	<b>ii</b>
<b>Acknowledgments</b> . . . . .	<b>v</b>
<b>List of Tables</b> . . . . .	<b>x</b>
<b>List of Figures</b> . . . . .	<b>xi</b>
<b>List of Abbreviations</b> . . . . .	<b>xv</b>
<b>List of Notations</b> . . . . .	<b>xvi</b>
<b>1 Introduction</b> . . . . .	<b>1</b>
1.1 The Individuals and the States . . . . .	2
1.2 Identity Verification and Biological Signal Modeling . . . . .	6
1.3 Laser Doppler Vibrometry . . . . .	7
1.4 Outline and Contributions . . . . .	8
<b>2 Graphical Models and Algorithms</b> . . . . .	<b>11</b>
2.1 Some Definitions from Graph Theory . . . . .	13
2.2 Random Vectors and Conditional Independence . . . . .	15
2.3 Graphical Models . . . . .	16
2.4 Algorithms for Graphical Models on Trees . . . . .	18
2.4.1 Computing Marginal Distributions . . . . .	20
2.4.2 Computing the Mode . . . . .	21
2.4.3 Inference on a Hidden Markov Model . . . . .	22
2.4.4 Inference on Nested Hidden Markov Models . . . . .	25
<b>3 Models for Biological Signals</b> . . . . .	<b>28</b>
3.1 Biological Signals . . . . .	29
3.1.1 Examples of Biological Signals . . . . .	30
3.1.2 Applications for Biological Signals . . . . .	33
3.2 Motivation for a Structured Modeling Framework . . . . .	37
3.3 Notation for the Data . . . . .	39
3.4 State Based Modeling . . . . .	40
3.5 Models . . . . .	43
3.5.1 Pulse Model (A) . . . . .	45

3.5.2	Pulse Model (B)	46
3.5.3	Pulse Model (C)	46
3.5.4	Session Model (D)	48
3.5.5	Multisession Model (E)	50
<b>4</b>	<b>Laser Doppler Vibrometry Measurements of the Carotid Pulse</b>	<b>52</b>
4.1	Data Acquisition	53
4.2	Biological Basis	54
4.3	Signal	55
4.4	Preprocessing	59
<b>5</b>	<b>Experimental Evaluation of Models for Laser Doppler Vibrometry</b>	<b>62</b>
5.1	Model $LDV_A$	66
5.2	Model $LDV_B$	66
5.3	Model $LDV_C$	68
5.3.1	Interpretation of Model $LDV_C$	68
5.4	Model $LDV_{BD}$	74
5.4.1	Interpretation of Model $LDV_{BD}$	74
5.4.1.1	Model parameters	78
5.4.1.2	State sequences	79
5.4.1.3	Estimating respiration rate	80
5.4.1.4	Discussion	89
<b>6</b>	<b>Wave Propagation in Elastic Tubes: Analysis and Models</b>	<b>93</b>
6.1	Pressure Waves in Elastic Tubes	95
6.1.1	Conservation of Mass and the Navier-Stokes Equations	95
6.1.2	Simplifications	96
6.1.3	One Dimensional Wave Equation	97
6.1.4	Primary Reflection	99
6.1.5	Pressure in a Tree Structure	100
6.2	Models	101
6.2.1	Model Description	102
6.2.2	Estimation of Parameters	103
6.3	Application to LDV	106
6.3.1	Pressure-Radius Relationship	107
6.3.2	State Effects	109
6.3.3	Adjustments for Widening	112
<b>7</b>	<b>Identity Verification Using Laser Doppler Vibrometry</b>	<b>117</b>
7.1	Motivation	119
7.2	System Design and Performance Prediction	121
7.2.1	Error Rates	121
7.2.2	Confidence Intervals	124

7.2.3	LDV . . . . .	128
7.3	Models $LDV_B$ and $LDV_{BD}$ . . . . .	129
7.4	Cepstral HMM . . . . .	135
7.4.1	Background . . . . .	135
7.4.2	Results . . . . .	136
<b>8</b>	<b>Conclusions and Future Work . . . . .</b>	<b>140</b>
8.1	Future Work . . . . .	142
8.1.1	Modeling for LDV and Biological Signals . . . . .	142
8.1.2	Underlying Physics of LDV Signals . . . . .	143
8.1.3	ID Verification Using the LDV . . . . .	144
<b>Appendix A</b>	<b>Fluid Dynamics . . . . .</b>	<b>146</b>
A.1	Conservation of Mass . . . . .	146
A.2	Navier-Stokes Equations in Cylindrical Coordinates . . . . .	147
<b>Bibliography</b>	<b>. . . . .</b>	<b>151</b>
<b>Vita</b>	<b>. . . . .</b>	<b>161</b>

# List of Tables

3.1	Categorized examples of the underlying properties for biological signals.	42
3.2	Eight model types.	44
5.1	Modeled trained and tested on LDV data.	62
5.2	Training and testing schedules.	63
5.3	Average model fit in loglikelihood per sample for the 11 training and testing schedules for time domain models.	65
5.4	Confidence intervals for the 11 training and testing schedules for time domain models.	65
7.1	All possible covariances between tests. The indices $a, b, c, d$ are distinct.	126
7.2	Empirical equal error rates for models $LDV_B$ and $LDV_{BD}$ over the 11 training and testing schedules.	133
7.3	FNMRs for set FMRs of 1%, 0.05%, and 0.01%.	134
7.4	Equal error rates with varying window lengths and 2 states. Also, 95% confidence intervals are given for the false nonmatch and false match rates. The overlap indicates the probability of the error rate being lower than that of the best performing model with a window length of 175ms.	137
7.5	Equal error rates with varying number of states using a window length of 175ms. Also, 95% confidence intervals are given for the false nonmatch and false match rates. The overlap indicates the probability of the error rate being lower than that of the best performing model with 3 states.	138

# List of Figures

1.1	Graphs showing the conditional dependence between the individual, $i$ , the state, $x$ , and the data, $d$ for a biometric. In (a), the data are independent of the individual given the state. This is not true for (b).	5
1.2	Intersecting themes of the dissertation. . . . .	8
2.1	Examples of a graphs with four vertices. The graph in (a) has 5 edges: $E_a = \{(1, 2), (2, 1), (1, 4), (2, 3), (4, 4)\}$ . The undirected graph in (b) has 4 edges $E_b = \{(1, 2), (1, 4), (2, 3), (4, 4)\}$ . The graph in (c) is simple and contains 3 edges, $E_c = \{(1, 2), (1, 4), (2, 3)\}$ . . . . .	14
2.2	Graph for a function that factorizes as $f(x_1, x_2, x_3) = g(x_1)g(x_1, x_2)g(x_2, x_3)$ .	20
2.3	A Hidden Markov Model. . . . .	23
2.4	A nested HMM. . . . .	26
3.1	A drawing of the circulatory system. . . . .	31
3.2	Blood pressure recordings of systemic arterial pressure, pulmonary arterial pressure, and central venous pressure. . . . .	32
3.3	Three electrocardiogram channels: (a) lead I, (b), lead II, and (c) lead V. . . . .	34
3.4	A respiration signal. . . . .	35
3.5	Hierarchy of the data. . . . .	41
3.6	HMM topology for Model C. . . . .	49
3.7	HMM topology for Models D and E. . . . .	50
4.1	Ten seconds of three signals recorded simultaneously: (a) carotid LDV signal, (b) ECG, (c) radial blood pressure. . . . .	56
4.2	An LDV velocity pulse and its corresponding LDV displacement pulse. Both have been normalized by their sample means and sample standard deviations. . . . .	57
4.3	Breathing activity in the LDV signal and a strain gauge: (a) an LDV displacement signal over 25 seconds and the low frequency component, (b) a strain gauge measurement over the abdomen. . . . .	58
4.4	The Gaussian, Hamming, and Nuttall windows are shown in (a), and their spectra are shown in (b). . . . .	61
5.1	Histograms across individuals for (a) model $LDV_A - S_{1,1}$ , and (b) model $LDV_A - S_{1,2}$ . The histogram in (c) shows how many more individuals for $LDV_A - S_{1,1}$ there are than $LDV_A - S_{1,2}$ in each score bin. . . . .	67

5.2	Histograms across individuals for (a) model $LDV_B - 1$ , and (b) model $LDV_B - 2$ . The solid red lines indicate the mean score and the dotted red line show a standard deviation away from the mean. The histogram in (c) shows how many more individuals for $LDV_B - 1$ there are than $LDV_B - 2$ in each score bin. . . . .	69
5.3	Means for the best performing individual across sessions for models (a) $LDV_B - S_{1,1}$ and (b) $LDV_B - S_{1,2}$ with several testing pulses. . . . .	70
5.4	Means for the worst performing individual across sessions for models (a) $LDV_B - S_{1,1}$ and (b) $LDV_B - S_{1,2}$ with several testing pulses. . . . .	70
5.5	Mean spectrogram and pulse for an individual. . . . .	71
5.6	The result of the max-product algorithm on a mean pulse is shown in (a), and the state transition probability matrix in shown in (b). . . . .	71
5.7	Examples of pulse segmentation using model $LDV_C$ on 5 seconds of data. The black dotted lines are pulse transition between detections, and the red dotted lines are main peak detections. The estimated heart rates are: (a) 97 bpm, (b) 89 bpm, (c) 65 bpm, (d) 85 bpm, (e) 103 bpm, and (f) 57 bpm. . . . .	75
5.8	Histograms across individuals for (a) model $LDV_{BD} - 1$ , and (b) model $LDV_{BD} - 2$ . The solid red lines indicate the mean score and the dotted red line show a standard deviation away from the mean. The histogram in (c) shows how many more individuals for $LDV_{BD} - 1$ there are than $LDV_{BD} - 2$ . . . . .	76
5.9	HMM mean vectors for two individuals: a) individual A, and b) individual B. . . . .	79
5.10	State transition probabilities for two individuals. a) State transition probability matrix for individual A. b) State transition probability matrix for individual B. . . . .	79
5.11	Strain gauge measurements and optimal state paths for two individuals. Note that two vertical axes are used in these figures. Data occurring before the dotted vertical line were used for training. a) State path and strain gauge measurements for individual A. Data occurring before the dotted vertical line were used for training. b) State path and strain gauge measurements for individual B. . . . .	81

5.12	Example of respiration rate estimation for one individual. In (a), the strain gauge is processed to derived $r_{SG}$ . A total of 6 periods are detected and the rate during this interval is $r_{SG} = 0.131$ Hz. Figure (b) shows the shift function $D(\tau)$ for the same individual. The initial part of the state sequence is shown in (c) along with shifted versions of the sequence corresponding to the minima computed from $D(\tau)$ . Figure (d) shows the state distances used. A shift of 8 pulses was detected and used with a mean IBI of 1.02 s, giving $r_{SS} = 0.123$ Hz. The error for this individual is 6%, which is near the 50th percentile (median). . . . .	85
5.13	DFT of $D(\tau)$ used in computing $r_{SS}$ . A frequency of 0.13 is computed for this individual (same individual in Figure 5.12), giving the estimate $r_{SS} = 0.128$ Hz. . . . .	86
5.14	Scatter plot of $r_{SG}$ vs $r_{SS}$ for the three state model for (a) the local minimum method, and (b) the DFT method. The black line is the set of points for which $r_{SG} = r_{SS}$ . . . . .	86
5.15	Respiration rate performance for the local minimum method. In (a), the algorithm is evaluated in the same 100 pulses used for training the HMMs. In (b), the following 50 pulses are used for estimating respiration rate. . . . .	87
5.16	Respiration rate performance for the DFT method. In (a), the algorithm is evaluated in the same 100 pulses used for training the HMMs. In (b), the following 50 pulses are used for estimating respiration rate. . . . .	88
5.17	PCA analysis for two subjects. The axes for plots (a) and (b) correspond to different principle components, and each of the points represents one pulse. Figures (c) and (d) show the PCA basis vectors for (a) and (b), respectively. . . . .	90
6.1	A generic bifurcating tree. . . . .	94
6.2	Linear approximation error as a function of radius change from 2.85 mm. . . . .	108
6.3	Model results for two subjects. . . . .	108
6.4	Data images for an individual across two sessions. . . . .	109
6.5	Figure (a) shows two pulses from different states, and the the mean pulse. Figure (b) shows the modeled signals from the two states and the mean. . . . .	112
6.6	Model estimates for (a) the mean pulse, (b) state 1, and (c) state 2. . . . .	113
6.7	Examples of LDV displacement pulses. . . . .	114
6.8	Initializations and final converged results of the algorithm for three subjects. The black curves are LDV data, the blue curves are individual waves, and the red curves are the sum of the individual waves. . . . .	116
7.1	An example of stability within session (a), and discriminability across individuals, (b). The pulses are aligned by their main peaks. . . . .	120

7.2	The grand mean LDV pulse used in the null model. . . . .	130
7.3	Empirical FNMR and FMR curves for the $LDV_B - S_{1,1}$ , $LDV_B - S_{1,2}$ , and $LDV_B - S_{12,3}$ systems. . . . .	131
7.4	Performance curves with 95% confidence bands for model (a) $LDV_B - S_{1,1}$ , (b) $LDV_B - S_{1,2}$ , and (c) $LDV_B - S_{12,3}$ . . . . .	132
7.5	Performance curves with 95% confidence bands for model (a) $LDV_{BD} - S_{1,1}$ , (b) $LDV_{BD} - S_{1,2}$ , and (c) $LDV_{BD} - S_{12,3}$ . . . . .	134
7.6	The performance curves for the cepstral HMM and 95% confidence bands. . . . .	139



# List of Abbreviations

BMI	Body Mass Index
ECG	Electrocardiogram
EER	Equal Error Rate
EM	Expectation Maximization
FFT	Fast Fourier Transform
FMR	False Match-Rate
FNMR	False Non-Match Rate
HMM	Hidden Markov Model
IBI	Interbeat Interval
ID	Identity
LDV	Laser Doppler Vibrometry
LTI	Linear Time-Invariant
PDF	Probability Density Function
PCA	Principal Components Analysis
STFT	Short Time Fourier Transform

# List of Notations

$\perp$	Independent
$a \leftrightarrow b$	Path between $a$ and $b$
$f_X(x)$ or $f(x)$	PDF of $X$
$G$	Graph
$V$	Vertex Set
$E$	Edge Set
$m$	Number of training sessions
$\tilde{m}$	Number of testing sessions
$m_{a,b}$	The message function from node $a$ to node $b$
$n$	Number of training pulses per session
$\tilde{n}$	Number of testing pulses per session
$\mathcal{N}(a)$	The neighbors of node $a$
$N$	Number of subjects used for ID verification
$\psi_C$	The clique potential function over node set $C$
$r$	Radial dimension in cylindrical coordinates
$r_m$	FMR
$r_n$	FNMR
$\theta$	Angular dimension in cylindrical coordinates
$x$	Axial dimension in cylindrical coordinates
$\mathcal{X}$	The domain of $x$
$\otimes_{v=1}^m \mathcal{X}_v$	The product space $\mathcal{X}_1 \times \mathcal{X}_2 \times \dots \times \mathcal{X}_m$
$\mathbf{y}$	Testing data
$\tilde{\mathbf{y}}$	Training data
$\mathbf{y}_s$	Data from session $s$
$\mathbf{y}_{s,i}$	Pulse $i$ from session $s$
$\mathbf{y}_{s,i,t}$	Sample $t$ from pulse $i$ from session $s$
$z$	Number of samples per pulse

# Chapter 1

## Introduction

In 1948, as president of the newly founded Biometric Society, R. A. Fisher, stated that Biometry is “... the active pursuit of biological knowledge by quantitative methods ...” [1]. Since then, the field has expanded to incorporate a range of new sensing devices, applications, and processing tools. In light of Fisher’s original statement and subsequent developments, we define biometrics as the science of sensing, quantifying, and processing data which originates from biological activity.

In its singular form, a biometric refers to a collection of three items: a particular sensor, the manner in which it is used to collect biological data, and the data. In this way, for example, we can talk about electrocardiograms (ECG) as a biometric, with the understanding that a complete description would require sensor details, including lead placement.

Applications of biometrics are numerous and diverse, encompassing both clinical and security domains. For example, much work has been done on the use of ECGs for the automated detection of ectopic heart beats. The successful deployment of such technology could have a far reaching impact on the diagnosing and monitoring of

patients, both in and out of the hospital. This is especially true today, given the promise of high performance mobile devices.

The work presented in this dissertation is motivated by, and has been applied to, a novel method for sensing cardiovascular activity using a Laser Doppler Vibrometer (LDV). A major focus of this technology thus far has been its use in the security applications of identity verification, which is seen as a critical component of security systems in general. Many identity verification methods do not utilize biological data, although the exploration of new methods, including LDV, which incorporate data related to cardiovascular activity has increased recently within the scientific community. In addition to the use of LDV for security applications, the technology holds great promise for clinical use, due to the centrality of its measurements to the heart, and the non-contact manner in which the measurements are made. In fact, both the security and clinical general areas of application are complimentary.

## **1.1 The Individuals and the States**

Biometrics, as defined and described above, is a highly important and vibrant area of research. In some ways, data generated from biological systems differ significantly from other classes of signals that electrical engineers typically work with. In the communications field, an area where many of the signal processing and detection techniques in common use originate, the problem is generally that of reconstructing a transmitted signal at another location. Uncertainty in this problem stems primarily from the medium in which the signal is transmitted, and the objective is to recover any damage imparted to the transmitted signal during its transmission. Unlike this

scenario, in biometrics, we often do not have as much knowledge about the mechanisms that generate the signals (the source in the communications problem). This renders many of the former techniques in need of refinement and reinvention for this new class of problems. The wide variety of biological signals can, however, be characterized in useful ways. We may describe a particular biological signal with respect to a particular individual. Within that individual, the signal is dependent on a number of internal states.

Individuality plays a major role in biometrics- ECG or LDV signals acquired from different individuals will likely exhibit varying traits, and may even require separate models and processing tools. This is generally a desirable trait for using biometrics for identity verification. Within an individual, there are many possible dynamic states, often characterized by physiological properties that are not directly measured. The dynamic states are often the quantities of interest in clinical applications. Physiological mechanisms and the laws of physics that govern their dynamics underlie the quantification of biological activity, providing a rich base from which the development of new tools and methods can stem.

In this dissertation, information processing tools are developed for biological signals that are specific to an individual. Models are constructed that track state changes within the individual, but the states alone are not enough to describe the data. The following three random variables may be defined for a biometric:

1.  $d$ : data measured from the sensor.
2.  $x$ : state of the individual.
3.  $i$ : the individual.

The joint Probability Density Function (PDF) is denoted as  $f(i, x, d)$ . In this formulation, the individual and the data are well defined, but the definition of state depends on the application. For example, if the problem is the estimation of some unknown physiological quantity, we may define the state to be this quantity. The specific problem will also motivate the nature of the conditional dependence between the random variables. Two models describing their conditional dependence are shown illustratively as graphs in Figure 1.1. In the figure, the nodes (circles) represent the random variables and the directed edges (arrows) represent condition dependencies, where two nodes connected by an edge are dependent. In Model A, the joint PDF can be factored as

$$\text{Model A: } f(i, x, d) = f(i) f(x|i) f(d|x). \quad (1.1)$$

For this model, the individual is independent of the data given the state. In this way, the states are considered to be common among individuals. With respect to this basic model,

$$f(i|d) \propto f(i) \int_x f(x|i) f(d|x), \quad (1.2)$$

and

$$f(x|d) \propto f(d|x) \int_i f(i) f(x|i). \quad (1.3)$$

In Model B, the joint PDF can be factored as

$$\text{Model B: } f(i, x, d) = f(i) f(x|i) f(d|i, x). \quad (1.4)$$

Unlike the first model, here the individual is not independent of the data given the state. This model may be applicable when the state is not defined in terms of physiological quantities, or when the states are not common among individuals. The models

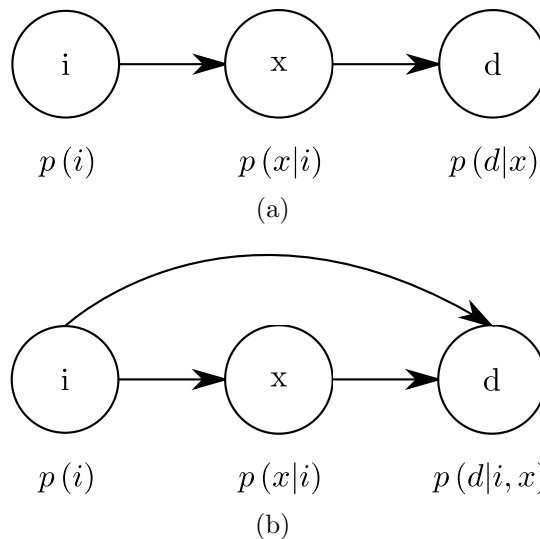


Figure 1.1: Graphs showing the conditional dependence between the individual,  $i$ , the state,  $x$ , and the data,  $d$  for a biometric. In (a), the data are independent of the individual given the state. This is not true for (b).

developed in this dissertation are of this type. With respect to this model,

$$f(i|d) \propto f(i) \int_x f(x|i) f(d|i, x), \quad (1.5)$$

and

$$f(x|d) \propto \int_i f(i) f(x|i) f(d|i, x). \quad (1.6)$$

Two interconnected inference problems in biometrics are highlighted: inference about the individual, and inference about the state of the individual. In most cases, the PDFs associated with either model are not known, and need to be estimated from sample data. This is often done by acquiring a set of data points  $\{i, x, d\}$ , and estimating the parameters associated with a family of PDFs. Greater sample sizes will lead to smaller estimation errors, and consequently improved performance.

The ideas discussed in this introduction are exploited in the development of information processing tools for biometrics. Graphical models are used as a basic framework

from which the tools are developed, not unlike the models described above. A comprehensive modeling approach is applied to LDV data, including a description of fluid flow in distensible tubes.

## 1.2 Identity Verification and Biological Signaling

Identity verification plays an important role within the general context of security [2]. It is fundamentally important to know who is who before further action can be taken. The two types of identity problems are those of identification and verification. In the identification problem, the system needs to ascertain the identity of an individual on the basis of some identity marker that is taken from the individual. In the verification problem, the system uses an identity marker, along with a claimed identity, and must either accept or reject this claimed identity.

Classical examples of identity markers are the fingerprint, handprint, face, and iris [3, 4]. These traits have been proposed for use as identity markers in part because of their presumed stability over time. There is evidence, however, that challenges this assumption for iris images [5, 6].

Recently, the use of biological signals as identity markers has been proposed. Since they are linked to the intrinsic function of the human body, biological signals may require more advanced processing for use in identity problems. Also, they may convey clinical side information that can be used simultaneously. For example, electrocardiograms [7, 8, 9] and heart sounds [10] have been explored for use in identity problem.



Designing a system that uses biological signals presents challenges due to the dynamics that are typically associated with such signals, but stands to benefit from the innate nature of the signal.

As alluded to in the previous section, the roles of identity and state of the individual are inherently tied together. Thus, it may be advantageous to consider the clinical applications of biological signals together with the security applications. Advances in one area may influence the other.

### **1.3 Laser Doppler Vibrometry**

Models that are developed in this dissertation are applied to measurements of skin velocity overlying the carotid artery using a laser Doppler vibrometer. This is a novel method of sensing cardiovascular activity in a noncontact and standoff manner. At distances of several meters, we are able to collect pulses that may harbor critical information pertaining to the function of the heart and vasculature. One of the processing goals is to draw out relevant information for use in a clinical or security setting. In many cases, contact with the individual may not be possible or desired. This allows for the collection of biological data in a wide variety of operational settings. For example, after natural disasters hit, the task of locating and probing the state of an individual that is trapped or injured is critical. Clearly the ability to gather such information in a timely manner is central to the survival of that individual. The laser needs only a line of sight to the individual to begin recording a signal. Although the data that are used in this dissertation are taken using an LDV targeted on the neck, we have also experimented with other sites, including through clothing. It seems that

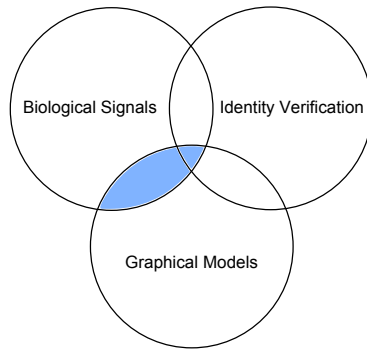


Figure 1.2: Intersecting themes of the dissertation.

at a minimum, the LDV can be used to detect the timing of heart beats and liveness from almost any targeting vantage.

## 1.4 Outline and Contributions

The main themes of this dissertation follow along the various intersections of biological signals (the substance), graphical models (the tools), and identity verification (the application). Figure 1.2 shows a diagram of these three areas, and the resulting intersecting areas. The two highlighted sections are the main focus of this dissertation.

Chapter 2 begins by describing the background tools and methods of graphical models. A graphical model is one that is Markov with respect to a graph, and their prolific use in many different applications is largely due to the existence of efficient algorithms to perform inference and estimation when the graph is cycle-free. The sum-product and max-product algorithms are described in this chapter, along with hidden Markov models and nested hidden Markov models.

Chapter 3 begins by describing biological signals, and showing a few examples. In this chapter, graphical models are applied to biological signals by defining a hierarchical

structure of state changes that occur within an individual. This structure has three levels, representing short, medium, and long term variability that is present in the individual. The resulting model may incorporate a variety of dynamics that are related to the measured signal.

In Chapter 4, the use of the LDV for making cardiovascular measurements is described. The LDV senses movements of the skin surface overlying the carotid artery along the neck. These movements are related to the underlying blood pressure, and therefore may be informative as to the cardiovascular state of the individual. Preprocessing tools are also given, including the short-time Fourier transform.

After introducing the LDV, Chapter 5 contains the evaluation and interpretation of the models defined in Chapter 3 for the LDV. The model fit is quantitatively evaluated under a variety of training and testing conditions. Model parameters are interpreted in terms of the underlying physiology, and the use of the models for pulse characterization and breathing estimation are demonstrated.

The underlying physics for the LDV signal is explored in Chapter 6. Fluid dynamics in an elastic tube are considered as a model for blood flow in the carotid, and models are constructed that are motivated by this analysis. A sequence of assumptions that are necessary to claim that the LDV signal is proportional to the underlying blood pressure is given. Although all of these assumptions are generally not valid, the resemblance of the LDV displacement pulse has experimentally been found to be similar to blood pressure waveforms. The models are estimated on LDV data and interpreted.

Identity verification system design and results are given in Chapter 7. The system is constructed using a normalized loglikelihood ratio test, in which models are trained

for each individual in a central database. Performance is predicted using experimental data, and confidence intervals are constructed taking correlations of the decisions into account.

The contributions of this work are:

- Developed a method for applying graphical models to biological signals, with physiological interpretations,
- Evaluated models for the LDV data for use in waveform analysis and breathing estimation,
- Presented analysis for pressure waves in elastic tubes with respect to the indirect measurement of pressure using the LDV,
- Evaluated ID verification systems using the LDV that do not treat pulses independently,
- Constructed confidence intervals on performance curves for ID verification systems using the LDV.

# Chapter 2

## Graphical Models and Algorithms

Graphical models are popular models that find use in diverse fields. They provide a unified structure from which models, inference algorithms, and estimation algorithms may be derived. The ability to visualize a model in the form of a graph is appealing, both aesthetically and mathematically. Due to the generalizable nature of graphical models, many books and review papers have been written about them [11, 12, 13].

Conditional dependence between random variables are encoded by graphical models. Some of these random variables may represent measured data, while others may represent unknown quantities. Using the graphical structure of the model, and the associated probability distributions, efficient algorithms exist for parameter estimation and inference, that capitalize on the structure of the model. These algorithms are especially efficient when the graph is a tree.

Applications of graphical models are various. A brief list may include:

- Error correcting codes [14, 15, 16],
- Genetics [17, 18],
- Speech recognition [19, 20, 21, 22],

- Image modeling [23, 24, 25, 26],
- Radar [27, 28, 29],
- ECG processing [30] and heart rate analysis [31].

The review by Wainwright and Jordan [11] contains more examples. Algorithms for performing inference on graphical models are essentially message passing algorithms which compute sum or max marginal functions of a given function of many variables [32, 33]. These algorithms compute and communicate “messages” from node to node on graphs without cycles. If the graph has cycles, then partial message passing may be used for portions of the graph that are cycle-free. Otherwise, a number of approximate inference algorithms exist [34].

This class of models is used for the processing of biological signals because of the flexibility in the design of models to capture a variety of underlying phenomenology. The dynamics of internal processes in the human body responsible for the generation of biological signals are usually unknown. In clinical applications, these may be the desired quantities. In many cases it is difficult or impossible to directly measure this central activity. Graphical models, through the use of hidden variables, allow us to model those processes that we are unable to acquire directly. By constraining the interactions between the measurements that we do make, we can make inferences about those that are hidden to us.

In this chapter, graphical models are defined. There is enough detail to provide a base for many of the subsequent methods in the dissertation. Basic definitions from graph theory are provided. Then a model is defined on a graph, and finally, algorithms for estimation and inference are presented. More detailed information on graphical models can be found in the books by Jordan and Lauritzen [13, 12].

## 2.1 Some Definitions from Graph Theory

We begin with the definition of a graph. A *graph* (or *directed graph*)  $G = (V, E)$  is a collection of vertices (or nodes),  $V = \{1, 2, \dots, m\}$ , and ordered pairs of vertices called edges,  $E \subset V \times V$ . The set of edges  $E$  may not contain multiple copies of the same edge. An *undirected graph* is a graph whose edges are not ordered pairs; thus the edges  $(a, b)$  and  $(b, a)$  are indistinguishable.

In the following definitions, consider an undirected graph  $G = (V, E)$ .

- Two vertices  $a, b \in V$  are *connected* if and only if  $(a, b) \in E$ ; this is denoted  $a \leftrightarrow b$ .
- The *neighbors* of a vertex  $a$  are the set of vertices  $\mathcal{N}(a) = \{b \mid (a, b) \in E\}$ .
- A *subgraph* with respect to  $V_S \subset V$ , is the graph  $G_S = (V_S, E_S)$ , where  $E_S = \{(a, b) \mid a, b \in V_S, (a, b) \in E\}$ .
- A *clique* is a subset of the vertex set,  $C \subset V$ , such that  $(a, b) \in E$  for all  $a, b \in C$ . The size of the clique is equal to the number of vertices in the clique.
- A *path*  $P$  is an ordered sequence of edges  $P = \{(v_0, v_1), (v_1, v_2), \dots, (v_{k-1}, v_k)\}$ , each one belonging to  $E$ ; the path is said to join vertices  $v_0$  and  $v_k$ . The notation  $a \leftrightarrow b$  means that there exists a path between the two nodes  $a$  and  $b$ .
- A graph is *connected* if  $a \leftrightarrow b$  for all  $a, b \in V$ .
- A *cycle* is a path that starts and ends at the same node.
- A *simple graph* is an undirected graph such that  $a \neq b$  for all  $(a, b) \in E$ .
- A graph is a *tree* if it is connected and has no cycles.

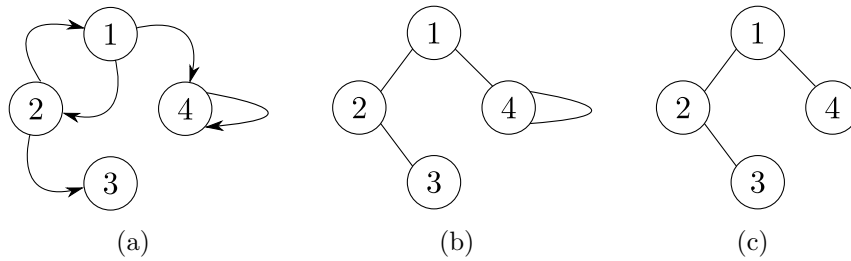


Figure 2.1: Examples of a graphs with four vertices. The graph in (a) has 5 edges:  $E_a = \{(1, 2), (2, 1), (1, 4), (2, 3), (4, 4)\}$ . The undirected graph in (b) has 4 edges  $E_b = \{(1, 2), (1, 4), (2, 3), (4, 4)\}$ . The graph in (c) is simple and contains 3 edges,  $E_c = \{(1, 2), (1, 4), (2, 3)\}$ .

The notation of separation between subgraphs is important in the subsequent definition of a graphical model. Let  $A$ ,  $B$ , and  $C$  be distinct subsets of  $V$ . The subset  $B$  separates two other subsets of nodes if it is impossible to construct a path from  $A$  to  $C$  without going through nodes in  $B$ . More formally,  $B$  is said to *separate*  $A$  and  $C$  if and only if  $\{(a, c) \mid a \in A, c \in C, a \leftrightarrow c\} = \emptyset$  with respect to the subgraph  $G_{A \cup C}$ .

Pictorially, graphs can be drawn with circles representing vertices, and arrows connecting them representing edges. An arrow from vertex  $a$  to vertex  $b$  means that  $(a, b) \in E$ . See Figure 2.1 for an example of a graph drawn in this way. When drawing undirected graphs, we use lines instead of arrows. This implies the lack of directionality in undirected graphs. See Figure 2.1 for examples of undirected and simple graphs.



## 2.2 Random Vectors and Conditional Independence

Consider a random variable  $X$ , with realization  $x$ . The space on which  $x$  takes values is  $\mathcal{X}$ , and its PDF is  $f_X(x)$ . To simplify notation, we use the symbol  $f$  to denote joint and conditional distributions in general, where the associated random variables can be inferred from the arguments. For example,  $f(x_1)$ ,  $f(x_1, x_2)$  are the distributions for  $X_1$  and  $(X_1, X_2)$ , respectively; while  $f(x_2|x_1)$  is the distribution of  $X_2|X_1$ . The random vector

$$\mathbf{X} = \begin{bmatrix} X_1 & X_2 & \dots & X_m \end{bmatrix}^T \quad (2.1)$$

has the distribution

$$f : \otimes_{v=1}^m \mathcal{X}_v \rightarrow \mathbb{R}_+, \quad (2.2)$$

where  $\otimes_{v=1}^m \mathcal{X}_v$  denotes the product space  $\mathcal{X}_1 \times \mathcal{X}_2 \times \dots \times \mathcal{X}_m$ .

In general, there are many ways to factor  $f(\mathbf{x})$  depending on the ordering of the random variables. One factorization is

$$f(\mathbf{x}) = f(x_1) f(x_2|x_1) f(x_3|x_2, x_1) \cdots f(x_m|x_{m-1}, x_{m-2}, \dots, x_1). \quad (2.3)$$

A more simple expression may be obtained if any of the random variables are conditionally independent. For example, if  $X_1$  is independent of  $X_3$  given  $X_2$  (written as  $X_1 \perp X_3|X_2$ ), then  $f(x_1, x_3|x_2) = f(x_1|x_2) f(x_3|x_2)$ . Thus  $f(x_3|x_2) = f(x_3|x_2, x_1)$  and

$$f(\mathbf{x}) = f(x_1) f(x_2|x_1) f(x_3|x_2) f(x_4|x_3, x_2, x_1) \cdots f(x_m|x_{m-1}, x_{m-2}, \dots, x_1). \quad (2.4)$$

Note that the third function in this product is a function of two variables, and not three, like in the general case. The ability to simplify the joint distribution based on conditional independence has important consequences for inference and estimation algorithms.

If the random variables are independent, then  $f(\mathbf{x}) = \prod_{v=1}^m f(x_v)$ , with  $\mathbf{x} = (x_1, x_2, \dots, x_m)$ .

If the random variables form a Markov chain,  $X_1 \rightarrow X_2 \rightarrow \dots \rightarrow X_m$ , then  $f(\mathbf{x}) = f(x_1) f(x_2|x_1) f(x_3|x_2) \dots f(x_m|x_{m-1})$ .

## 2.3 Graphical Models

Consider a set of random variables,  $X_v$ , each one associated with a vertex of a simple graph  $G = (V, E)$ , where  $v \in V$ . The space on which realizations of the random variables take values is denoted  $\mathcal{X}_v$ . Denote the random vector of  $m$  random variables for the graph as  $\mathbf{X}$ , and a realization as  $\mathbf{x}$ . When  $A$  is a subset of  $V$ , the random vector over  $A$  is denoted  $\mathbf{X}_A$ , and a realization is  $\mathbf{x}_A$ .

Markov random processes can be characterized by a set of conditional independence statements of the form  $\mathbf{X}_A \perp \mathbf{X}_C | \mathbf{X}_B$ . A Markov chain, for example, is a random process  $X_1, X_2, \dots, X_n$  for which  $\mathbf{X}_A \perp \mathbf{X}_C | \mathbf{X}_i$  for any  $i$  where  $A = (X_1, X_2, \dots, X_{i-1})$  and  $C = (X_{i+1}, X_{i+2}, \dots, X_n)$ . Below, we define the notion of a random vector being Markov with respect to a graph, using the notion of graph separation defined in the previous section. Then a graphical model is defined in terms of the factorization of the PDF into a product of functions defined on the cliques of the graph. These functions are called *compatibility functions*, and the domains of these functions is the product spaces of their vertices:  $\psi_C : \otimes_{v \in C} \mathcal{X}_v \rightarrow \mathbb{R}_+$ . The Hammersley-Clifford Theorem

connects the two definitions, and allows us to directly state the Markov properties of a graphical model.

**Definition 2.1.** *Let  $A$ ,  $B$ , and  $C$  be distinct subsets of  $V$ . A random vector  $\mathbf{X}$  defined on the vertices of a graph  $G$  is Markov with respect to  $G$  if and only if  $\mathbf{X}_A \perp \mathbf{X}_C | \mathbf{X}_B$  whenever  $B$  separates  $A$  and  $C$ .*

**Definition 2.2.** *A graphical model is a distribution for the random vector  $\mathbf{X}$  defined on a graph  $G$  that factorizes as  $f(\mathbf{x}) = \frac{1}{Z} \prod_{C \in \mathcal{C}} \psi_C(\mathbf{x}_C)$ , where  $\mathcal{C}$  is the set of all cliques and  $Z = \int_{\otimes_v x_v} \prod_{C \in \mathcal{C}} \psi_C(\mathbf{x}_C)$  is a normalizing constant ensuring that  $\int_{\otimes_v x_v} f(\mathbf{x}) = 1$ .*

The dependencies between the random variables may be expressed using a simple graph. If two nodes in the graph are connected, then the corresponding random variables are dependent. The following is the Hammersley-Clifford Theorem.

**Theorem 2.1.** *If  $f$  is a graphical model for  $\mathbf{X}$  on  $G$ , then  $\mathbf{X}$  is Markov with respect to  $G$ . Conversely, if  $\mathbf{X}$  is Markov with respect to  $G$ , then there exists a graphical model  $f$  for  $\mathbf{X}$  on  $G$ .*

Proofs of this theorem can be found in [35, 36]. For the case of trees, the cliques are either the single vertices themselves, with compatibility functions  $\psi_v(x_v)$ , or pairs of vertices, with compatibility functions  $\psi_{a,b}(x_a, x_b)$ . The graphical model for  $\mathbf{X}$  with respect to a tree is the normalized product of the clique potentials. In this case the PDF factorizes as

$$f(\mathbf{x}) = \frac{1}{Z} \prod_{v \in V} \psi_v(x_v) \prod_{(a,b) \in E} \psi_{a,b}(x_a, x_b), \quad (2.5)$$

since the cliques are the nodes themselves and pairs of nodes in the case of a tree. One consistent definition of the clique potentials is

$$\psi_v(x_v) = f(x_v), \tag{2.6}$$

and

$$\psi_{a,b}(x_a, x_b) = \frac{f(x_a, x_b)}{f(x_a)f(x_b)}. \tag{2.7}$$

Equivalently, we can have the functions in Equation 2.6 for all vertices  $a$  for which  $|\mathcal{N}(a)| = 1$ , and  $\psi_v(x_v) = 1$  otherwise. Then the compatibility functions for pairs of connected vertices is  $\psi_{a,b}(x_a, x_b) = f(x_a|x_b)$  or  $\psi_{a,b}(x_a, x_b) = f(x_b|x_a)$ .

## 2.4 Algorithms for Graphical Models on Trees

In this section, algorithms for computing marginal functions of a given function  $f(x_1, x_2, \dots, x_m)$  are described that are more efficient than brute force methods. These algorithms are especially efficient when the function factorizes into a product of functions of one or two variables, and capitalize on this factorization. For example, consider a function over a discrete space that factorizes as  $f(x_1, x_2, x_3) = g(x_1)g(x_1, x_2)g(x_2, x_3)$ . The computation of

$$f(x_2) = \sum_{\mathcal{X}_1} \sum_{\mathcal{X}_3} f(x_1, x_2, x_3), \tag{2.8}$$

requires  $|\mathcal{X}_1||\mathcal{X}_3|$  computations. For functions of many variables with large domains, this procedure quickly becomes unfeasible. Instead, we may take advantage of the

factorization and instead compute

$$f(x_2) = \left( \sum_{\mathcal{X}_1} g(x_1) g(x_1, x_2) \right) \left( \sum_{\mathcal{X}_3} g(x_2, x_3) \right). \quad (2.9)$$

This requires  $|\mathcal{X}_3| + 2|\mathcal{X}_1| + 1$  computations. This is a large improvement when the domains are large.

A graph may be defined for any function that describes its factorization. If each variable of this function is represented by a node in a graph, we connect nodes with undirected edges that are in one of the product terms. This leads to a graph where each clique is the domain of one of the product functions in the factorization. Figure 2.2 shows the graph for the above example, where the corresponding clique potential functions are:

$$\begin{aligned} \psi_1(x_1) &= g(x_1), \\ \psi_{1,2}(x_1, x_2) &= g(x_1, x_2), \\ \psi_{2,3}(x_2, x_3) &= g(x_2, x_3). \end{aligned}$$

The algorithms in this section can be visualized as passing messages along the edges of such a graph. Specific instances of these message passing algorithms include the forward-backward algorithm [37] and the Viterbi algorithm [38, 39], which is a special case of computing the mode.

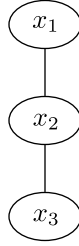


Figure 2.2: Graph for a function that factorizes as  $f(x_1, x_2, x_3) = g(x_1)g(x_1, x_2)g(x_2, x_3)$ .

### 2.4.1 Computing Marginal Distributions

The algorithms described here are for computing marginal distributions,  $f(x_a)$  associated with a single vertex for a Markov random vector  $\mathbf{X}$  with respect to a tree  $G$ . Joint distributions over a subset of the variables can also be computed in the process. An efficient algorithm, known as the sum-product algorithm, can be used to compute marginal distributions  $f(x_A)$ , where  $A$  is any subset of the nodes. A message is defined from vertex  $a$  to vertex  $b$  according to

$$m_{a,b}(x_b) = \int_{\mathcal{X}_a} \left( \psi_a(x_a) \psi_{a,b}(x_a, x_b) \prod_{k \in \mathcal{N}(a), k \neq b} m_{k,a}(x_a) \right). \quad (2.10)$$

The integral in this expression represents a summation in the case of a discrete domain  $\mathcal{X}_a$ . Each message from node  $a$  to node  $b$  involves a summation over its domain and a product over all other messages to node  $a$ , except for the message from node  $b$  to node  $a$ . After all of the messages are passed, any marginal distribution can be computed as

$$f(x_a) = \frac{1}{Z} \psi_a(x_a) \prod_{b \in \mathcal{N}(a)} m_{b,a}(x_a). \quad (2.11)$$

If a joint distribution is required, then the same messages are computed, except that the integral in Equation 2.10 for variables in the desired joint distribution should be

omitted. The messages may be functions of multiple variables in this case, and not only a function of the variable associated with the node that the message is passed from. Then, the joint distribution is computed by Equation 2.11 on any one of the joint variables. For example, we can compute  $f(x_a, x_b)$  by

$$f(x_a, x_b) = \frac{1}{Z} \psi_a(x_a) m_{b,a}(x_a, x_b) \prod_{\substack{i \in \mathcal{N}(a) \\ i \neq b}} m_{i,a}(x_a), \quad (2.12)$$

where

$$m_{b,a}(x_a, x_b) = \psi_b(x_b) \psi_{a,b}(x_a, x_b) \prod_{k \in \mathcal{N}(b), k \neq a} m_{k,b}(x_b). \quad (2.13)$$

## 2.4.2 Computing the Mode

For the random vector  $\mathbf{X}$ , the mode is given by

$$\hat{\mathbf{x}} = \arg \max_{\otimes_v \mathcal{X}_v} f(\mathbf{x}). \quad (2.14)$$

The mode may be computed using the max-product algorithm, which is similar to the sum-product algorithm. In the sum-product algorithm, the variable that the each message is passed from is summed out of the message. For the max-product algorithm, we take the max instead of the sum. The messages are computed using

$$m_{a,b}(x_b) = \max_{x_a} \left( \psi_a(x_a) \psi_{a,b}(x_a, x_b) \prod_{k \in \mathcal{N}(a), k \neq b} m_{k,a}(x_a) \right). \quad (2.15)$$

Some of the nodes may be left out of the mode computation if desired. In this case, the max is computed over only those nodes of interest in the graph. To compute the  $i^{\text{th}}$  value of  $\hat{\mathbf{x}}$ , we compute the following max-marginal function, analogous to

Equation 2.11:

$$g(x_i) \triangleq \max_{\substack{\otimes \mathcal{X}_a \\ a \neq i}} f(\mathbf{x}) \quad (2.16)$$

$$= \frac{1}{Z} \psi(x_i) \prod_{b \in \mathcal{N}(i)} m_{b,i}(x_i). \quad (2.17)$$

Finally, we compute

$$\hat{x}_i = \arg \max_{x_i \in \mathcal{X}_i} g(x_i). \quad (2.18)$$

The procedure of computing the maximizing values  $\hat{x}_i$  is sometimes called backtracking. These values are the mode of the random vector. More details on the max-product algorithm can be found in the paper by Wainwright [40].

### 2.4.3 Inference on a Hidden Markov Model

The structure of a Hidden Markov Model (HMM) is shown in Figure 2.3. There are  $2m$  nodes in this model. Each of the  $x_i$  nodes corresponds to a discrete random variable  $X_i$  with support  $\mathcal{X}_i$ . These random variables correspond to an underlying process, and they form a Markov chain. Each of the  $y_i$  nodes corresponds to a discrete or continuous random variable  $Y_i$  with support  $\mathcal{Y}_i$ . These nodes correspond to the measured data.



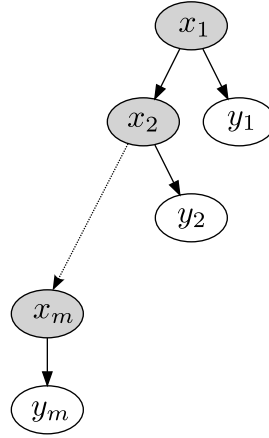


Figure 2.3: A Hidden Markov Model.

The compatibility functions are:

$$\psi_{x_i}(x_i) = \begin{cases} f(x_1), & i = 1 \\ 1, & \text{else,} \end{cases} \quad (2.19)$$

$$\psi_{x_i, x_{i+1}}(x_i, x_{i+1}) = f(x_{i+1}|x_i), \quad (2.20)$$

$$\psi_{y_i}(y_i) = 1, \quad (2.21)$$

$$\psi_{x_i, y_i}(x_i, y_i) = f(y_i|x_i). \quad (2.22)$$

From Equation 2.5, the joint distribution of all of the random variables is

$$f(\mathbf{x}, \mathbf{y}) = \prod_{v \in V} \psi_v(x_v) \prod_{(a,b) \in E} \psi_{a,b}(x_a, x_b) \quad (2.23)$$

$$= f(x_1) f(y_1|x_1) f(x_2|x_1) f(y_2|x_2) \cdots f(x_m|x_{m-1}) f(y_m|x_m). \quad (2.24)$$

Often, we are interested in computing  $f(x_i|\mathbf{y})$  and  $f(x_i, x_{i+1}|\mathbf{y})$ . These marginal distributions are important for the estimation of parameters in the expectation maximization algorithm. Since  $\mathbf{y}$  is included in these marginal distributions, we do not

need to compute the messages from  $y_i$  to  $x_i$ . From Equation 2.11

$$f(x_i|\mathbf{y}) = \frac{1}{Z} m_{x_{i-1},x_i}(x_i|y_1, \dots, y_{i-1}) m_{x_{i+1},x_i}(x_i|y_{i+1}, \dots, y_m) f(y_i|x_i). \quad (2.25)$$

The right side of this equation is equal to  $\frac{1}{Z} f(x_i, \mathbf{y})$ , and  $f(x_i|\mathbf{y})$  is computed using the normalizing factor  $Z = f(\mathbf{y})$ . This can be viewed as a two part computation. In the first part, we compute backward messages, and in the second part, we compute forward messages. The forward part is computed by

$$m_{x_1,x_2}(x_2|y_1) = \sum_{x_1} f(x_1) f(x_2|x_1) f(y_1|x_1), \quad (2.26)$$

$$m_{x_2,x_3}(x_3|y_1, y_2) = \sum_{x_2} f(x_3|x_2) f(y_2|x_2) m_{x_1,x_2}(x_2|y_1), \quad (2.27)$$

$$\vdots \quad \vdots \quad (2.28)$$

$$m_{x_{i-1},x_i}(x_i|y_1, \dots, y_{i-1}) = \sum_{x_{i-1}} f(x_i|x_{i-1}) f(y_{i-1}|x_{i-1}) m_{x_{i-2},x_{i-1}}(x_{i-1}|y_1, \dots, y_{i-2}).$$

The backward part is computed by

$$m_{x_m,x_{m-1}}(x_{m-1}|y_m) = \sum_{x_m} f(x_m|x_{m-1}) f(y_m|x_m), \quad (2.29)$$

$$\begin{aligned} m_{x_{m-1},x_{m-2}}(x_{m-2}|y_{m-1}, y_m) &= \sum_{x_{m-1}} f(x_{m-1}|x_{m-2}) f(y_{m-1}|x_{m-1}) m_{x_m,x_{m-1}}(x_{m-1}|y_m), \\ &\vdots \quad \vdots \quad (2.30) \end{aligned}$$

$$m_{x_{i+1},x_i}(x_i|y_{i+1}, \dots, y_m) = \sum_{x_{i+1}} f(x_{i+1}|x_i) f(y_{i+1}|x_{i+1}) m_{x_{i+2},x_{i+1}}(x_{i+1}|y_{i+2}, \dots, y_m).$$

In this way, any of the  $f(x_i|\mathbf{y})$  may be computed. The joint distribution  $f(x_i, x_{i+1}|\mathbf{y})$  is computed by

$$f(x_i, x_{i+1}|\mathbf{y}) \propto m_{x_{i-1},x_i}(x_i|y_1, \dots, y_{i-1}) f(y_i|x_i) f(x_{i+1}|x_i). \quad (2.31)$$

$$f(y_{i+1}|x_{i+1}) m_{x_{i+2}, x_{i+1}}(x_{i+1}|y_{i+2}, \dots, y_m).$$

The distribution of  $\mathbf{y}$  is the normalizing constant for the distribution of  $x_i$ , and may be computed by

$$f(\mathbf{y}) = \sum_{x_i} f(x_i, \mathbf{y}), \quad (2.32)$$

for any  $x_i$ .

#### 2.4.4 Inference on Nested Hidden Markov Models

Each of the  $f(y_i|x_i)$  in the HMM may be another HMM. We can denote levels of HMMs using superscripts. The top level is  $x_i^{(1)}, y_i^{(1)}$ , the second level is  $x_{i,j}^{(2)}, y_{i,j}^{(2)}$ , and so on. In this case, inference is performed in a straightforward manner. Whenever computation of  $f(\mathbf{y}_i^{(p)}|\mathbf{x}_i^{(p)})$  is required, an inference algorithm is performed on the  $(p+1)^{th}$  level.

Consider Figure 2.4, which shows a nested HMM containing two levels. The  $\mathbf{y}_i^{(1)}$  variables represent all of the variables in the corresponding HMM in the next level, so that  $\mathbf{y}_i^{(1)} = (x_{i,1}^{(2)}, x_{i,2}^{(2)}, \dots, x_{i,n}^{(2)}, y_{i,1}^{(2)}, y_{i,2}^{(2)}, \dots, y_{i,n}^{(2)})$ . Only observed variables in the bottom level represent the data, and these variables may be denoted simply as  $\mathbf{y}^{(2)}$ .

First, consider the computation of  $f(x_i^{(1)}|\mathbf{y}^{(2)})$  for any  $i$ . This is computed by multiplying forward and backward functions

$$f(x_i^{(1)}|\mathbf{y}^{(2)}) = \frac{1}{Z} m_{x_{i-1}, x_i^{(1)}}(x_i^{(1)}|\mathbf{y}_1^{(2)}, \dots, \mathbf{y}_{i-1}^{(2)}) m_{x_{i+1}, x_i}(x_i^{(1)}|\mathbf{y}_{i+1}^{(2)}, \dots, \mathbf{y}_m^{(2)}) f(\mathbf{y}_i^{(2)}|x_i^{(1)}).$$

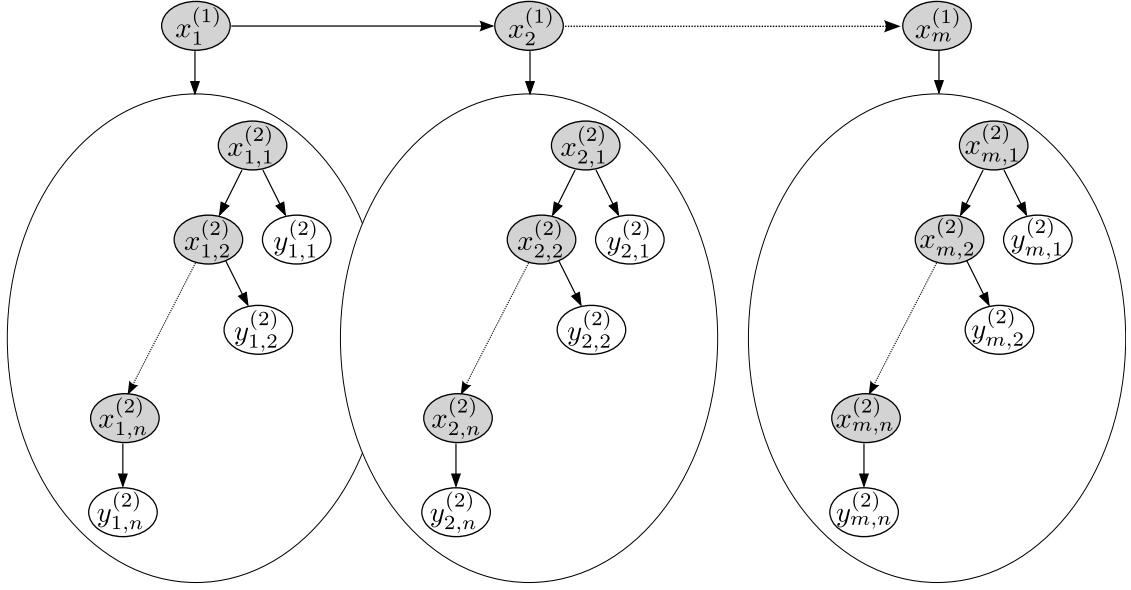


Figure 2.4: A nested HMM.

The forward part is computed by

$$\begin{aligned}
m_{x_1^{(1)}, x_2^{(1)}}(x_2^{(1)} | \mathbf{y}_1^{(2)}) &= \sum_{x_1^{(1)}} f(x_1^{(1)}) f(x_2^{(1)} | x_1^{(1)}) f(\mathbf{y}_1^{(2)} | x_1^{(1)}), \quad (2.33) \\
m_{x_2^{(1)}, x_3^{(1)}}(x_3^{(1)} | \mathbf{y}_1^{(2)}, \mathbf{y}_2^{(2)}) &= \sum_{x_2^{(1)}} f(x_3^{(1)} | x_2^{(1)}) f(\mathbf{y}_2^{(2)} | x_2^{(1)}) m_{x_1^{(1)}, x_2^{(1)}}(x_2^{(1)} | \mathbf{y}_1^{(2)}), \\
&\vdots \quad \vdots \\
m_{x_{i-1}^{(1)}, x_i^{(1)}}(x_i^{(1)} | \mathbf{y}_1^{(2)}, \dots, \mathbf{y}_{i-1}^{(2)}) &= \\
&\sum_{x_{i-1}^{(1)}} f(x_i^{(1)} | x_{i-1}^{(1)}) f(\mathbf{y}_{i-1}^{(2)} | x_{i-1}^{(1)}) m_{x_{i-2}^{(1)}, x_{i-1}^{(1)}}(x_{i-1}^{(1)} | \mathbf{y}_1^{(2)}, \dots, \mathbf{y}_{i-2}^{(2)}).
\end{aligned}$$

Each of these steps requires computation of the lower level,  $f(\mathbf{y}_i^{(2)}|x_i^{(1)})$ , which uses another sum-product algorithm via Section 2.4.3. The backward part is computed by

$$m_{x_m^{(1)}, x_{m-1}^{(1)}}(x_{m-1}^{(1)}|\mathbf{y}_m^{(2)}) = \sum_{x_m^{(1)}} f(x_m^{(1)}|x_{m-1}^{(1)}) f(\mathbf{y}_m^{(2)}|x_m), \quad (2.34)$$

$$m_{x_{m-1}^{(1)}, x_{m-2}^{(1)}}(x_{m-2}^{(1)}|\mathbf{y}_{m-1}^{(2)}, \mathbf{y}_m^{(2)}) = \sum_{x_{m-1}^{(1)}} f(x_{m-1}^{(1)}|x_{m-2}^{(1)}) f(\mathbf{y}_{m-1}^{(2)}|x_{m-1}^{(1)}) \cdot m_{x_m^{(1)}, x_{m-1}^{(1)}}(x_{m-1}^{(1)}|\mathbf{y}_m^{(2)}), \quad (2.35)$$

⋮     ⋮

$$m_{x_{i+1}^{(1)}, x_i^{(1)}}(x_i^{(1)}|\mathbf{y}_{i+1}^{(2)}, \dots, \mathbf{y}_m^{(2)}) = \sum_{x_{i+1}^{(1)}} f(x_{i+1}^{(1)}|x_i^{(1)}) f(\mathbf{y}_{i+1}^{(2)}|x_{i+1}^{(1)}) m_{x_{i+2}^{(1)}, x_{i+1}^{(1)}}(x_{i+1}^{(1)}|\mathbf{y}_{i+2}^{(2)}, \dots, \mathbf{y}_m^{(2)}).$$

In this way, any of the  $f(x_i^{(1)}|\mathbf{y}^{(2)})$  may be computed. Computation of the joint distribution  $f(x_i^{(1)}, x_{i+1}^{(1)}|\mathbf{y}^{(2)})$ , similarly to the single HMM case, is computed by

$$f(x_i^{(1)}, x_{i+1}^{(1)}|\mathbf{y}^{(2)}) \propto m_{x_{i-1}^{(1)}, x_i^{(1)}}(x_i^{(1)}|\mathbf{y}_1^{(2)}, \dots, \mathbf{y}_{i-1}^{(2)}) f(\mathbf{y}_i^{(2)}|x_i) f(x_{i+1}^{(1)}|x_i^{(1)}) \cdot f(\mathbf{y}_{i+1}^{(2)}|x_{i+1}^{(1)}) m_{x_{i+2}^{(1)}, x_{i+1}^{(1)}}(x_{i+1}^{(1)}). \quad (2.36)$$

The distribution of  $\mathbf{y}^{(2)}$  is the normalizing constant for the distribution of  $x_i^{(1)}$ , and may be computed by

$$f(\mathbf{y}^{(2)}) = \sum_{x_i^{(1)}} f(x_i^{(1)}, \mathbf{y}^{(2)}), \quad (2.37)$$

for any  $x_i^{(1)}$ .

This procedure may be performed on any number of nested HMMs.

# Chapter 3

## Models for Biological Signals

A model is an approximate description of data acquired under a specific set of conditions. Since all models are approximate, there is no notion of a single true model. Some models may be successful in certain applications, and others may be successful in other applications. Trial and error plays an important role in the experimental evaluation of models, and the prediction of performance for an application becomes a critical component. However, this does not mean that model based design is an entirely guess and check operation. There is a significant knowledge base related to the underpinnings of biological signals. In many cases, quantitative analysis rooted in the fundamental laws of physics which is common to engineering design is not available for the complicated physiological processes that are responsible for generating biological signals. When they are available, they are often too complex for efficient computation. Thus, model design benefits from, and can be built upon, previous work, but often requires a flexible approach to incorporate many different views.

Processing biological signals is a challenging task due to the complexities of the human body. Basic principles of physics may be used to construct models that are of great use [41]. However, some of these models do not accurately represent the richness of

the signal. Despite this, they are enormously useful for preliminary modeling and acquiring a fundamental understanding of the underlying process. In other approaches, digital signal processing tools from other domains are applied to either help remove certain unwanted components of the signal [42, 43], or extract only the components that are deemed necessary for some application [44]. These methods sometimes lack a connection with the basic phenomenology. A special issue of the IEEE Transactions on Biomedical Engineering [45] focused on signal processing and modeling for heart rate series and related data.

The approach described in this dissertation is a combination of the two, and sometimes leaning more towards one direction than the other. Models are developed with the underlying physiology at the core of the design, but ultimately the models may deviate from this basis. In this chapter, examples for biological signals are presented, including a description of the underlying physiology. Examples are given of the electrical activity of the heart, blood flow through the arterial and venous systems, and respiration. Commonality between these signals motivates a modeling framework that utilizes the tools from Chapter 2.

## **3.1 Biological Signals**

We begin by describing three different types of biological signals, resulting from different, but deeply related physiological processes. The first two involve the flow of blood in the cardiovascular system. The nature of blood flow through the vessels is impacted by numerous factors, such as the elasticity of the vessel walls, the blood density, and the geometry of the vasculature. All of these factors affect the pressure at any point along the vasculature, which is a mechanical quantity. In the second

example, the measured activity is generated from the electrical activity of the heart. The heart is the central organ in the cardiovascular system, and it is regulated and activated electrically. Respiration, which may be the simplest of the three examples functionally, may be the most difficult to quantify because it is partially autonomous. Therefore, the underlying biological process may be difficult to infer from measurements. These descriptions are valid under normal conditions for healthy individuals. For some applications, however, it may be of interest to detect deviations from the norm.

### 3.1.1 Examples of Biological Signals

Blood, which is the carrier of oxygen among other purposes, is provided to the tissues of the body through the systemic circuit. It is pumped from the heart to the large arteries, and enters progressively smaller vessels until the capillaries are reached. These are extremely small vessels that aid the transfer of oxygen from the blood to the tissues. Carbon dioxide is exchanged into the blood, where it is eventually transported to the lungs and expelled. The resulting deoxygenated blood returns through the veins, and enters the heart in the right atrium. In the heart, blood from the pulmonary circuit is transferred to the systemic circuit. Figure 3.1 shows a depiction of blood circulation<sup>1</sup>. When the atria contract, this blood flows into the right ventricle. After ventricle contraction, it is forced through the pulmonary arteries and enters the lungs, where the blood is oxygenated. This oxygen rich blood returns to the heart into the left atrium, and goes into the left ventricle after the atria contract. Once again, when the ventricles contract, blood is pumped into the systemic arteries.

---

<sup>1</sup>Drawing in the public domain by Mariana Villarreal



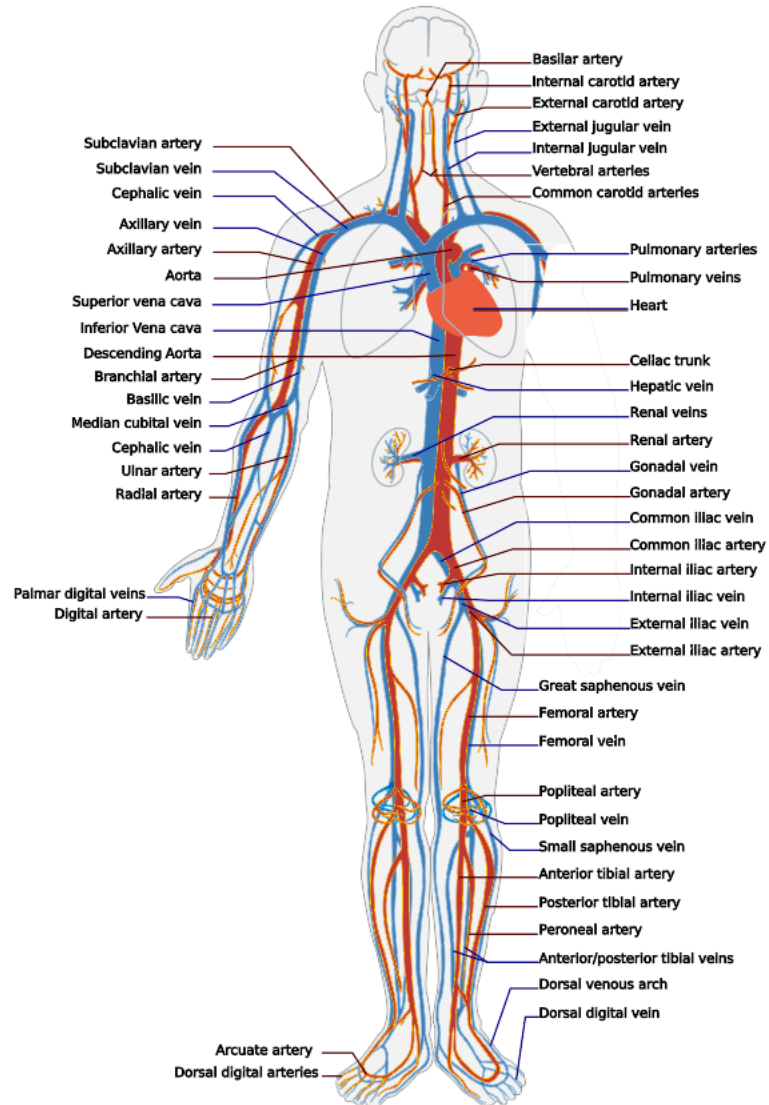


Figure 3.1: A drawing of the circulatory system.

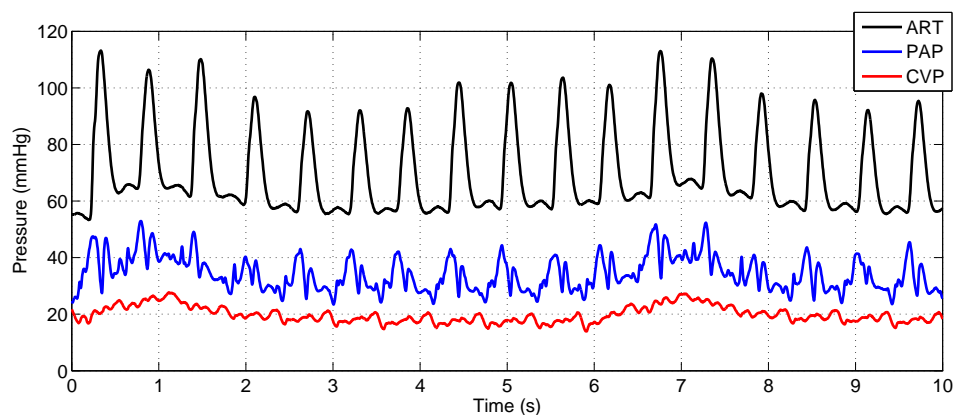


Figure 3.2: Blood pressure recordings of systemic arterial pressure, pulmonary arterial pressure, and central venous pressure.

The heart pumps blood into both circuits simultaneously. Atrial contractions push blood from the left and right atria into the left and right ventricles, respectively. There is no pathway between the left and right halves of a healthy heart. Ventricle contractions pump blood into the systemic and pulmonary arteries.

Blood pressure is highest in the arteries, although during the cardiac cycle the pressure typically changes by approximately 60 mmHg there. As blood travels into smaller vessels, the pressure drops, and the flow changes from being pulsatile to more regular. The veins have the lowest pressure, and the highest volume. The pressure in the pulmonary circuit is much lower than in the systemic circuit. Pulmonary arteries fluctuate by approximately 20 mmHg during the cardiac cycle. Figure 3.2 shows three blood pressure signals recorded simultaneously: arterial pressure, pulmonary arterial pressure, and central venous pressure<sup>2</sup>.

The heart is stimulated electrically through the myocardium, which is the conductive outer layer of the heart. An initial pulse is sent out from the sinoatrial node, which

<sup>2</sup>Data from the Massachusetts General Hospital/Marquette Foundation (MGH/MF) Waveform Database

is located in the right atrium. This pulse activates the heart, and the regular timing of this pulse is the pacemaker of the heart. The atria contract soon afterwards. This pulse travels through the myocardium, where it reaches the atrioventricular node. Here it is delayed through slower conducting tissue, until the second pulse is released, contracting the ventricles.

Measurements of the electrical activity of the heart can be made from the skin surface using a pair of electrodes. These electrodes can be placed in many different configurations, each one of which recording a different angle of the same phenomenon. Typical electrode placement, such as the lead I configuration, measures the potential difference from the left arm to the right arm. Lead II measures the potential difference between the left leg and the right arm. Figure 3.3 shows an example of three ECG leads <sup>3</sup>.

As blood flows into the lungs, and through the capillaries of the lungs, oxygen is exchanged to and from the alveoli via diffusion. The carbon dioxide is forced from the alveoli through the bronchioles and into the trachea by the compression of the lungs. Oxygen is fed into the alveoli through the same pathways, where it diffuses into blood cells. Properties of the lungs that affect breathing and the exchange of oxygen include the elasticity and maximal volume of the lungs. Figure 3.4 shows a respiration signal.

### 3.1.2 Applications for Biological Signals

Biological signals find use in a wide variety of domains. From the above discussion, it is clear that they harbor significant information about the physiological state of the

---

<sup>3</sup>Data from the Massachusetts General Hospital/Marquette Foundation (MGH/MF) Waveform Database

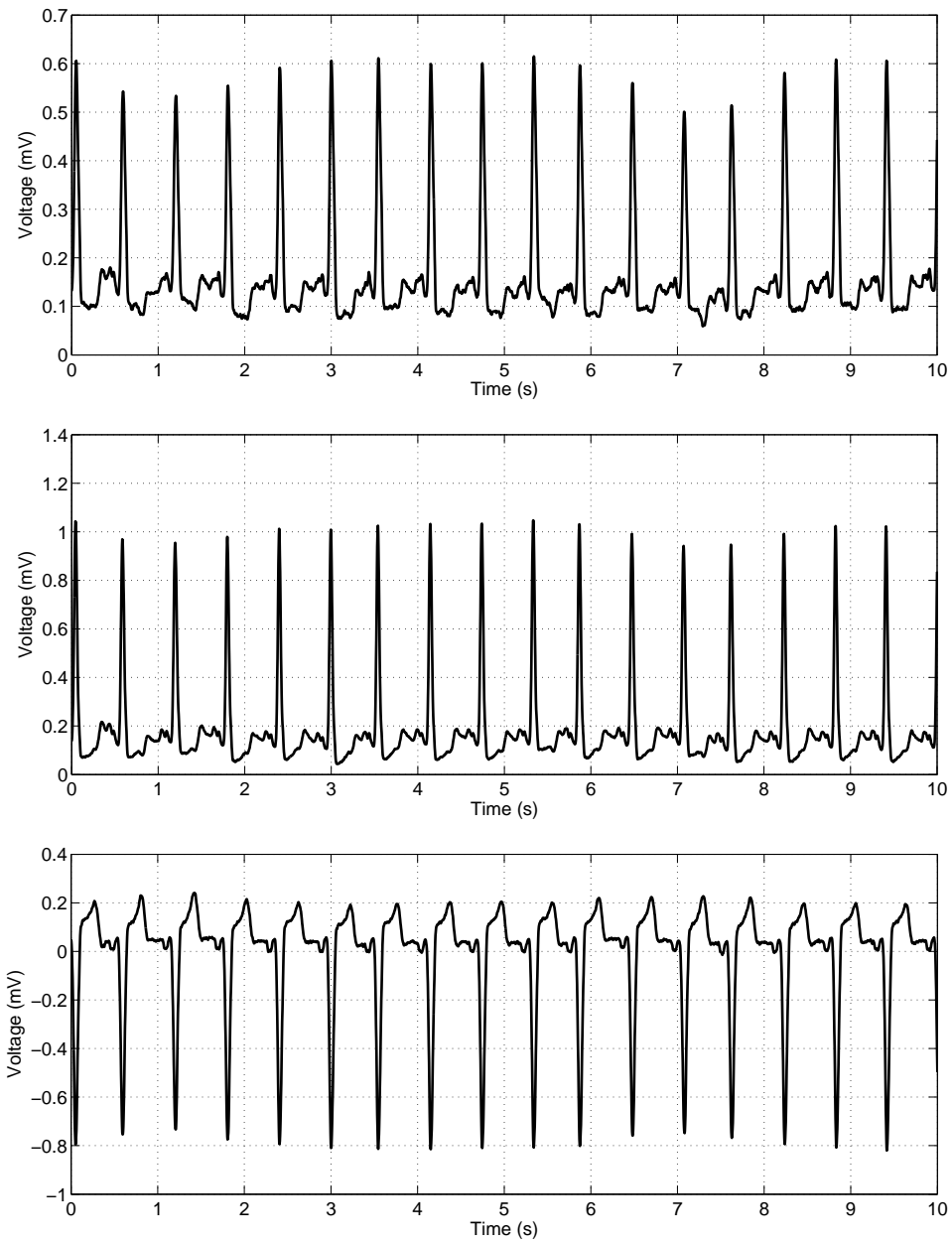


Figure 3.3: Three electrocardiogram channels: (a) lead I, (b), lead II, and (c) lead V.

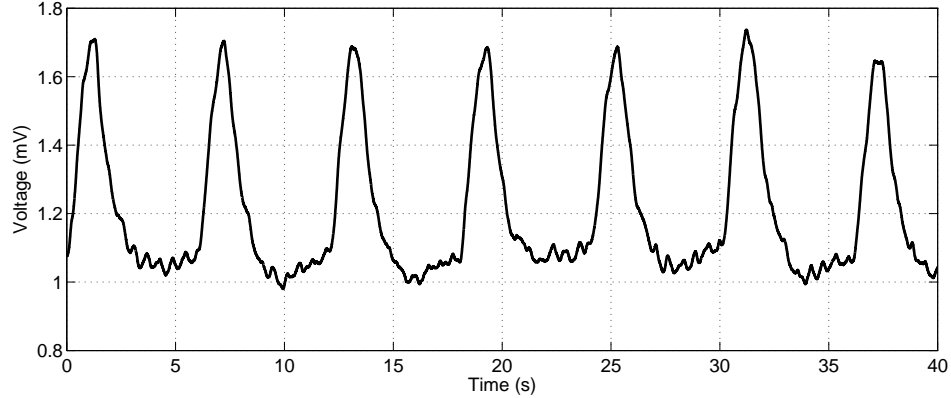


Figure 3.4: A respiration signal.

individual. Depending on the application, this information may be exploited in different ways. For each of the applications described below, a system may be designed that utilizes one or more biological signals to make decisions about an individual. The system may require the use of a human observer, or may operate on an automated basis. Since human judgment is subjective and frequently prone to error, an automated system may perform better. In addition, there are often hidden components to the signals that may require extensive computation to elicit. However, fully computerized systems need to be thoroughly tested before deployment, and require good models for the data.

In clinical settings, biological signals may be used to detect abnormalities, either in terms of universal norms, or with respect to the individual patient. Such systems may operate as one step in a screening process, or they may act exclusively. Operational choices depend on the specific application and the predicted performance of the system. As one example, the ECG may be used to detect ischemic, or abnormal, heart beats. If the sinoatrial node is not firing appropriately, this may be inferred from the ECG. Having models that incorporate the activity of the sinoatrial node is essential for this application.

Another application is in first response scenarios, where an individual may be injured or suffering from an immediate condition. In this case, probing the state of the individual from a distance may be important, especially if the individual is in a precarious environment.

Detecting the onset of disease is often critical for its successful treatment. In some cases, the likelihood of acquiring a disease may be detected and if proper action is taken, it can be avoided entirely. This preventive approach should be a vital part of the health care system. Effectively, this is a transition of monitoring devices and processing tools from the hospital into private homes, and on mobile devices. Due to the proliferation of smaller and faster mobile devices, this possibility is quickly becoming a reality. In this approach, a combination of efficient sensors, smart algorithms, and communication systems combine to form a cohesive health assessment. The use of information processing techniques for biological signals in this application is critical to fully utilize what may be a less than optimal signal, compared to hospital settings.

There are numerous security applications as well. Detecting the state of the individual, whether or not someone is fearful or nervous, for example, using a biological measurement may be of great interest. The body's response to nervousness is wide spread. Blood pressure, for example, rises significantly when the individual is subjected to various types of stressors. Another security application is the verification or detection of identity. Some biological signals may contain individualized aspects, such as respiration patterns, heart rate pattern, and other cardiovascular parameters. In the identity verification scenario, an individual claims a certain identity, and the system needs to either accept or reject this claim on the basis of a measured biological

signal. This problem is addressed using the LDV signal in Chapter 7. In the identity detection scenario, the system needs to identify the individual using biological measurements without any other input.

## 3.2 Motivation for a Structured Modeling Framework

There are a number of approaches that can be taken in designing a system for any of the applications mentioned above. Such a system can be thought of as providing a judgment on the individual on the basis of measured data.

System performance is typically evaluated on the basis of experimental data. If the physiological understanding is thorough and tractable, then the performance may be analytically computed. This is rarely the case for biological signals, since the underlying mechanics are often exceedingly complex. Therefore, for any system, we may predict its performance on the basis of experimental data containing possibly contaminated ground truth. Due to the nearly endless variety of possible systems, we cannot approach the problem of system design merely by trial and error. The search for high performance systems needs to have more structure.

In classical multiclass detection problems where the underlying probability distributions for the classes are known, the optimal decision boundaries may be computed. In the problems of interest, the underlying distributions are not known. In fact, the notion of a true distribution is troublesome. However, if the assumed distributions are close fits to experimental data, then we have a well grounded motivation to use these models in the system.

This provides a link between finding well fitting models and system design for the application of interest. Another advantage of modeling first is that the models may be used in a variety of applications. Also, by starting from simple models and gradually increasing complexity, we can gain an understanding of the underlying process that generates the data, and consequently the use of the models in applications.

Commonalities between biological signals motivate a general framework for signal models. The example signals described above are recorded simultaneously from the same individual, and are driven, in part, by the same complex system. One aim of this work is to develop information processing and modeling techniques that are applicable to a wide variety of biological signals. This requires a basic understanding of the commonality between these signals, which is a hint to the structure of the model.

Cardiovascular signals are semi-periodic. There are segments of the signal that repeat at intervals equal to the inter-beat intervals. Although these segments are not identical, they are often similar. Some of the models developed in this chapter and evaluated in the next chapter capitalize on this periodicity. The respiration pulse is also semi-periodic, at a larger period than the blood pressure and ECG signals. The segments associated with each lung cycle contain information pertaining to the respiratory system. We define each of these segments as a *pulse*, and this is valid both for the cardiovascular and respiratory signals.



### 3.3 Notation for the Data

We consider continuous, real valued signals acquired from an individual from time  $t' = 0$  to  $t' = t_z$ , which can be viewed as the output of a biological system. There may be multiple sessions recorded for the individual. The signal from session  $s$  is denoted  $y_s(t')$ . These signals are sampled and quantized, resulting in the discrete time signals  $y_s[t] = y_s(tT)$ , where  $T$  is the sampling period and  $t \in \{0, 1, 2, \dots, \lfloor \frac{t_z}{T} \rfloor\}$ . The set of signal points from  $t_a$  to  $t_b$  inclusive is denoted as  $y_s[t_a : t_b]$ . If we have multiple sessions, then the data are a set of signals,  $(y_1[t], y_2[t], \dots, y_m[t])$ .

The pulses for session  $s$  occur at times  $p_{s,1}, p_{s,2}, \dots, p_{s,n_s}$ , where  $n_s$  is the number of pulses from session  $s$ . Let their discrete counterparts be  $q_{s,1}, q_{s,2}, \dots, q_{s,n_s}$ , where  $q_{s,i} = \lfloor \frac{p_{s,i}}{T} \rfloor$ . The number of samples in the  $i^{th}$  pulse is  $z_{s,i} = q_{s,i+1} - q_{s,i}$ . In this way, the  $i^{th}$  pulse can be extracted from the signal by  $y_{s,i}[t] = y_s[q_i : q_{i+1} - 1]$ , where  $t = \{0, 1, \dots, z_{s,i} - 1\}$ . When convenient, the time index may also be written as a subscript,  $y_{s,i,t}$ .

If the pulse lengths are identical,  $z = z_{s,i} \forall s, i$ , then the pulses from one session can be organized into a  $z \times n$  data matrix as follows,

$$\mathbf{y}_s = \begin{bmatrix} y_{s,1,0} & y_{s,2,0} & \cdots & y_{s,n,0} \\ y_{s,1,1} & y_{s,2,1} & \cdots & y_{s,n,1} \\ \vdots & \vdots & \ddots & \vdots \\ y_{s,1,z-1} & y_{s,2,z-1} & \cdots & y_{s,n,z-1} \end{bmatrix}.$$

In this case, there are  $mnz$  samples in the data. A single pulse is represented by a column vector as follows,

$$\mathbf{y}_{s,i} = \begin{bmatrix} y_{s,i,0} \\ y_{s,i,1} \\ \vdots \\ y_{s,i,z-1} \end{bmatrix}.$$

Figure 3.5 shows the data hierarchy for  $\mathbf{y}$ . The arrows indicate physiological changes that occur between portions of the data. Red arrows denote changes across sessions, green arrows denote changes across pulses, and blue arrows denote changes within a pulse. These changes are described in the next section.

### 3.4 State Based Modeling

Biological signals depend on many internal properties, which may include factors such as heart rate, arterial stiffness, and breathing phase. In the clinical domain, the goal may be to accurately estimate one or more of these properties in situations where it may not be feasible to measure them directly. In some cases, it may be acceptable to assume that these properties remain constant. For example, the arterial stiffness is not likely to change over the course of several heart beats. If, however, measurements are made over longer periods of time, then the models used should incorporate changes in the underlying arterial properties. We can organize these underlying properties into a hierarchical structure based on their duration of effect. Three such categories are identified:

- Pulse: state changes with a pulse, short term

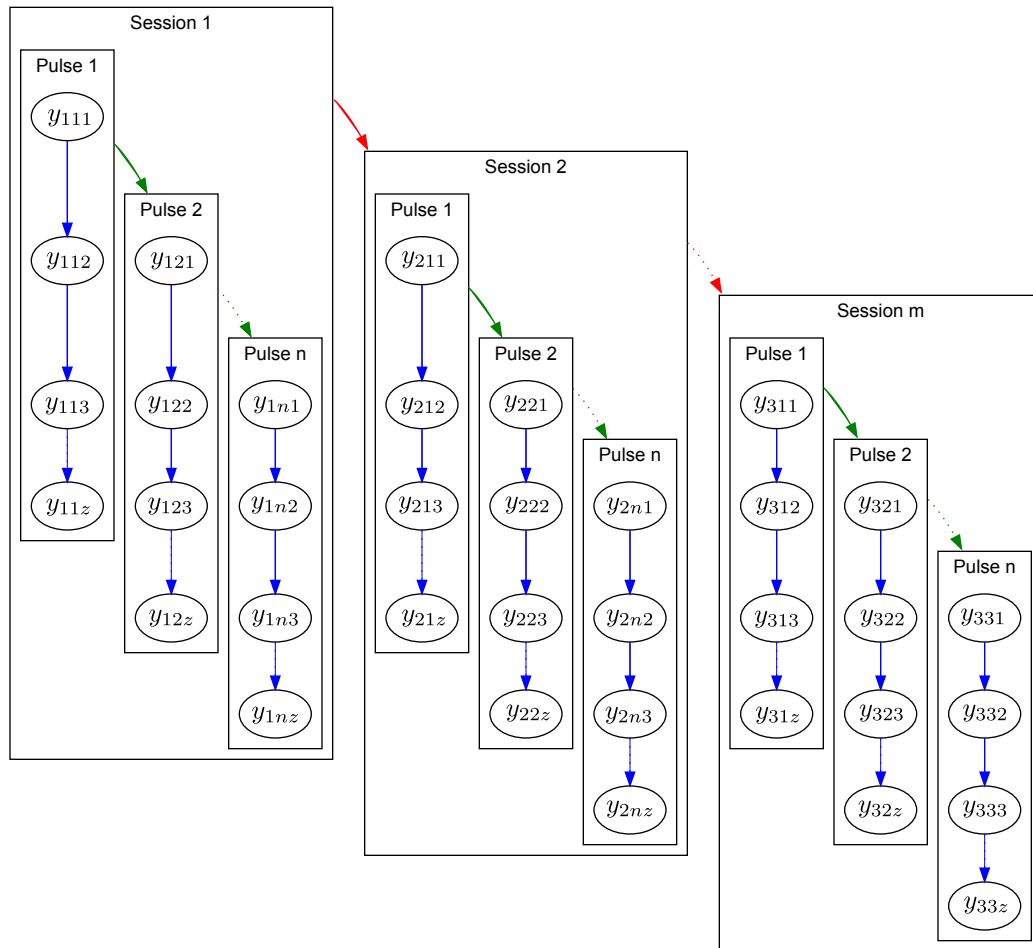


Figure 3.5: Hierarchy of the data.

Pulse	Session	Multisession
Sinoatrial electrical activity	Breathing phase	Drugs
Atrioventricular electrical activity	Heart rate	Weight
Ventricular ejection	Mental stimulation	Arterial plaque
Atrial blood pressure	Physical exercise	Vasculature geometry

Table 3.1: Categorized examples of the underlying properties for biological signals.

- Session: state changes across pulses within one recording session, medium term
- Multisession: state changes across multiple sessions, long term

Table 3.1 contains examples of these categories.

For any point in time, each of these properties has some value associated with it. We may assume that the range of possible values is discrete; in this case, they belong to some state. Over time, the state changes, and it may be possible to infer this change from the measured signal. Collectively, we consider a set of states for each category defined above. We can choose to include any subset of the three categories in a model, so that there may be as many as three state types for each sample of the signal. The state corresponding to  $y_{s,i}[t]$  may be written as a triple:  $x_{s,i}[t] = (x_s, x_i, x_t)$ , where  $x_s \in \mathcal{X}_s$  is the multisession state,  $x_i \in \mathcal{X}_i$  is the session state, and  $x_t \in \mathcal{X}_t$  is the pulse state. We will define probability density functions on portions of the data for each state within a category. Biological signals are dependent on the state of the individual, and their models therefore may need to account for this dependence.

In many cases, it is not practical to measure the state of the individual, although we may be able to measure some of the underlying properties. Thus, they are largely unknown to us. This presents a challenge when trying to model the signals. States that are not directly measured are called hidden states, and ones that are measured are called labeled states. The modeling framework presented in this chapter allows

for a flexible construction of models that attempt to capture a variety of levels of state changes.

A model may be trained from the data, by choosing to incorporate any combination of the three state types. Thus, the model for an individual may contain three submodels. We begin by choosing a model for a single pulse. In the next section, we describe three such models. This model may or may not incorporate pulse states. Then we may choose to include a session model for a sequence of pulses. Not choosing a session model is equivalent to treating the pulses independently. Finally, a multisession model may be chosen. Not choosing a multisession model is equivalent to treating sessions independently.

## 3.5 Models

The models in this section are for testing data  $\mathbf{y}$ , for which there are  $m$  sessions,  $n$  pulses, and  $z$  samples per pulse. Training data,  $\tilde{\mathbf{y}}$ , are used to estimate parameters of the model, for which there are  $\tilde{m}$  sessions,  $\tilde{n}$  pulses, and  $z$  samples per pulse. Three models for a single pulse, one model for a session, and one model for multiple sessions are presented. A total of twelve different models may be constructed using this framework. Table 3.2 lists these models, and organizes them into what state types they are designed to capture.

If desired, the data may initially undergo a preprocessing step, such as a time-frequency decomposition:  $\mathbf{y} \rightarrow \mathbf{y}'$ . This may be useful for some applications, but it does not change the model structure or the estimation algorithm for the parameters. However, the resulting models will be for the data in the processed domain.

State Types	Pulse Model	Session Model	Multisession Model
None	A	-	-
	B	-	-
Pulse	C	-	-
Session	A	D	-
	B	D	-
Pulse & Session	C	D	-
Multisession	A	-	E
	B	-	E
Pulse & Multisession	C	-	E
Session & Multisession	A	D	E
	B	D	E
Pulse, Session, & Multisession	C	D	E

Table 3.2: Eight model types.

Various types of transformations are not considered in this chapter, but are described in the next chapter for LDV data.

The model descriptions below are for hidden states, and estimation procedures make use of the iterative expectation maximization algorithm. Any combination of the state types may be labeled. In this case, the Expectation Maximization (EM) algorithm no longer becomes necessary for that state type. For these cases, the likelihood of the state given the data  $f(x|\tilde{\mathbf{y}})$  terms will be 0 or 1, depending on the label.

Recall that the data  $\mathbf{y}$  consist of  $m$  sessions:  $\mathbf{y} = (\mathbf{y}_1, \mathbf{y}_2, \dots, \mathbf{y}_m)$ . Each session consists of  $n$  pulses:  $\mathbf{y}_s = (\mathbf{y}_{s,1}, \mathbf{y}_{s,2}, \dots, \mathbf{y}_{s,m})$ , and each pulse consists of  $z$  samples:  $\mathbf{y}_{s,i} = y_{s,i,1}, y_{s,i,2}, \dots, y_{s,i,z}$  (see Figure 3.5). Sections 3.5.1, 3.5.2, and 3.5.3 contain descriptions of three different models for the pulse  $\mathbf{y}_{s,i}$ . Section 3.5.4 gives a model for a session, where the pulses may be dependent on hidden or labeled states. The model in Section 3.5.3 uses states that transition in a left to right manner, while the states in the session model may transition to any other state. Finally, Section 3.5.5 contains a similar model for a sequence of sessions that track longer term states.

These models may be combined by choosing a pulse model, and then choosing to include state effects across pulses or sessions. For models with hidden states, the EM algorithm is used [46, 47]. This algorithm requires inference to be performed on the graph using the algorithms presented in Section 2.4.3. For more details on the EM algorithm see Rabiner and Jordan [37, 13].

### 3.5.1 Pulse Model (A)

This model assumes that every sample of the pulse is drawn from a Gaussian random variable,

$$y_{s,i,t} = \mu + \omega_{s,i,t}, \quad (3.1)$$

where the noise term is zero mean Gaussian,  $\omega_{s,i,t} \sim \mathcal{N}(0, \sigma^2)$ . The log density is

$$\ln f(\mathbf{y}; \boldsymbol{\mu}, \sigma^2) = \sum_{s=1}^m \sum_{i=1}^n \sum_{t=1}^z \left( -\frac{1}{2} \ln 2\pi\sigma^2 - \frac{1}{2\sigma^2} (y_{s,i,t} - \mu)^2 \right) \quad (3.2)$$

$$= -\frac{mnz}{2} \ln 2\pi\sigma^2 - \frac{1}{2\sigma^2} \sum_{s=1}^m \sum_{i=1}^n \sum_{t=1}^z (y_{s,i,t} - \mu)^2. \quad (3.3)$$

There are 2 parameters in this model, and they are estimated using the training data:

$$\hat{\mu}(\tilde{\mathbf{y}}) = \frac{1}{\tilde{m}\tilde{n}z} \sum_{s=1}^{\tilde{m}} \sum_{i=1}^{\tilde{n}} \sum_{t=1}^z \tilde{y}_{s,i,t}, \quad (3.4)$$

$$\hat{\sigma}^2(\tilde{\mathbf{y}}) = \frac{1}{\tilde{m}\tilde{n}z - 1} \sum_{s=1}^{\tilde{m}} \sum_{i=1}^{\tilde{n}} \sum_{t=1}^z (\tilde{y}_{s,i,t} - \hat{\mu})^2. \quad (3.5)$$

### 3.5.2 Pulse Model (B)

In this model, the pulse has independent Gaussian components, but they may have different parameters,

$$y_{s,i,t} = \mu_t + \omega_{s,i,t}, \quad (3.6)$$

where the noise terms are zero mean Gaussian,  $\omega_{s,i,t} \sim \mathcal{N}(0, \sigma_t^2)$ . The log density is

$$\ln f(\mathbf{y}; \boldsymbol{\mu}, \boldsymbol{\sigma}^2) = \sum_{s=1}^m \sum_{i=1}^n \sum_{t=1}^z \left( -\frac{1}{2} \ln 2\pi\sigma_t^2 - \frac{1}{2\sigma_t^2} (y_{s,i,t} - \mu_t)^2 \right) \quad (3.7)$$

$$= -\frac{mn}{2} \sum_{t=1}^z \ln 2\pi\sigma_t^2 - \sum_{t=1}^z \frac{1}{2\sigma_t^2} \sum_{s=1}^m \sum_{i=1}^n (y_{s,i,t} - \mu_t)^2. \quad (3.8)$$

Maximum likelihood estimators for the  $2z$  parameters in this model are:

$$\hat{\mu}_t(\tilde{\mathbf{y}}) = \frac{1}{\tilde{m}\tilde{n}} \sum_{s=1}^{\tilde{m}} \sum_{i=1}^{\tilde{n}} \tilde{y}_{s,i,t}, \quad (3.9)$$

$$\hat{\sigma}_t^2(\tilde{\mathbf{y}}) = \frac{1}{\tilde{m}\tilde{n} - 1} \sum_{s=1}^{\tilde{m}} \sum_{i=1}^{\tilde{n}} (\tilde{y}_{s,i,t} - \hat{\mu}_t)^2. \quad (3.10)$$

### 3.5.3 Pulse Model (C)

This model uses an HMM with  $z$  hidden variables,  $\mathbf{x} = (x_1, x_2, \dots, x_z)$  with identical discrete domains:

$$x_t \in \{1, 2, \dots, q\}, \quad (3.11)$$

for any  $t$ . To draw a pulse from this model, the following steps are taken:

1. Draw  $x_1$  from  $f(x_1)$ ,
2. Draw  $x_2, \dots, x_z$  from a Markov chain  $f(x_t|x_{t-1})$ ,



3. Draw samples  $y_{s,i,t}$  from  $\mathcal{N}(\mu_{x_t}, \sigma_{x_t}^2)$  until a pulse is formed.

The model for the pulse given  $\mathbf{x}$  is

$$y_{s,i,t} = \mu_{x_t} + \omega_{x_t}, \quad (3.12)$$

where  $x_1 \rightarrow x_2 \rightarrow \dots \rightarrow x_z$  forms a Markov chain according to  $f(x_1)$  and  $f(x_t|x_{t-1})$ , and  $\omega_k \sim \mathcal{N}(0, \sigma_k^2)$ . The Markov chain is left to right, in the sense that  $f(x_t = l|x_{t-1} = k) = 0$  whenever  $l \neq k$  and  $l \neq k + 1$  (see Figure 3.6). The log density is

$$\ln f(\mathbf{y}; \mathbf{p}, \boldsymbol{\mu}, \boldsymbol{\sigma}^2) = \ln \prod_{s=1}^m \prod_{i=1}^n \sum_{\mathbf{x}} p(\mathbf{x}) \prod_{t=1}^z \frac{1}{\sqrt{2\pi\sigma_{x_t}^2}} e^{-\frac{(y_{s,i,t} - \mu_{x_t})^2}{2\sigma_{x_t}^2}}, \quad (3.13)$$

$$= \sum_{s=1}^m \sum_{i=1}^n \ln \sum_{\mathbf{x}} p(\mathbf{x}) \prod_{t=1}^z \frac{1}{\sqrt{2\pi\sigma_{x_t}^2}} e^{-\frac{(y_{s,i,t} - \mu_{x_t})^2}{2\sigma_{x_t}^2}}. \quad (3.14)$$

The parameters are estimated using the EM algorithm which guarantees convergence to a maximum likelihood estimate,

1. Initialize the parameter estimates:  $\hat{f}^{(0)}(l|k)$ ,  $\hat{\mu}_k^{(0)}$ ,  $\hat{\sigma}_k^{2(0)}$ . Set  $a \rightarrow 1$ .
2. Use the graphical inference algorithm from Section 2.4.3 to compute

$$f(x_t = k, x_{t+1} = l|\tilde{\mathbf{y}}), f(x_t = k|\tilde{\mathbf{y}}).$$

3. Update the parameter estimates by:

$$f(x_t = l | x_{t-1} = k)^{(a)}(\tilde{\mathbf{y}}) = \frac{\sum_{s=1}^{\tilde{m}} \sum_{i=1}^{\tilde{n}} \sum_{t=1}^{z-1} f(x_t = k, x_{t+1} = l | \tilde{\mathbf{y}})}{\sum_{s=1}^{\tilde{m}} \sum_{i=1}^{\tilde{n}} \sum_{t=1}^z f(x_t = k | \tilde{\mathbf{y}})}, \quad (3.15)$$

$$\hat{\mu}_k^{(a)}(\tilde{\mathbf{y}}) = \frac{\sum_{s=1}^{\tilde{m}} \sum_{i=1}^{\tilde{n}} \sum_{t=1}^z f(x_t = k | \tilde{\mathbf{y}}) \tilde{y}_{s,i,t}}{\sum_{s=1}^{\tilde{m}} \sum_{i=1}^{\tilde{n}} \sum_{t=1}^z f(x_t = k | \tilde{\mathbf{y}})}, \quad (3.16)$$

$$\hat{\sigma}_k^{2(a)}(\tilde{\mathbf{y}}) = \frac{\sum_{s=1}^{\tilde{m}} \sum_{i=1}^{\tilde{n}} \sum_{t=1}^z f(x_t = k | \tilde{\mathbf{y}}) (\tilde{y}_{s,i,t} - \hat{\mu}_k)^2}{\sum_{s=1}^{\tilde{m}} \sum_{i=1}^{\tilde{n}} \sum_{t=1}^z f(x_t = k | \tilde{\mathbf{y}})}.$$

4. Set  $a \rightarrow a + 1$ . Check for convergence. Go to step 2.

In the case when the states  $\mathbf{x}$  are labeled, the conditional distributions  $f(x_t = k, x_{t+1} = l | \tilde{\mathbf{y}})$ ,  $f(x_t = k | \tilde{\mathbf{y}})$  are indicator functions taking on the following values:

$$f(x_t = k | \tilde{\mathbf{y}}) = \begin{cases} 0, & x_t \neq k, \\ 1, & x_t = k, \end{cases} \quad (3.17)$$

$$f(x_t = k, x_{t+1} = l | \tilde{\mathbf{y}}) = \begin{cases} 0, & (x_t, x_{t+1}) \neq (k, l), \\ 1, & (x_t, x_{t+1}) = (k, l). \end{cases} \quad (3.18)$$

The above EM algorithm iterations turn into a single step, where the parameters are weighted combinations of the labeled samples.

### 3.5.4 Session Model (D)

These are models for a sequence of pulses that capture variability from pulse to pulse, and they require that one of the three pulse models is used. To draw a pulse from this model, the following steps are taken:

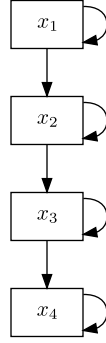


Figure 3.6: HMM topology for Model C.

1. Draw  $x_1, x_2, \dots, x_n$  from a Markov chain  $f(x_t|x_{t-1})$ .
2. Draw pulses  $\mathbf{y}_{s,i}$  from a pulse model with parameters  $\theta'_{x_i}$ .

The Markov chain is full, in the sense that  $f(l|k) \neq 0$  for all  $k, l$ . The log density is

$$\ln f(\mathbf{y}; \mathbf{p}, \boldsymbol{\mu}, \sigma^2) = \ln \prod_{s=1}^m \sum_{\mathbf{x}} p(\mathbf{x}) \prod_{i=1}^n f(\mathbf{y}_{s,i}; \theta_{x_i}), \quad (3.19)$$

$$= \sum_{s=1}^m \ln \sum_{\mathbf{x}} p(\mathbf{x}) \prod_{i=1}^n f(\mathbf{y}_{s,i}; \theta_{x_i}). \quad (3.20)$$

The parameters are estimated using the expectation maximization algorithm,

1. Initialize the parameter estimates:  $\hat{f}^{(0)}(l|k), \theta_k^{(0)}$ .
2. Use the graphical inference algorithm to compute:  $f(x_t = k, x_{t+1} = l|\tilde{\mathbf{y}}), f(x_t = k|\tilde{\mathbf{y}})$ .
3. Update the parameter estimates by:

$$\hat{p}(x_t = l|x_{t-1} = k) = \frac{\sum_{s=1}^{\tilde{m}} \sum_{i=1}^{\tilde{n}} f(x_i = k, x_{i+1} = l|\tilde{\mathbf{y}})}{\sum_{s=1}^{\tilde{m}} \sum_{i=1}^{\tilde{n}} f(x_i = k|\tilde{\mathbf{y}})}, \quad (3.21)$$

$$\hat{\theta}_k = \frac{\sum_{s=1}^{\tilde{m}} \sum_{i=1}^{\tilde{n}} f(x_i = k|\tilde{\mathbf{y}}) \hat{\theta}'_k(\tilde{\mathbf{y}}_{s,i})}{\sum_{s=1}^{\tilde{m}} \sum_{i=1}^{\tilde{n}} f(x_i = k|\tilde{\mathbf{y}})}. \quad (3.22)$$

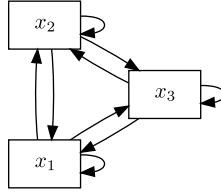


Figure 3.7: HMM topology for Models D and E.

This step requires estimating parameters in a pulse model (either A, B, or C).

For clarity, the estimates are repeated here for models A and B:

$$\text{Model A: } \hat{\theta}'_k(\tilde{\mathbf{y}}_{s,i}) = \frac{1}{z} \sum_{t=1}^z y_{s,i,t}, \quad (3.23)$$

$$\text{Model B: } \hat{\theta}'_k(\tilde{\mathbf{y}}_{s,i}) = \mathbf{y}_{s,i}. \quad (3.24)$$

Model C requires another EM algorithm to be performed.

4. Check for convergence. Go to step 2.

### 3.5.5 Multisession Model (E)

These are models for a sequence of sessions. One of the session models is embedded.

To draw a pulse from this model, the following steps are taken:

1. Draw  $x_1, x_2, \dots, x_m$  from a Markov chain  $f(x_t|x_{t-1})$ .
2. Draw sessions  $\mathbf{y}_s$  from a session model with parameters  $\theta'_{x_s}$ .

The Markov chain is full, in the sense that  $f(l|k) \neq 0$  for all  $k, l$ . The log density is

$$\ln f(\mathbf{y}; \mathbf{p}, \boldsymbol{\mu}, \sigma^2) = \ln \sum_{\mathbf{x}} p(\mathbf{x}) \prod_{s=1}^m f(\mathbf{y}_s; \theta_{x_s}). \quad (3.25)$$

The parameters are estimated using the expectation maximization algorithm,

1. Initialize the parameter estimates:  $\hat{p}^{(0)}(l|k)$ ,  $\theta_k^{(0)}$ .
2. Use the graphical inference algorithm to compute:  $f(x_t = k, x_{t+1} = l|\tilde{\mathbf{y}})$ ,  $f(x_t = k|\tilde{\mathbf{y}})$ .
3. Update the parameter estimates by:

$$\hat{p}(l|k) = \frac{\sum_{s=1}^{\tilde{m}} f(x_s = k, x_{s+1} = l|\tilde{\mathbf{y}})}{\sum_{s=1}^{\tilde{m}} f(x_s = k|\tilde{\mathbf{y}})}, \quad (3.26)$$

$$\hat{\theta}_k = \frac{\sum_{s=1}^{\tilde{m}} f(x_s = k|\tilde{\mathbf{y}}) \hat{\theta}'_k(\tilde{\mathbf{y}}_s)}{\sum_{s=1}^{\tilde{m}} f(x_i = k|\tilde{\mathbf{y}})}. \quad (3.27)$$

This step requires estimating parameters in session model D, which in turn requires estimating parameters in a pulse model.

4. Check for convergence. Go to step 2.

# Chapter 4

## Laser Doppler Vibrometry

### Measurements of the Carotid Pulse

A Laser Doppler Vibrometer (LDV) is a device which measures surface velocity on the basis of the Doppler shift. A laser is targeted on the surface, and the change in frequency of the reflected light is proportional to the velocity of the surface in the direction of the beam. This reflected light is sensed in the same device. Laser Doppler techniques have found use in measuring blood flow, called laser Doppler flowmetry, for some time. This method requires contact with the subject, but is noninvasive, and works by measuring the Doppler shift from illuminated blood cells traveling through live tissue [48]. Some applications of this method include gastrointestinal [49], head [50], and peripheral measurements of blood perfusion [51]. Aside from measuring blood flow, laser Doppler techniques for measuring tissue surface velocity have not been as common. One exception is the study of inner ear disorders [52, 53, 54]. In [55], contact technique for measuring skin vibration is described. Experiments using a noncontact LDV were performed in [56], in which quantitative comparisons were made with electrocardiograms.

## 4.1 Data Acquisition

A Polytec PSV-400 LDV with a 633 nm wavelength laser is targeted at a site on the neck overlying the right carotid artery. This device uses a class II eye-safe laser. We have chosen this site because we are able to detect a strong signal there. The proximity of the carotid to the skin surface means that mechanical energy may be sensed at the skin surface that originates from within the carotid due to the underlying blood flow. A small patch of reflective tape was used to enhance the signal quality, although subsequent tests without the tape indicate that the signal quality is nearly identical in both cases.

Subjects were enrolled in this study with informed consent according to the regulation of the IRB through Washington University School of Medicine. Broad health information, including drug use, and history were recorded from all subjects. The subjects varied in age between 18 and 66 years, and in demographics. After a brief initial resting period, the recording sessions lasted 5 minutes, with the subjects at rest during recording. The second session was recorded approximately one month after the first, and a third session was recorded approximately five months after the second. A total of 142 subjects are used from this protocol.

Another protocol was used in which a strain gauge is applied over the abdomen for breathing information. The same LDV was used on 43 subjects for this protocol (22 females) ranging in age from 20 to 29 years, all non-smokers, with BMIs  $< 30$ , and free from cardiovascular, pulmonary or other major diseases.

## 4.2 Biological Basis

As a major vessel in the arterial tree, the carotid harbors significant information of central cardiovascular activity. Its proximity to the skin surface makes it accessible and thus an ideal targeting site. Mechanical vibrations, resulting from the underlying blood flow and pressure waves in combination with the elasticity of the carotid walls contribute to the measured signal. Other sources of mechanical activity are also sensed, including activity from other parts of the body that is transmitted internally to the measurement site, such as heart sounds. A variety of other movements including those associated with respiration, speech and gross movements of the head, neck, and body are also recorded.

Blood flow is a wave-like phenomenon in which a pressure wave originates from the heart and travels through the arterial tree [57]. The wave speed varies across the vasculature and is dependent on the elasticity of the arterial walls, but is typically 5 m/s on average, while the blood flow itself is at a much slower speed. Many of the arteries are elastic vessels, and stretch and contract in accordance with the underlying pressure. The pressure wave is reflected in numerous locations along its path due to discontinuities and bifurcations, and the resulting pressure at a given location is the constructive interference of multiple overlapping waves. Thus, the pressure waveform contains significant information that is both clinically relevant and specific to the individual. Information about the vessel wall elasticity and blockage that may be causing extra reflections may be inferred from the pressure. The LDV signal is not a direct pressure measurement, but it is clinically relevant. Quantitatively connecting the measured signal with the underlying pressure is an important aim

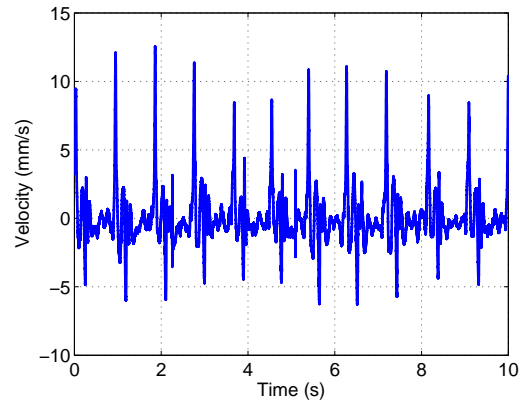


for the development of this technology. Analysis that contributes in this direction is presented in Chapter 6.

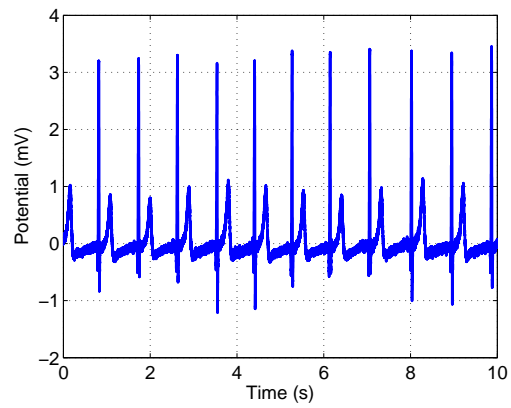
### 4.3 Signal

A typical carotid LDV recording is shown in Figure 4.1, along with a simultaneous ECG recording and a measurement of radial blood pressure. Most of the power in the signal is contained within the band 0 Hz - 100 Hz, and there is approximately a 50 dB drop across this band [58]. Each of the large velocity peaks in the data corresponds to the initial activity of each heartbeat. Portions of the data which correspond to the activity of a single heartbeat can be extracted, either in an automated basis relying on LDV pulse signal features, or with the aid of an external signal, such as a simultaneous electrocardiogram. These segments are called *LDV velocity pulses*, or simply *LDV pulses*.

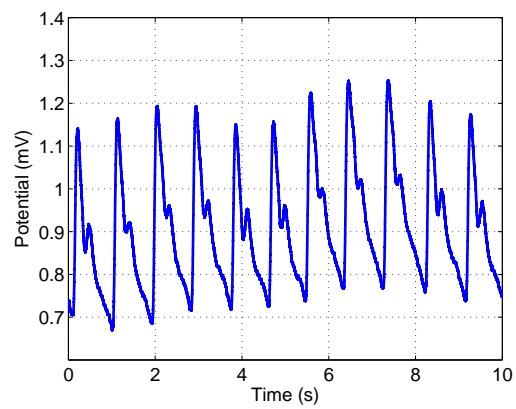
A prominent feature of the LDV pulse is the initial velocity peak coinciding with the ejection of blood from the left ventricle. Figure 4.2 shows a single normalized LDV pulse, and its normalized displacement pulse, called the *LDV displacement pulse*, computed by taking the cumulative sum of the LDV velocity pulse. The LDV displacement pulse is similar in shape to an arterial blood pressure waveform [59, 60], and indeed shares many similarities to the underlying blood pressure pulse. In some studies, the pressure-radius relationship in the carotid has been experimentally shown to be approximately linear [61, 62]. This assumption is analytically explored through the physics of fluid dynamics in Chapter 6. Due to the proximity (in many cases) of the carotid wall to the skin surface, we expect that the LDV-sensed changes in displacement associated with the pressure pulse will track the changes in the carotid's



(a)



(b)



(c)

Figure 4.1: Ten seconds of three signals recorded simultaneously: (a) carotid LDV signal, (b) ECG, (c) radial blood pressure.

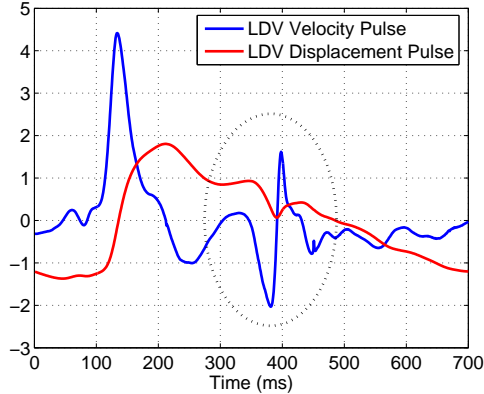
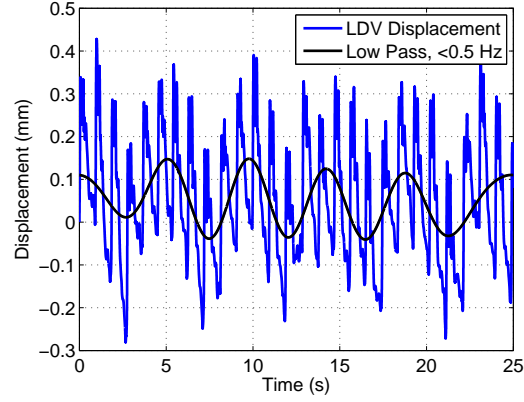


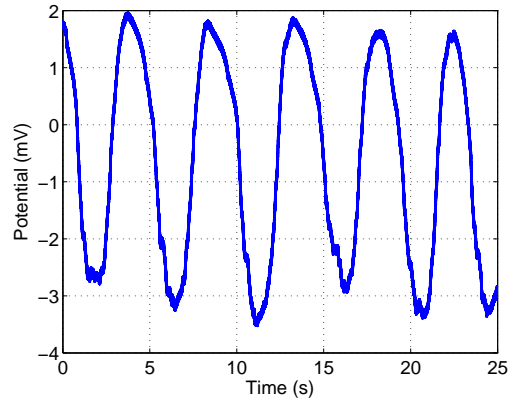
Figure 4.2: An LDV velocity pulse and its corresponding LDV displacement pulse. Both have been normalized by their sample means and sample standard deviations.

radius, and therefore of the underlying blood pressure profile. This observation is further strengthened by considering physiologically relevant attributes that can be extracted from the LDV pulse, such as an approximate measure of the left ventricular ejection time (LVET). LVET is the time interval between the opening and closing of the aortic valve. We do not measure the LVET directly; instead we make inferences about it from the form of the LDV pulses. The segment of the pulse waveform corresponding to the closing of the aortic valve is marked in Figure 4.2 with a dotted circle. We adopt the convention of labeling the pressure event associated with aortic valve closure (i.e., end of the LVET) the *incisura*. The time interval between the initial upstroke of the displacement waveform and the small notch corresponding to the incisura can be used to approximate the LVET.

Over longer time intervals, breathing activity may be sensed in the LDV signal. This activity is in a low frequency (approximately  $<0.5$  Hz) portion of the signal, and may be seen from the displacement waveform. The displacement is computed by taking the cumulative sum of the velocity signal. In Figure 4.3, an LDV displacement signal



(a)



(b)

Figure 4.3: Breathing activity in the LDV signal and a strain gauge: (a) an LDV displacement signal over 25 seconds and the low frequency component, (b) a strain gauge measurement over the abdomen.

and a simultaneous strain gauge placed over the abdomen are shown. The strain gauge is used to measure respiratory effort.

Systematic changes are observed in the LDV pulse waveform from beat to beat, including changes in the duration of LVET. In individuals at rest, this variability is attributed to the respiration cycle, consistent with the hemodynamic changes associated with inspiration and expiration. These effects are apparent only when the

pulse signals are studied on a beat-to-beat basis, and are obscured by ensemble averaging. There are other changes over successive pulses, varying in time course and arising from multiple factors including autoregulatory reflexes, stress and metabolic demands. The state of the individual, which refers to an unknown physiological condition associated with each pulse, may change slowly or rapidly, and is inferred from the measured signal.

## 4.4 Preprocessing

The LDV signal is sampled at 10 kHz, and downsampled to 1 kHz. A template matching algorithm is used to extract LDV pulses. In some cases, manual adjustments to the detection of the main peaks are made as necessary.

For some models, a short-time frequency decomposition is used. The goal is to construct an instantaneous representation of the frequency contents of a signal. This requires a synthesis window over which the Fourier transform is computed. There is an intrinsic trade off between frequency resolution and time resolution. As the window size increases, the frequency resolution increases, but the time resolution decreases. On the other hand, as the window becomes shorter, the time resolution improves at the expense of worse frequency resolution. Short-Time Fourier Transform (STFT) methods have found application in many areas, such as speech processing.

The STFT is computed by,

$$X(nL, \omega) = \sum_{t=-\infty}^{\infty} x[t] w[nL - t] e^{-j\omega t}, \quad (4.1)$$

where  $w[n]$  is the window and  $L$  is the window shift. The window is nonzero inside some support  $T$ ,  $w[n] \neq 0$  for  $-T < n < T$ . Since the STFT is an invertible operation, we can reconstruct the original signal from its STFT, as long as  $L < T$ . We will often use the magnitude STFT, defined by,

$$S(nL, \omega) = \left| \sum_{t=-\infty}^{\infty} x[t] w[nL - t] e^{-j\omega t} \right|. \quad (4.2)$$

Sufficient conditions for signal reconstruction from the magnitude STFT [63] are:

1. The window shift must be less than half of the window support:  $L \leq \lfloor \frac{T}{2} \rfloor$ ,
2. The window length is greater than 2:  $T > 2$ ,
3. The signal  $x[t]$  is one-sided,
4. The signal  $x[t]$  has at most  $T - 2L$  consecutive zeros between any two nonzero samples,
5. The first  $L$  samples of  $x[t]$  are known, starting from the first nonzero samples.

These are not necessary conditions, but they are mild.

Three popular types of windows are the Gaussian, Hamming and Nuttall windows. They are given by,

$$\text{Gaussian:} \quad w(n) = e^{-\frac{1}{2} \left( \alpha \frac{n-1-\frac{N}{2}}{N/2} \right)^2}, \quad (4.3)$$

$$\text{Hamming:} \quad w(n) = 0.54 - 0.46 \cos \frac{2\pi n}{N-1}, \quad (4.4)$$

$$\text{Nuttall:} \quad w(n) = a_0 - a_1 \cos \frac{2\pi n}{N-1} + a_2 \cos \frac{4\pi n}{N-1} - a_3 \cos \frac{6\pi n}{N-1}.$$

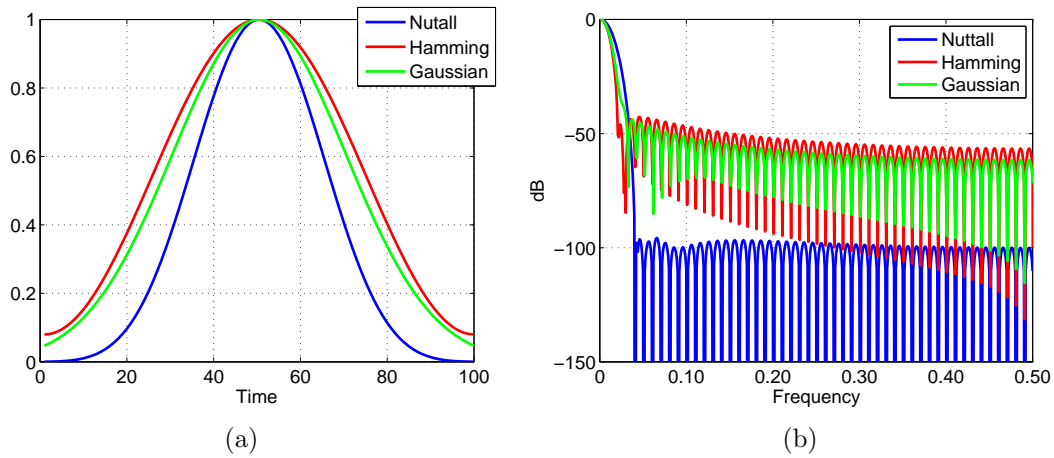


Figure 4.4: The Gaussian, Hamming, and Nuttall windows are shown in (a), and their spectra are shown in (b).

The values for the constants that are typically used are

$$\alpha = 2.5,$$

$$a_0 = 0.355768,$$

$$a_1 = 0.487396,$$

$$a_2 = 0.144232,$$

$$a_3 = 0.012604.$$

Each of these windows trades off time resolution for frequency resolution. Figure 4.4 shows the three windows and their spectra. Of these windows, the Nuttall window has the highest time resolution, but the lowest frequency resolution. An advantage of this window, however, is that it has small sidelobes. The Hamming window has the lowest time resolution and the highest frequency resolution. The Gaussian window is in between the Nuttall and Hamming windows in both time and frequency resolution. The Nuttall window is used in the spectral methods in this dissertation.

# Chapter 5

## Experimental Evaluation of Models for Laser Doppler Vibrometry

Based on the framework presented in Chapter 3, we consider 7 models, encompassing the three types of state transitions described in that chapter. Each of the models is trained and tested on the LDV data for each of the 142 individuals, over various training and testing conditions. Table 5.1 lists these models, as well as the preprocessing performed on the data, if any. The type refers to the combination of models from the previous chapter. The states are assumed to be either hidden or labeled; since we have only three sessions, we assume that the multisession states are labeled.

Model	Preprocessing	Type	Pulse States	Session States	Multisession States
$LDV_A$	none	A	-	-	-
$LDV_B$	none	B	-	-	-
$LDV_{BE}$	none	BE	-	-	Labeled
$LDV_C$	STFT	C	Hidden	-	-
$LDV_{CE}$	STFT	CE	Hidden	-	Labeled
$LDV_{BD}$	none	BD	-	Hidden	-
$LDV_{BDE}$	none	BDE	-	Hidden	Labeled

Table 5.1: Modeled trained and tested on LDV data.



	Session 1a	Session 1b	Session 2a	Session 2b	Session 3a	Session 3b
$S_{1,1}$	Train (48)	Test (48)				
$S_{1,2}$	Train (48)			Test (48)		
$S_{1,3}$	Train (48)					Test (48)
$S_{2,2}$			Train (48)	Test (48)		
$S_{2,3}$			Train (48)			Test (48)
$S_{3,3}$					Train (48)	Test (48)
$S_{12,2}$	Train (24)		Train (24)	Test (48)		
$S_{12,3}$	Train (24)		Train (24)			Test (48)
$S_{13,3}$	Train (24)				Train (24)	Test (48)
$S_{23,3}$			Train (24)		Train (24)	Test (48)
$S_{123,3}$	Train (12)		Train (12)		Train (12)	Test (48)

Table 5.2: Training and testing schedules.

For model evaluation, each session is divided into two halves ('a' and 'b') of 48 pulses each. We use the training and testing schedule shown in Table 5.2 for each of the 7 models. The numbers in parenthesis are the number of pulses used from that session for either training or testing purposes. In cases where multiple sessions are used for training, the 48 pulses are divided evenly among the training sessions. There are 11 training and testing schedules, with 7 unique training sets resulting in a total of 49 unique models. To denote a specific model and schedule combination, we use a dash between the model name and the schedule number. For example, Model  $LDV_A$  trained on schedule  $S_{1,1}$  is denoted  $LDV_A - S_{1,1}$ . The variety of training and testing schedules allows us to compare how the models perform in varying conditions.

For a given model, the following steps are performed to evaluate the model fit:

1. Perform a preprocessing step, if any, on the training data:  $\tilde{\mathbf{y}} \rightarrow \tilde{\mathbf{y}}'$ ,
2. Estimate the model parameters using the estimation technique from Chapter 3:  
 $\hat{\theta}(\tilde{\mathbf{y}}')$ ,

3. Perform the same preprocessing step, if any, on the testing data:  $\mathbf{y} \rightarrow \mathbf{y}'$ ,
4. Compute the loglikelihood of the testing data given the trained model:  $L_s = \log f(\mathbf{y}'|\hat{\theta})$ .

The loglikelihood is a quantity that can be used to compare models with the same preprocessing and that are tested on the same number of samples. Greater values denote better fit. Table 5.3 shows the average loglikelihood score per sample across the 142 individuals for the time domain models. The best models within session are the  $LDV_{BD}$  and  $LDV_{BDE}$  models. Across sessions, the best model is the  $LDV_B$  model. The multisession models (E) do not help much. In fact training on two sessions and testing on the second session is equally good on average when training only on the second session. Training on two sessions and testing on the third, however, improves the fit compared to training on only one session.

Confidence intervals are computed to provide a measure of accuracy, giving a 95% confidence interval for each score. These are computed by assuming that the scores computed from different individuals are independent. Since we assume that the scores are independent,  $L$  will be approximately Gaussian by the central limit theorem. The 95% confidence interval is computed by,  $\hat{\mu} \pm 2\hat{\sigma}$ , where  $\hat{\mu}$  is the mean score for an individual, and  $\hat{\sigma}$  is the sample standard deviation. The next chapter contains a broader analysis of confidence intervals in the case of dependent samples for identity verification. Table 5.4 shows the 95% confidence intervals for each of the models.

Model	$S_{1,1}$	$S_{1,2}$	$S_{1,3}$	$S_{2,2}$	$S_{2,3}$	$S_{3,3}$	$S_{12,2}$	$S_{12,3}$	$S_{13,3}$	$S_{23,3}$	$S_{123,3}$
$LDV_A$	-8.8	-8.8	-9.0	-8.8	-9.0	-9.0	-8.8	-9.0	-9.0	-9.0	-9.0
$LDV_B$	-6.6	-7.4	-7.5	-6.6	-7.4	-6.6	-6.7	-7.1	-6.8	-6.8	-6.8
$LDV_{BE}$	-	-	-	-	-	-	-6.6	-7.2	-6.6	-6.6	-6.6
$LDV_{BD}$	-6.5	-7.8	-7.9	-6.5	-7.9	-6.5	-6.6	-7.4	-6.7	-6.6	-6.7
$LDV_{BDE}$	-	-	-	-	-	-	-6.5	-7.5	-6.5	-6.5	-6.5

Table 5.3: Average model fit in loglikelihood per sample for the 11 training and testing schedules for time domain models.

Model	$S_{1,1}$	$S_{1,2}$	$S_{1,3}$	$S_{2,2}$	$S_{2,3}$	$S_{3,3}$
$LDV_A$	$\pm 2.2$	$\pm 3.0$	$\pm 3.0$	$\pm 3.0$	$\pm 3.0$	$\pm 3.0$
$LDV_B$	$\pm 0.6$	$\pm 1.7$	$\pm 1.5$	$\pm 0.6$	$\pm 1.8$	$\pm 0.6$
$LDV_{BE}$	-	-	-	-	-	-
$LDV_{BD}$	$\pm 0.6$	$\pm 2.9$	$\pm 2.4$	$\pm 0.6$	$\pm 2.8$	$\pm 0.6$
$LDV_{BDE}$	-	-	-	-	-	-

Model	$S_{12,2}$	$S_{12,3}$	$S_{13,3}$	$S_{23,3}$	$S_{123,3}$
$LDV_A$	$\pm 3.0$	$\pm 3.0$	$\pm 3.0$	$\pm 3.0$	$\pm 3.0$
$LDV_B$	$\pm 0.6$	$\pm 1.1$	$\pm 0.5$	$\pm 0.6$	$\pm 0.5$
$LDV_{BE}$	$\pm 0.6$	$\pm 1.2$	$\pm 0.6$	$\pm 0.6$	$\pm 0.6$
$LDV_{BD}$	$\pm 0.7$	$\pm 1.8$	$\pm 0.6$	$\pm 0.6$	$\pm 0.6$
$LDV_{BDE}$	$\pm 0.6$	$\pm 1.8$	$\pm 0.6$	$\pm 0.6$	$\pm 0.6$

Table 5.4: Confidence intervals for the 11 training and testing schedules for time domain models.

## 5.1 Model $LDV_A$

The first model,  $LDV_A$  uses Pulse Model A with no session or multisession model. This is a two parameter model, where the data  $y$  are assumed to be generated by Equation 3.1. The fit for this model is the lowest of all the models, and the loglikelihoods are fairly consistent when training and testing on distinct sessions. Figure 5.1 shows score histograms for models  $S_{1,1}$  and  $S_{1,2}$ . The similarity between these histograms indicates that the fit is consistent across sessions, as can also be seen from Table 5.3. The bottom histogram in the figure shows how many more individuals from the  $S_{1,1}$  test there are than from the  $S_{1,2}$  for each score bin.

## 5.2 Model $LDV_B$

Model  $LDV_B$  uses Pulse Model B without any preprocessing. Figure 5.2 shows histograms from  $S_{1,1}$  and  $S_{1,2}$ . The scores from  $S_{1,2}$  are generally lower than those from  $S_{1,1}$ , showing the decrease in fit across sessions. Thus the improvement in fit over model  $LDV_A$  comes at the expense of a decrease in fit across sessions, although the fit across sessions for this model is higher than the fit within session under  $LDV_A$ .

To gain further insight, the best and worst fits for model  $LDV_B - S_{1,2}$  are examined. The best performing individual for  $LDV_B - S_{1,2}$  is examined in Figure 5.3. The first subfigure shows the model means along with pulses from the same session, while the second subfigure shows the same means with pulses from the second session. For this individual the score for  $LDV_B - S_{1,1}$  is -6.2, and the score for  $LDV_B - S_{1,2}$  is -6.3, which is only a slight decrease. This across sessions fit is better than most individuals had within session.

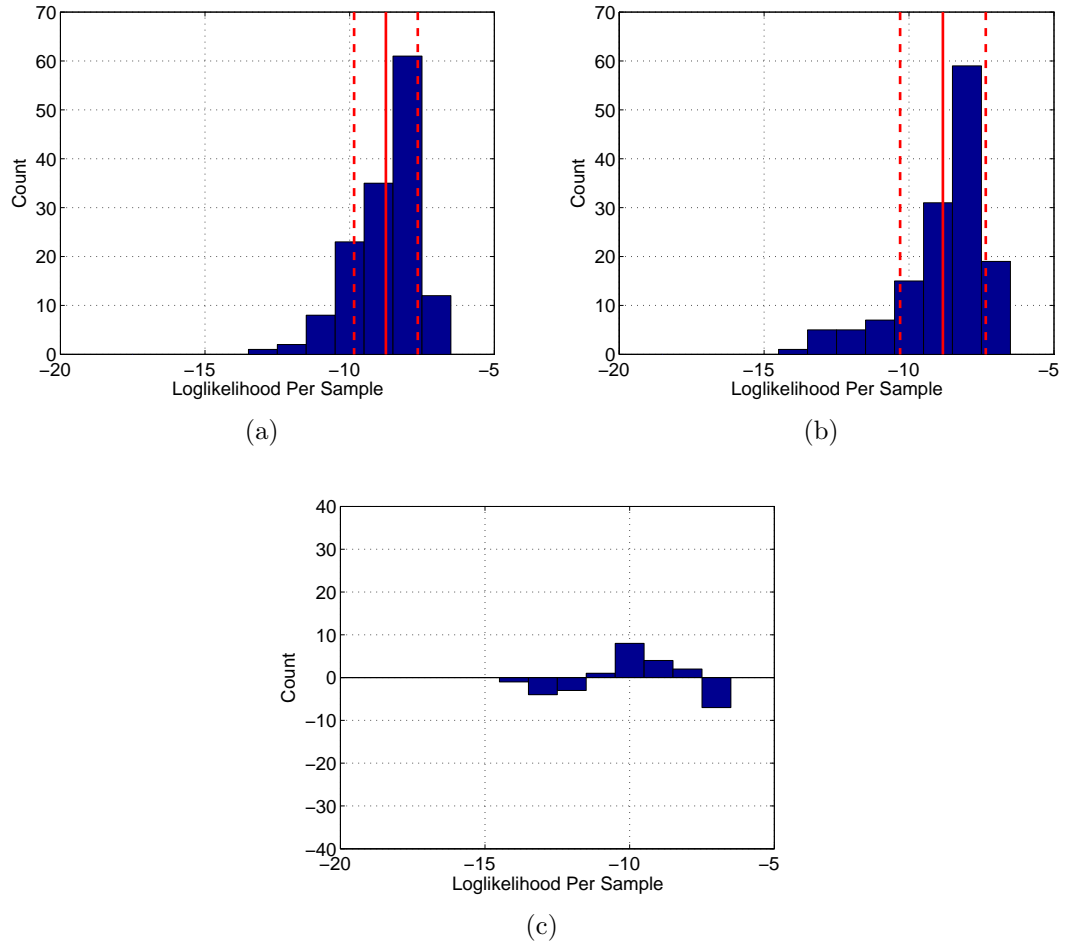


Figure 5.1: Histograms across individuals for (a) model  $LDV_A - S_{1,1}$ , and (b) model  $LDV_A - S_{1,2}$ . The histogram in (c) shows how many more individuals for  $LDV_A - S_{1,1}$  there are than  $LDV_A - S_{1,2}$  in each score bin.

The worst performing individual for  $LDV_B - S_{1,2}$  is examined in Figure 5.4. For this individual the score for  $LDV_B - S_{1,1}$  is -6.6, and the score for  $LDV_B - S_{1,2}$  is -11.2. This within session fit is the average fit within session. The reduction in fit across sessions can be seen in the figure.

### 5.3 Model $LDV_C$

Model  $LDV_C$  uses Pulse Model C with 6 states, and a magnitude STFT in the preprocessing step. This model is designed to track state changes within a pulse. A Nuttall window was used, computing FFTs over 96 ms windows, sliding by 1 ms at a time. Frequency bins up to 150 Hz were retained, resulting in 15 points that are computed under each window frame. The number of states was chosen to account for the main peak, the *insicura*, and time periods before and after these events.

#### 5.3.1 Interpretation of Model $LDV_C$

This model tracks state changes within a pulse in the magnitude STFT domain. The mean training pulse for one individual along with its spectrum are shown in Figure 5.5. The pulse has been rescaled and shifted for presentation purposes.

After the model is trained, we then compute the most likely state sequence of the mean pulse using the max-product algorithm from Chapter 2. The pulse has been color coded according to the state sequence in Figure 5.6. In addition, the state transition probability matrix is shown. The algorithm partitions the pulse into sections according to the model.

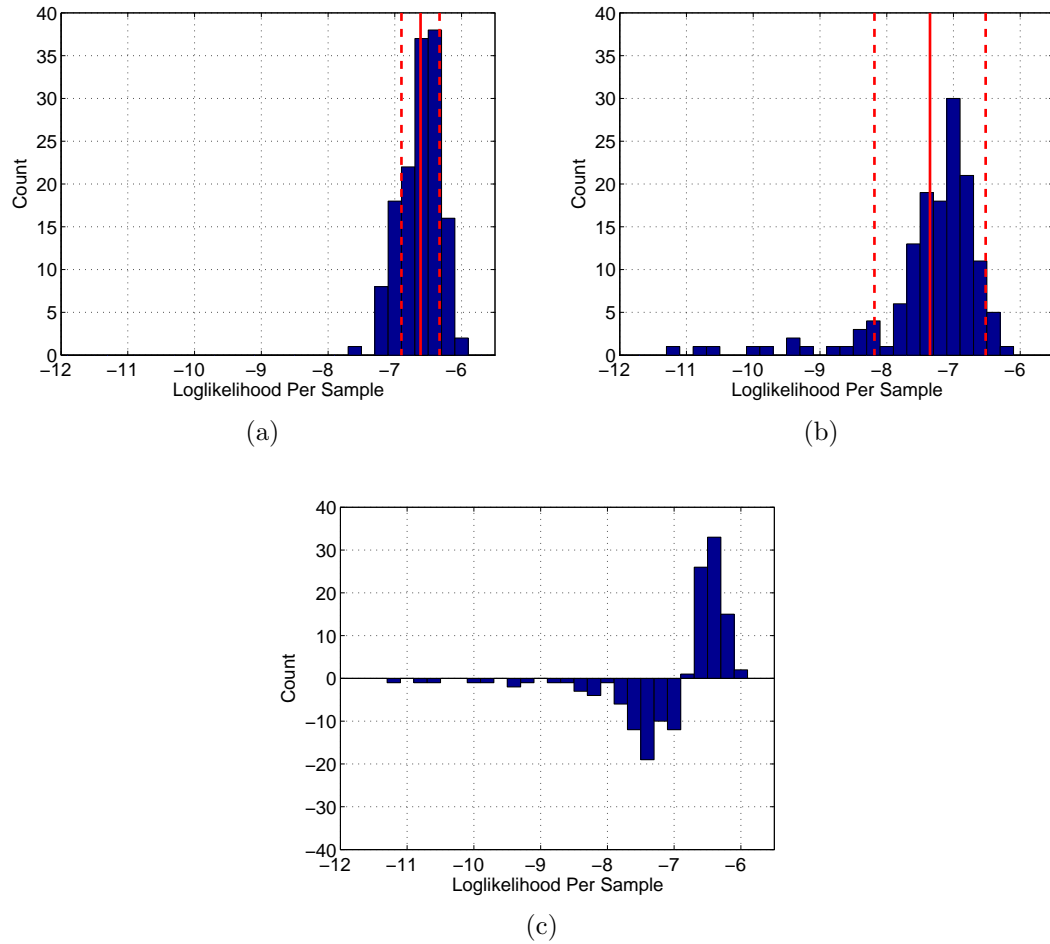


Figure 5.2: Histograms across individuals for (a) model  $LDV_B - 1$ , and (b) model  $LDV_B - 2$ . The solid red lines indicate the mean score and the dotted red line show a standard deviation away from the mean. The histogram in (c) shows how many more individuals for  $LDV_B - 1$  there are than  $LDV_B - 2$  in each score bin.

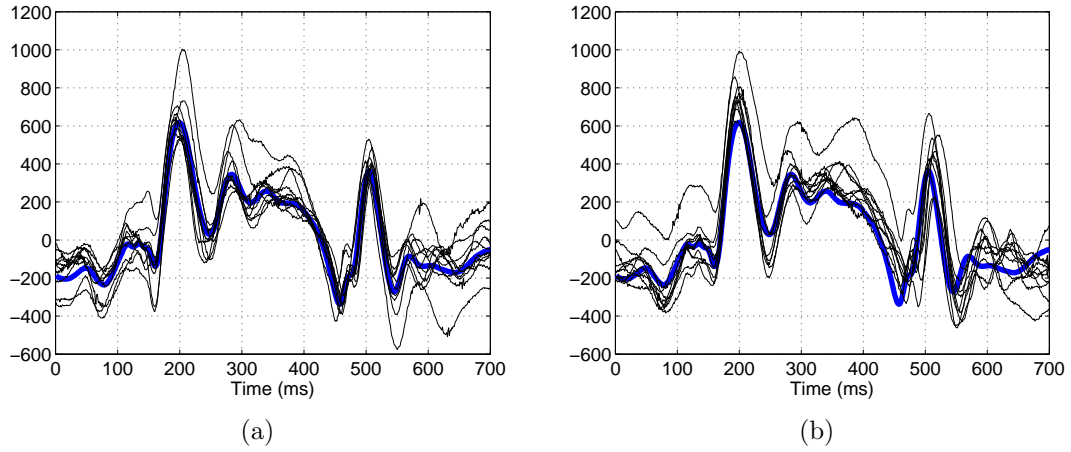


Figure 5.3: Means for the best performing individual across sessions for models (a)  $LDV_B - S_{1,1}$  and (b)  $LDV_B - S_{1,2}$  with several testing pulses.

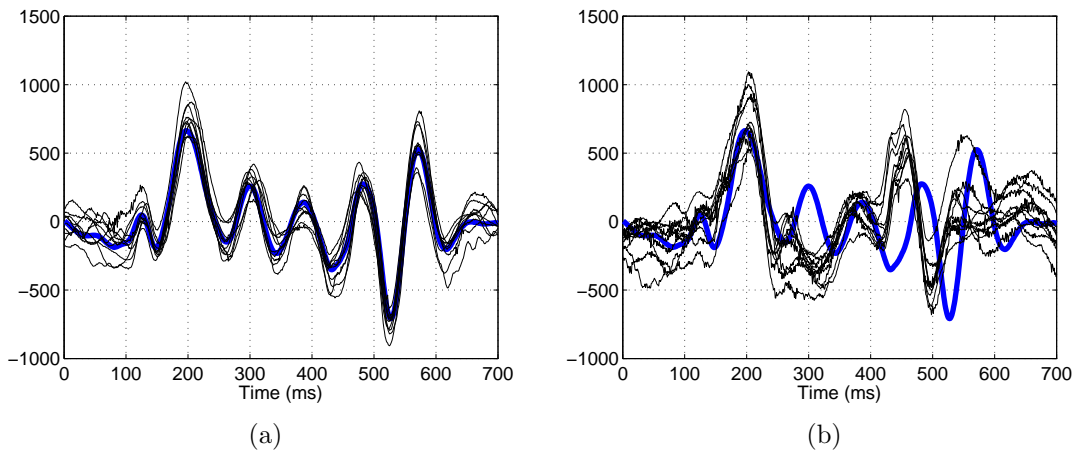


Figure 5.4: Means for the worst performing individual across sessions for models (a)  $LDV_B - S_{1,1}$  and (b)  $LDV_B - S_{1,2}$  with several testing pulses.



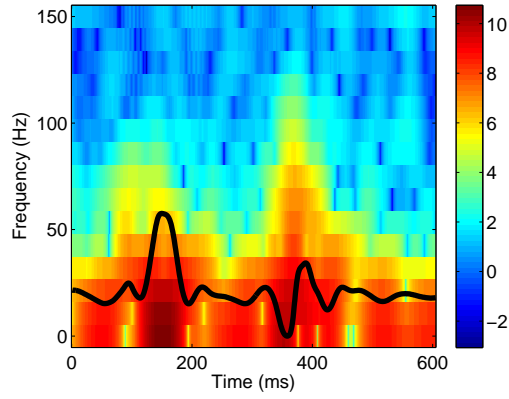
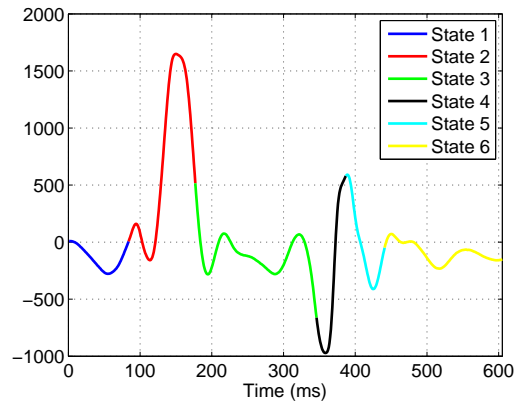


Figure 5.5: Mean spectrogram and pulse for an individual.



(a)

	1	2	3	4	5	6
1	0.987	0.013				
2		0.992	0.009			
3			0.993	0.007		
4				0.986	0.015	
5					0.985	0.015
6						1.000

(b)

Figure 5.6: The result of the max-product algorithm on a mean pulse is shown in (a), and the state transition probability matrix in shown in (b).

We can use this for detecting pulses in an LDV signal that has not been labeled. First, we need to modify the model to accommodate for the fact that it will not be run on a single pulse, but on a raw signal. This is done by adding several buffer states. We augment the state transition probability matrix to allow the model to transition from state 6 to the new states, and back to state 1. This entails changing  $p(6|6)$  from 1 to  $1 - \alpha$ ,  $p(6|7)$  to  $\alpha$ ,  $p(7|7)$  to  $1 - \alpha$ ,  $p(8|6)$  to  $\alpha$  and so on. Zero vectors are added for the new means, and identity vectors are added for the new variances. Each new state that is added guarantees that the model will spend at least another millisecond on each pulse. This can change the most likely state sequence along the entire path. The total number of states is determined adaptively by estimating the heart rate each iteration of the algorithm.

Then the magnitude STFT needs to be computed on the signal. Frequencies below 2 Hz are removed to remove baseline wander components of the signal. After this is done, the max-product algorithm computes the most likely state sequence for the signal given the model. Two sets of numbers are computed from the resulting state sequence. First, we find the time points where the model transitions from the last state back to state 1. This should indicate the start of a new pulse. Secondly, we compute the point that maximizes the signal within the region associated with state 2. This is approximately the location of the main peaks. However, since the models were individually trained, state 2 may not be the best place to look for the main peak. The algorithm runs as follows:

1. Start with the trained model  $f$ .
2. Add another state to the model.
3. Run the max-product algorithm on the data and save:

- (a) Transition times between pulses,
  - (b) Main peak locations.
4. Go to step 1 or go to step 4.
  5. Choose one model from the collection generated from steps 2 and 3.

The number of states to add to the original model may be chosen based on the reliability of the pulse detections. If the resulting interbeat interval sequence is implausible, then the corresponding model may be discarded. Two examples are shown in Figure 5.7. Data that are used in these examples are distinct from the data used to train the models, but are from the same session. The transitions are detected accurately, even for atypical signals. Thresholding methods may not work correctly in cases where the incisura is larger than the main peak. This algorithm, however, is able to recognize that the incisura and the main peak belong to the same pulse because of the state transitions in the model. The sequence of states across the whole signal is used to differentiate between the incisura and the main peak even though they have similar frequency content.

The main peaks are not always detected appropriately. This could be because state 2 was always used to find the main peak. Other methods could be used to find points of interest within the pulses once they are segmented.

A few pulses are required for training of the model that is used. This could be done manually or by another methods, such as a template matching algorithm. Then, the model is trained, and run on the remaining data. Heart rates may be computed from the detections. The advantage of this method over local methods which analyze the

pulses independently, is that the algorithm is optimized over the entire sequence of pulses to find the transition points.

## 5.4 Model $LDV_{BD}$

Model  $LDV_{BD}$  uses pulse model B and session model D with 4 states without any preprocessing. This model is designed to track state changes that occur from beat to beat. The choice of four states is motivated by prior knowledge. The subjects were at rest, and the primary source of beat to beat variability was respiration, for which we identified four epochs in the respiration phase: inhalation, end of inhalation, exhalation, and end of exhalation. In the next subsection, the number of states is varied. This model generally performs better than model  $LDV_B$  within session, but worse across sessions. The cause for this may be that the breathing patterns also change across sessions.

### 5.4.1 Interpretation of Model $LDV_{BD}$

A version of this work appeared in Kaplan, et al. [64]. To interpret the parameters from this model, another data set is used that includes a strain gauge for measuring respiration. LDV carotid pulse measurements were acquired from 43 subjects (22 female), ranging in age from 20 to 29 years, all non-smokers, with BMIs  $< 30$ , and free from cardiovascular, pulmonary or other major diseases. In this section, we present experimental results for two of these individuals for illustrative purposes. Data from all of the subjects are also analyzed and breathing rate estimation results are presented in Section 5.4.1.3. Models are trained for each subject and interpreted

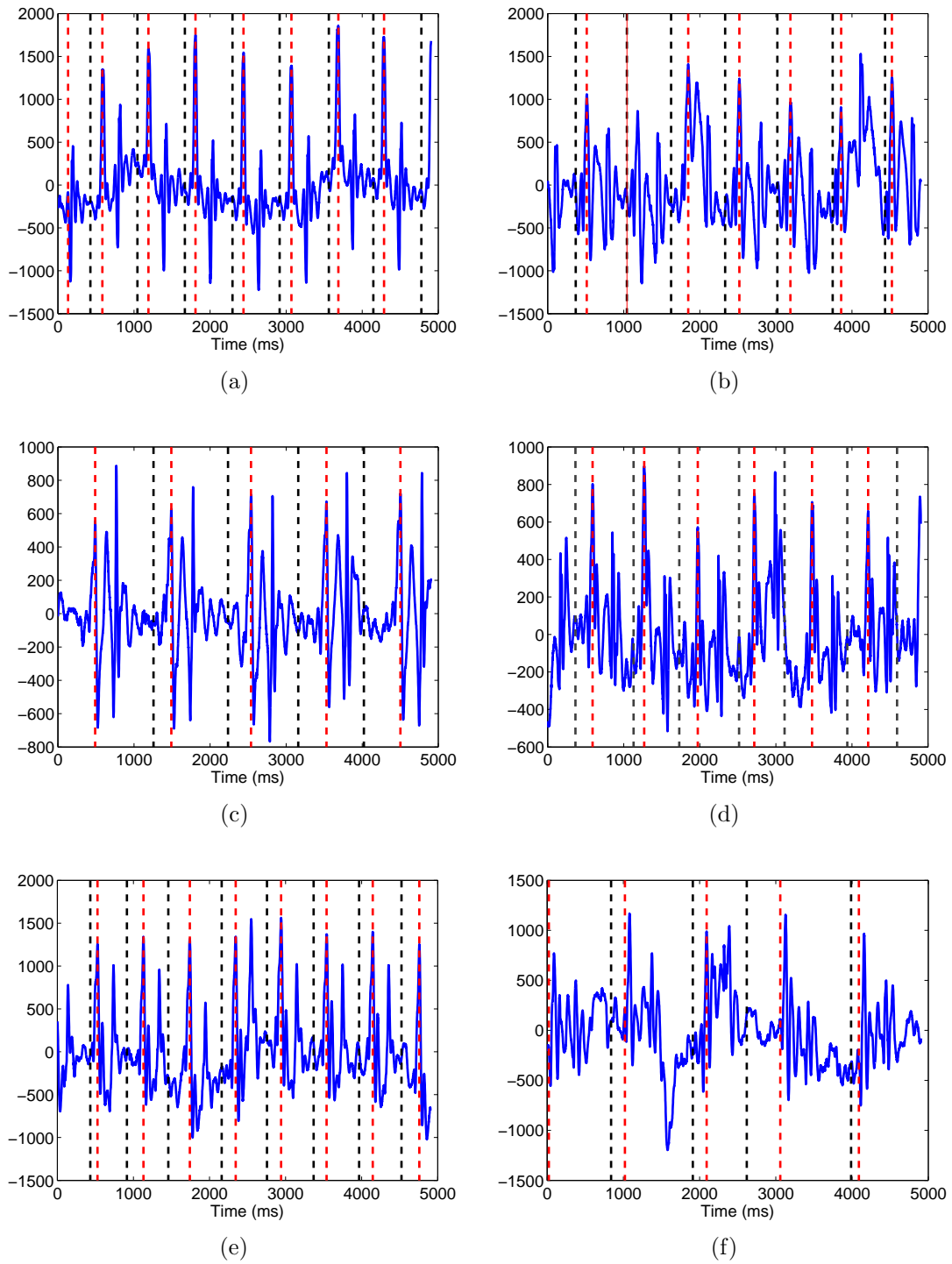


Figure 5.7: Examples of pulse segmentation using model  $LDV_C$  on 5 seconds of data. The black dotted lines are pulse transition between detections, and the red dotted lines are main peak detections. The estimated heart rates are: (a) 97 bpm, (b) 89 bpm, (c) 65 bpm, (d) 85 bpm, (e) 103 bpm, and (f) 57 bpm.

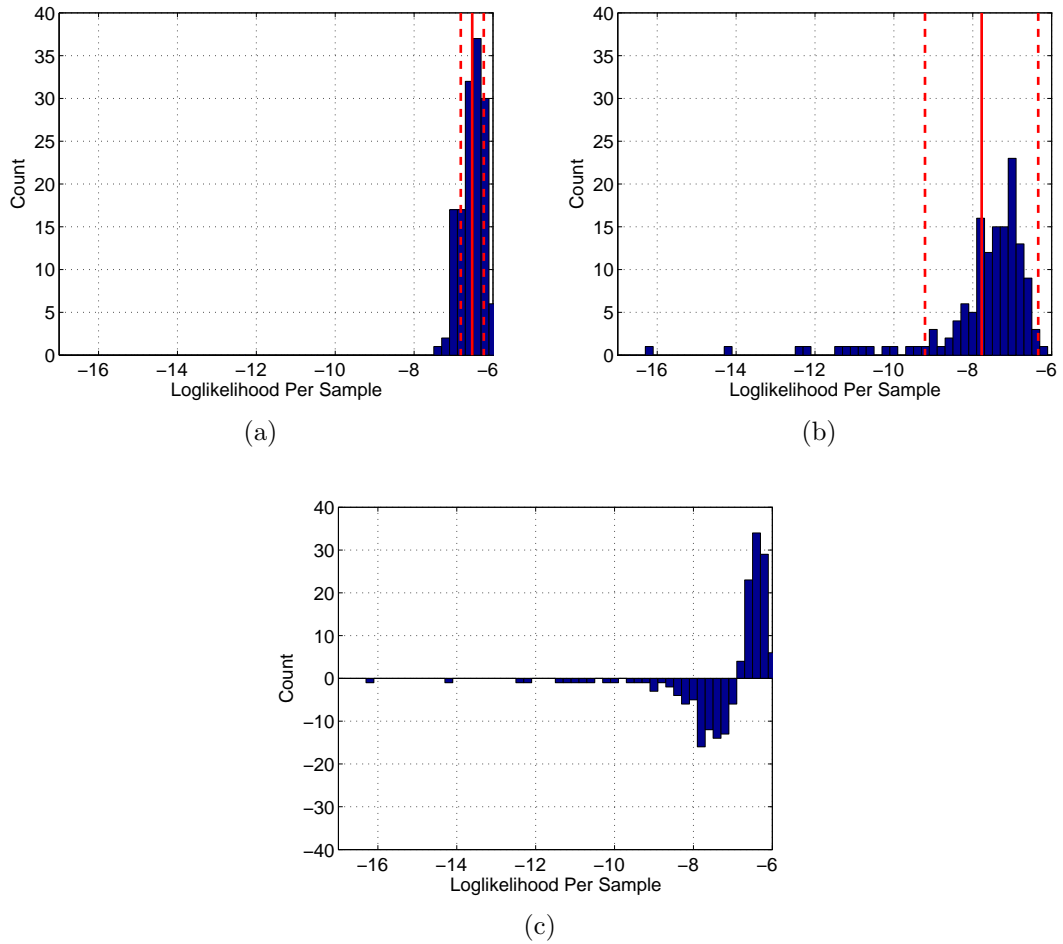


Figure 5.8: Histograms across individuals for (a) model  $LDV_{BD} - 1$ , and (b) model  $LDV_{BD} - 2$ . The solid red lines indicate the mean score and the dotted red line show a standard deviation away from the mean. The histogram in (c) shows how many more individuals for  $LDV_{BD} - 1$  there are than  $LDV_{BD} - 2$ .

with respect to the most likely state sequence. Also, respiration rate is estimated for each individual using the trained models, and compared to estimates derived from abdominal strain gauge recordings.

Carotid LDV pulse signals were measured using a Polytec PSV 400<sup>4</sup> LDV under resting conditions. The subjects were seated and asked to remain motionless and quiet for three minutes. The data under resting conditions were obtained as part of a larger experiment, which investigated the effects of a number of cardiorespiratory activating maneuvers as well as mental stressors, given in orders that were balanced over subjects. Conditions were separated by at least 4 minutes of recovery time, during which subjects viewed relaxing videos of aquatic life. An independent measure of the electrocardiogram (ECG was obtained from bilateral chest electrodes), and respiratory effort was measured with a strain gauge around the abdomen, using a Biopac Tel100 system and associated transducers. The LDV signal is sampled at 10 kHz, then downsampled to 1 kHz. To lessen the effects of measurement noise, harmonics with frequencies greater than 300 Hz are removed from the data by setting the higher frequency components in the discrete Fourier transform to zero, and taking the inverse transform. The simultaneous ECG recordings are used to extract 700 ms LDV pulses, where the first sample of each LDV pulse is aligned to occur at the same time as the peak of the QRS complex in the ECG signal. The R wave in the ECG signal was extracted using a simple thresholding and peak detection method.

The pulses from each individual are separated into two groups, the first containing 100 pulses, and the second consisting of 50 pulses. We train a set of ten models for each individual on the first group, with the number of states varying from 2 to 11. Parameter initializations were set to a uniform transition probability matrix, constant

---

<sup>4</sup>[www.polytec.com](http://www.polytec.com)

variance, and mean vectors taken from exemplar pulses spaced evenly in the pulse sequence. Optimal state sequences were computed over both groups of pulses for cross validation.

#### 5.4.1.1 Model parameters

The subjects were at rest, and the primary source of beat to beat variability may be respiration, for which we identified four epochs in the respiration phase: inhalation, end of inhalation, exhalation, and end of exhalation. The ideal number of states in the model is dependent on the pulse waveforms for the individual. A two state model may be sufficient to characterize the dynamics for some individuals, but more states may be needed for others. Although we instructed subjects to remain calm and motionless during recording, we recognize that there may be a number of sources of uncontrolled variability including anxiety as well as recovery from other activities during the laboratory session. For two individuals, we show three figures: the HMM mean vectors (Figure 5.9), the transition probability matrices (Figure 5.10), and the estimated state sequence compared to the strain gauge measurements (Figure 5.11).

As is evident in the figures, the HMM mean vectors indicate morphology changes due to the state dependence. Note that the greatest variability occurs around the incisura. Changes in LVET of 15 ms are present in these mean vectors, which is a significant change consistent with respiratory dynamics [65, 66]. Other studies examine the effect of respiration on heart rate, pulse transit time, and pre-ejection period [67, 68, 69]. This model allows for the analysis of respiration on waveforms. Amplitude variability in the main peaks is also observed, which may indicate beat to beat changes in blood pressure amplitude. The ability to measure such fine detail in the carotid pulse has



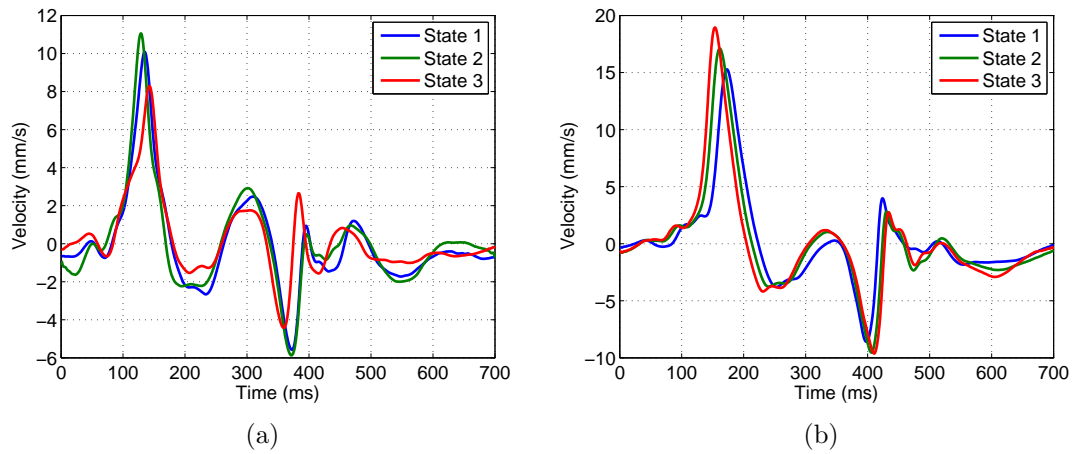


Figure 5.9: HMM mean vectors for two individuals: a) individual A, and b) individual B.

	1	2	3
1	0.00	0.93	0.07
2	0.02	0.60	0.38
3	0.38	0.18	0.44

(a)

	1	2	3
1	0.63	0.26	0.12
2	0.48	0.23	0.29
3	0.00	0.52	0.48

(b)

Figure 5.10: State transition probabilities for two individuals. a) State transition probability matrix for individual A. b) State transition probability matrix for individual B.

significant potential clinical use. Figure 5.10 shows the state transition matrices, whose entries are probabilities rounded off to the nearest hundredths place. These two individuals have dissimilar matrices, suggesting that the matrices are informative to the individual.

#### 5.4.1.2 State sequences

After the models are trained, the most likely state sequence is computed for each subject. For most subjects, we observed that the state sequences generally exhibit a nearly periodic pattern at a period roughly equal to typical respiration rates (0.2

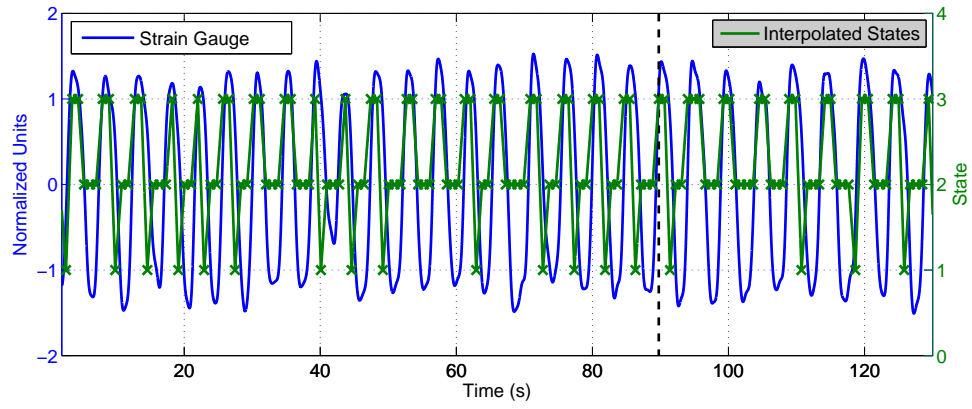
Hz). The state sequences were then compared to the strain gauge signals to further evaluate and quantify this relationship.

As mentioned above, the beat to beat dynamics during rest are primarily due to respiration effects. We first examine the optimal state path for an individual, and show that we are tracking changes due to respiration by comparison with measurements from the strain gauge. Using the trained HMM, the most likely state sequence,  $S_1^*, S_2^*, \dots, S_N^*$  is computed given the sequence of LDV pulses, where  $S_n^* \in \{1, 2, \dots, M\}$ . To visually compare with the strain gauge measurements, we construct an interpolated state signal, which is equal to the state number at time locations corresponding to the R wave peaks (marked in the figure by the X's) in the ECG signal, and intermediate values are interpolated linearly. Figure 5.11 shows both the strain gauge and the state interpolation for the two individuals. An upward gauge trace in the figure denotes inspiration as sensed in terms of abdominal expansion. Only the first 100 pulses (the time interval before the dotted vertical line) were used for model training. Data occurring after the dotted line were not used for training the models.

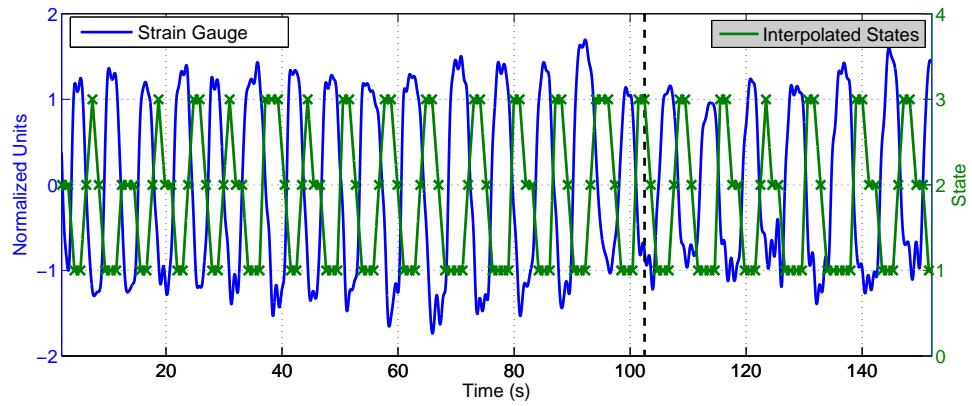
#### 5.4.1.3 Estimating respiration rate

Due to the agreement in periodicity between HMM state sequences and respiration cycles for many subjects at rest, it is of interest to quantify how well these models can be used for respiration rate estimation.

Respiration, which is affected by both voluntary and involuntary influences, is an integral part of the body's cardiovascular control system. In respiration-based studies, subjects are sometimes asked to breathe at experimentally controlled rates. An



(a)



(b)

Figure 5.11: Strain gauge measurements and optimal state paths for two individuals. Note that two vertical axes are used in these figures. Data occurring before the dotted vertical line were used for training. a) State path and strain gauge measurements for individual A. Data occurring before the dotted vertical line were used for training. b) State path and strain gauge measurements for individual B.

advantage to this procedure is that methods can be tested with careful control of respiration rate, providing that the subjects follow the breathing instructions accurately. In our experiments, the subjects are not instructed on how fast to breathe, so they are free to relax and do as they wish. The advantage here is the absence of the extra stimuli, which may induce additional states (make the subjects stressed, etc.).

Our emphasis here is on comparing an estimate of the respiration rate derived from the strain gauge with one derived from the hidden state models. The strain gauge is an indirect measurement of respiration, measuring the expansion and constriction of the abdomen. It is possible to breathe without observing the abdomen rise and fall significantly. Also, the abdomen can move and stretch voluntarily. These factors contribute to the uncertainty in the measurements. Still, the strain gauge performs quite well in many circumstances.

Of the 43 strain gauge measurements, 4 were not usable because of noise artifacts and they were not analyzed. We estimate the respiration rate from the strain gauge ( $r_{SG}$ ) and the interpolated state sequence ( $r_{SS}$ ) for each individual, and compare them on both the training and testing data.

**Respiration Rate from the Strain Gauge** First, the signal is filtered to remove high frequency noise. The cut-off frequency is individual dependent (around 0.5 Hz), and every case was verified manually to match in periodicity to the original signal. Then the local maxima are located by taking the first derivative and finding the zero crossings. The total number of full periods is divided by the time interval in seconds to give respiration cycles per second. Figure 5.12a shows an example of the processing steps for a sample individual.

**Respiration Rate from the LDV Derived State Sequence** First, the optimal state sequence is computed:  $\mathbf{S}^* = S_1^*, S_2^*, \dots, S_N^*$  using the Viterbi algorithm [38]. The next goal is to find repeating patterns in this sequence that may be periodic or semi-periodic with respiration. Shifted versions of this sequence are compared with the original sequence, and the level of disagreement between these two sequences is computed based on a distance measure between the states. The distance measure used between states  $i$  and  $j$  is a symmetrized divergence of the corresponding state distributions,

$$d_{i,j} = \frac{1}{2}d'_{i,j} + \frac{1}{2}d'_{j,i}, \quad (5.1)$$

where  $d'_{i,j}$  is the relative entropy between PDFs from states  $i$  and  $j$ , given by,

$$d'_{i,j} = \frac{1}{2} \sum_t \left( \frac{\sigma_{i,t}^2}{\sigma_{j,t}^2} + \frac{(\mu_{i,t} - \mu_{j,t})^2}{\sigma_{j,t}^2} - \ln \sigma_{i,t}^2 + \ln \sigma_{j,t}^2 - 1 \right).$$

Using this measure on shifted versions of  $\mathbf{S}^*$ , a shift dependent distance function is computed by,

$$D(\tau) = \frac{1}{T - \tau} \sum_{t=\tau+1}^T d_{S_t^*, S_{t-\tau}^*}. \quad (5.2)$$

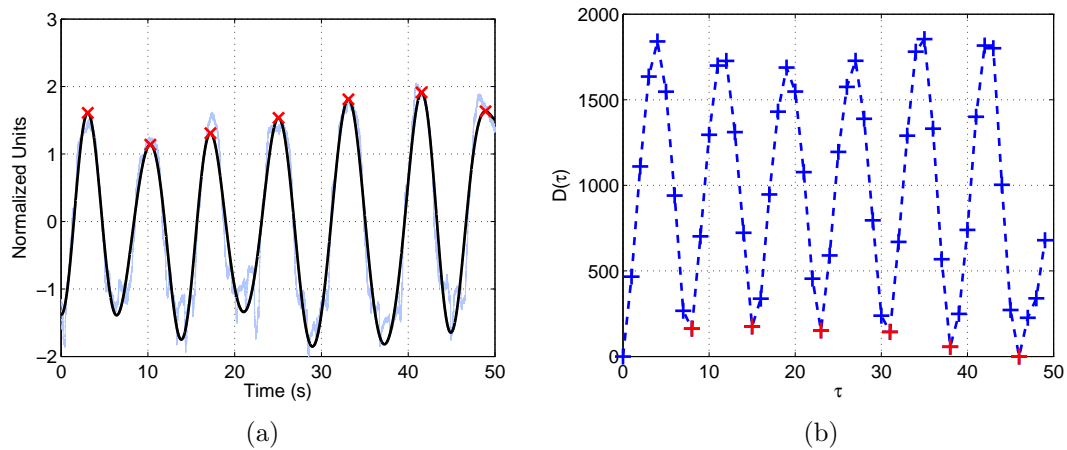
The shift  $\tau$  is in units of pulses (biological time). An example of this measure is shown in Figure 5.12b.

Two approaches for estimating respiration rate from this distance function are now described. If the underlying sequence is periodic with period  $Q$ , then so will the shift-distance function:  $D(\tau) = 0$  for  $\tau = \alpha Q$  for integer  $\alpha$ , since  $d_{i,i} = 0$ . If instead, the underlying sequence is only approximately periodic, then this function will admit a local minimum for  $\tau$  near  $\alpha Q$  for integer  $\alpha$ . The local minima of  $D(\tau)$ , therefore, represent time shifts for which the two sequences approximately match locally, and indicate periodicity in the sequence. In the first approach, the shift corresponding to

the first of these minima is selected to represent the periodicity of respiration. Using the ECG, the average respiration period is computed by multiplying this shift by the average interbeat interval.

The precision of this method is limited to integer values of the shift. To get subsample precision, we can instead use the discrete Fourier transform. In the second approach, a 1000 point DFT is computed on  $D(\tau)$  after subtracting the mean. Then the maximum of its magnitude is located, and the corresponding frequency ( $\text{beats}^{-1}$ ) is taken as the respiration frequency. The ECG derived mean IBI is again used to compute respiration rate in Hz. Figure 5.13 shows an example of this computation for the same individual shown in Figure 5.12.

**Performance Evaluation** The respiration rate is computed from the strain gauge,  $r_{SG}$ , and the HMM state sequence trained on LDV data,  $r_{SS}$ , on ten models with an increasing state space from 2 to 11. The error is computed as,  $\frac{r_{SG}-r_{SS}}{r_{SG}}$ , both on the 100 pulses used to train the HMMs, and on the following 50 pulses that were not used in training the HMMs. Figure 5.14 shows scatter plots of  $r_{SG}$  vs  $r_{SS}$  for the model with three states. Table 5.15 shows the results for five percentiles using the first method, and Table 5.16 shows results using the DFT method. The rows marked “Optimal” give the performance using the best performing number of states for each individual. The DFT method gives lower error than the local minimum method in the median, but has more outliers.



$\tau$																								
0	2	1	1	1	2	3	3	2	1	1	1	1	3	3	2	2	1	1	1	2	3	2	2	1
8	-	-	-	-	-	-	-	-	2	1	1	1	2	3	3	2	1	1	1	1	3	3	2	2
15	-	-	-	-	-	-	-	-	-	-	-	-	-	-	2	1	1	1	1	2	3	3	2	1

(c)

	S1	S2	S3
S1	0	679	3293
S2	679	0	689
S3	3293	689	0

(d)

Figure 5.12: Example of respiration rate estimation for one individual. In (a), the strain gauge is processed to derived  $r_{SG}$ . A total of 6 periods are detected and the rate during this interval is  $r_{SG} = 0.131$  Hz. Figure (b) shows the shift function  $D(\tau)$  for the same individual. The initial part of the state sequence is shown in (c) along with shifted versions of the sequence corresponding to the minima computed from  $D(\tau)$ . Figure (d) shows the state distances used. A shift of 8 pulses was detected and used with a mean IBI of 1.02 s, giving  $r_{SS} = 0.123$  Hz. The error for this individual is 6%, which is near the 50th percentile (median).

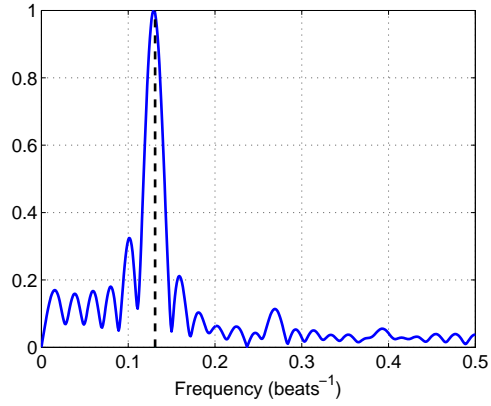


Figure 5.13: DFT of  $D(\tau)$  used in computing  $r_{SS}$ . A frequency of 0.13 is computed for this individual (same individual in Figure 5.12), giving the estimate  $r_{SS} = 0.128$  Hz.

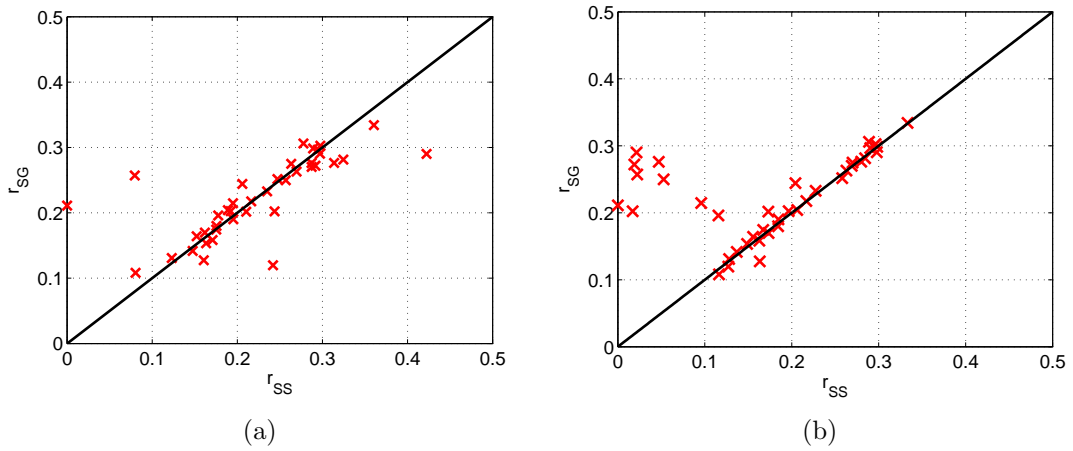


Figure 5.14: Scatter plot of  $r_{SG}$  vs  $r_{SS}$  for the three state model for (a) the local minimum method, and (b) the DFT method. The black line is the set of points for which  $r_{SG} = r_{SS}$ .



Number of States	10%	25%	50%	75%	90%
2	0.01	0.05	0.13	0.48	1.00
3	0.01	0.02	0.07	0.16	0.46
4	0.01	0.03	0.09	0.18	0.52
5	0.01	0.02	0.07	0.18	0.45
6	0.01	0.03	0.09	0.18	0.55
7	0.01	0.03	0.09	0.17	0.49
8	0.01	0.03	0.08	0.16	0.27
9	0.01	0.03	0.09	0.18	0.69
10	0.01	0.04	0.09	0.17	0.23
11	0.01	0.03	0.09	0.17	0.40
Optimal	0.01	0.02	0.05	0.09	0.17

(a)

Number of States	10%	25%	50%	75%	90%
2	0.02	0.04	0.08	0.59	1.00
3	0.01	0.03	0.06	0.13	0.38
4	0.01	0.03	0.07	0.09	0.49
5	0.02	0.03	0.07	0.12	0.41
6	0.01	0.03	0.07	0.09	0.36
7	0.01	0.03	0.07	0.10	0.22
8	0.02	0.03	0.06	0.09	0.36
9	0.01	0.03	0.07	0.13	0.67
10	0.01	0.03	0.06	0.09	0.16
11	0.01	0.03	0.07	0.11	0.24
Optimal	0.01	0.03	0.05	0.08	0.09

(b)

Figure 5.15: Respiration rate performance for the local minimum method. In (a), the algorithm is evaluated in the same 100 pulses used for training the HMMs. In (b), the following 50 pulses are used for estimating respiration rate.

Number of States	10%	25%	50%	75%	90%
2	0.01	0.06	0.14	0.47	1.00
3	0.01	0.02	0.06	0.14	0.27
4	0.01	0.03	0.09	0.18	0.52
5	0.01	0.02	0.07	0.19	0.45
6	0.01	0.03	0.09	0.18	0.55
7	0.01	0.03	0.09	0.18	0.51
8	0.01	0.03	0.09	0.18	0.30
9	0.01	0.03	0.09	0.17	0.67
10	0.01	0.04	0.09	0.17	0.24
11	0.01	0.03	0.09	0.18	0.44
Optimal	<0.01	0.01	0.03	0.17	0.89

(a)

Number of States	10%	25%	50%	75%	90%
2	0.01	0.03	0.11	0.90	1.00
3	<0.01	0.02	0.03	0.25	0.92
4	0.01	0.02	0.03	0.52	0.92
5	<0.01	0.01	0.02	0.52	0.92
6	0.01	0.01	0.03	0.26	0.92
7	0.01	0.02	0.03	0.16	0.91
8	0.01	0.01	0.03	0.26	0.91
9	0.01	0.01	0.03	0.38	0.92
10	<0.01	0.01	0.02	0.13	0.72
11	0.01	0.01	0.02	0.14	0.84
Optimal	<0.01	<0.01	0.01	0.05	0.15

(b)

Figure 5.16: Respiration rate performance for the DFT method. In (a), the algorithm is evaluated in the same 100 pulses used for training the HMMs. In (b), the following 50 pulses are used for estimating respiration rate.

#### 5.4.1.4 Discussion

We begin with the state sequences as illustrated in Figure 5.11, which shows that the state sequence generally tracks the record of respiration provided by the strain gauge. For individual A, states 1 and 2 typically corresponded to low lung volume, and state 3 often corresponded to maximal lung volume. For individual B, the situation was reversed: state 3 corresponded to low lung volume, and state 1 corresponded to maximal lung volume. Note that each heartbeat is associated with a time location by the corresponding R wave in the ECG signal, even though a 700 ms segment of the LDV data is used to estimate the model parameters. Also, since respiration phase is continuous, there are changes occurring in the signals during each LDV pulse. From the state sequences, we can see that state 1 is intermittent for individual A, while it occurs more consistently for individual B.

In the state means, we observe that the incisura changes location, indicating a change in the LVET. From Figure 5.9, the location of the inflection points near the incisura vary by 5 ms to 10 ms. In other studies, LVET has been shown to decrease during inspiration and increase during expiration [65]. A reduction of LVET during inspiration can be seen from the figures for both individuals.

Using Principal Components Analysis (PCA), we can further interpret the state means. Using the first two principal components computed from each data set, each pulse may be shown as a point in two dimensions. Figure 5.17 shows these results for the two individuals used in Figure 5.9. Each pulse is coded in terms of the associated state from the most likely state sequence. Even though the mean vectors may look similar in some cases, we can see that the states correspond to different clusters in the principal component space.

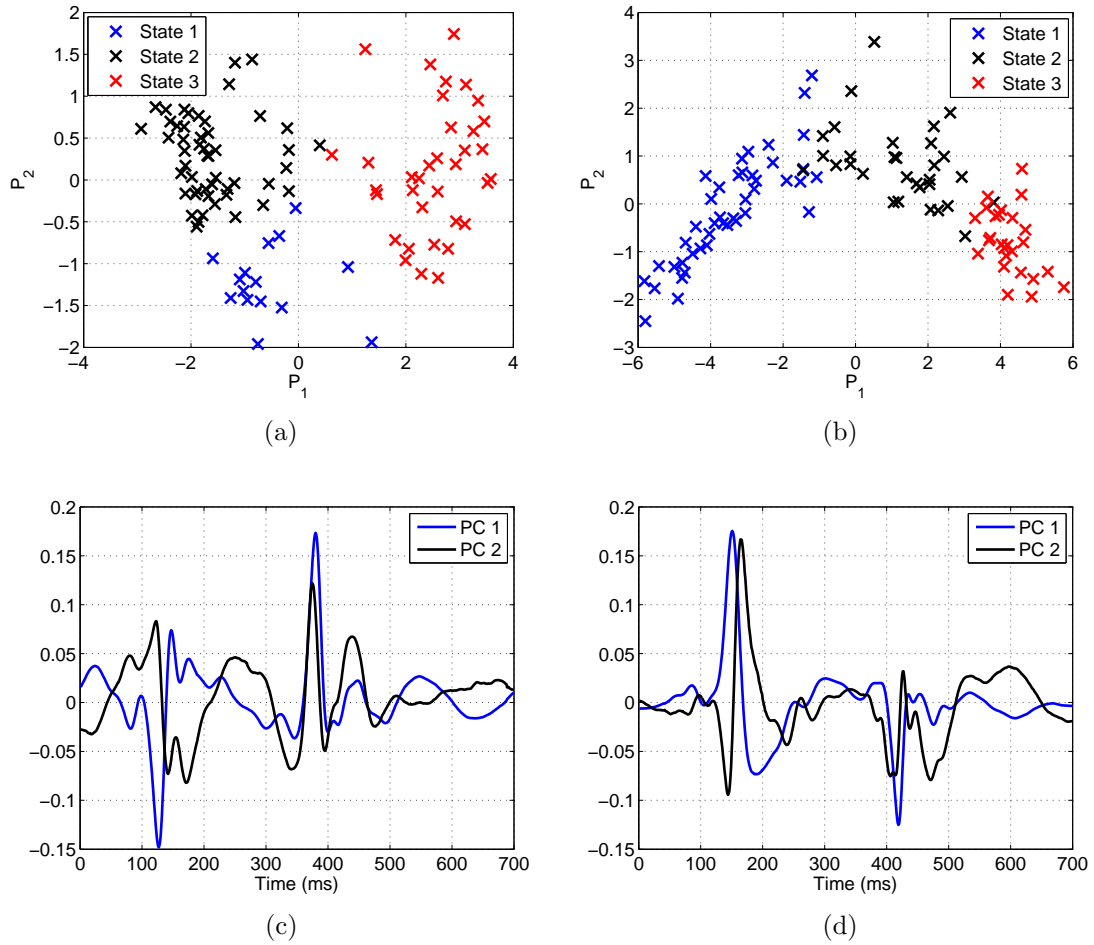


Figure 5.17: PCA analysis for two subjects. The axes for plots (a) and (b) correspond to different principle components, and each of the points represents one pulse. Figures (c) and (d) show the PCA basis vectors for (a) and (b), respectively.

The stationary distributions of the underlying Markov chains of the models give the limiting distributions across the states. They are the distributions  $p^*$  that satisfy,  $Ap^* = p^*$ , where  $A$  is the transpose of the transition probability matrix given in Figure 5.10. The stationary distributions for the two individuals are:  $p_A^* = \begin{bmatrix} 0.15 & 0.50 & 0.36 \end{bmatrix}$ ,  $p_B^* = \begin{bmatrix} 0.41 & 0.32 & 0.27 \end{bmatrix}$ . Thus we can see that for individual B, the states occur more or less uniformly, while state 2 is the most likely states for individual A. This is consistent with the preceding observations in the state sequences.

In some cases, the respiration rate error was large. This resulted from a state sequence that did not track the respiration cycle well. This can occur for a number of reasons. If the individuals in this study were performing some prescribed activity evoking a cardiovascular response, then the LDV pulse may be affected accordingly. Hidden states, such as the ones defined in this paper might be used to separate the various stimuli occurring in the body. If the number of states were increased, then perhaps some of them could correspond to respiration, while others could correspond to other physiological dynamics, such as mental stress. This could be a source of errors when attempting to infer respiration from the HMM state sequence.

We observed subjects whose state sequences did not match the strain gauge measure of respiration as well as the ones illustrated in the above figures. In some of the subjects, several of the states are only seen a few times, and the state sequence fluctuated between the other states in accordance with respiration. This indicates that there was a change observed in the data that only occurred a few times. The models can still be used to accurately estimate respiration rate for portions of the measurements in these cases. Subjects for which the respiration rate estimation fails entirely typically have one state which dominates for an extended period of time. This

we attribute to all of the states other than one corresponding to extraneous activity, and only one state corresponding to the resting condition.

# Chapter 6

## Wave Propagation in Elastic Tubes: Analysis and Models

This is a basic description of the physics involved in solving for the pressure distribution inside elastic tubes that are configured in a bifurcating tree structure. A concise background of the application of this physics to problems of blood flow may be found in the monograph by Westerhof [70]. Starting with the fluid dynamics of a finite element in cylindrical coordinates, and utilizing a number of simplifying assumptions, a solution for the pressure at every point in every elastic tube of a generic bifurcating tree structure (Figure 6.1) will be found. Applying Newton's second law of motion gives the Navier-Stokes equation of fluid dynamics. This, together with the equation of conservation of mass leads to a set of governing equations. After some simplifications, a wave equation and solution will be formulated for the situation of an infinite elastic tube. Then, reflections due to the interconnection of tubes (as in Figure 6.1) will be taken into account, and a solution of propagating waves with primary reflections is derived. Evidence of reflected pressure waves has been found in many studies [71, 72, 73]. The analysis in this chapter, and specifically Section 6.1 is based on the work of Zamir [57]. In the analysis of Wang, et al. [74], a model for the prediction

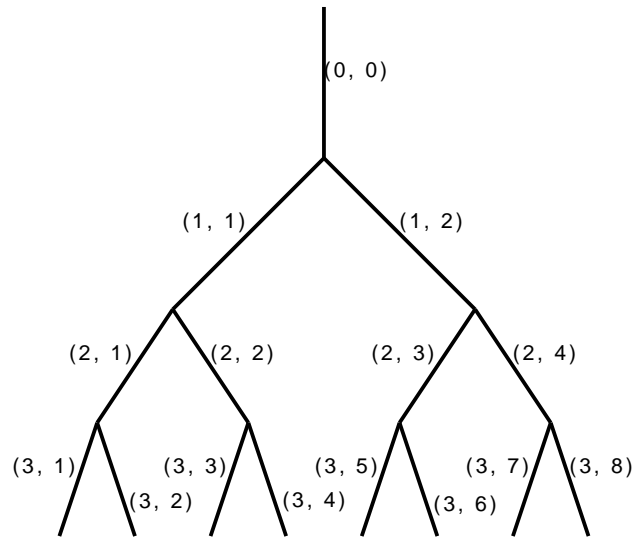


Figure 6.1: A generic bifurcating tree.

of pressure waves based on an extensive network of reflection sites is presented. The book by Nichols, et al. describes the physics of blood flow in light of the underlying physiology [75].

A novel model that is motivated by this analysis is then developed. Before using this model on LDV data, the relationship between the radius of an elastic tube and the underlying pressure of moving fluid is examined. This relationship is used to consider the use of the LDV as an indirect measurement of the underlying blood pressure in the carotid. The models are trained on LDV signals and interpreted.



## 6.1 Pressure Waves in Elastic Tubes

### 6.1.1 Conservation of Mass and the Navier-Stokes Equations

The governing equations of fluid dynamics are the conservation of mass equation and the Navier-Stokes equations. We use the cylindrical coordinates  $x$ ,  $r$ ,  $\theta$  for the axial, radial, and angular dimensions, respectively, and  $u$ ,  $v$ , and  $w$  for components of velocity in those respective dimensions. The conservation of mass equation is

$$\frac{\partial u}{\partial x} + \frac{\partial v}{\partial r} + \frac{\rho v}{r} + \frac{1}{r} \frac{\partial w}{\partial \theta} = 0. \quad (6.1)$$

The Navier-Stokes equations in cylindrical coordinates:

$$\rho \left( \frac{\partial u}{\partial t} + u \frac{\partial u}{\partial x} + v \frac{\partial u}{\partial r} + \frac{w}{r} \frac{\partial u}{\partial \theta} \right) + \frac{\partial p}{\partial x} = \mu \left( \frac{\partial^2 u}{\partial x^2} + \frac{\partial^2 u}{\partial r^2} + \frac{1}{r} \frac{\partial u}{\partial r} + \frac{1}{r^2} \frac{\partial^2 u}{\partial \theta^2} \right), \quad (6.2)$$

$$\rho \left( \frac{\partial v}{\partial t} + u \frac{\partial v}{\partial x} + v \frac{\partial v}{\partial r} + \frac{w}{r} \frac{\partial v}{\partial \theta} - \frac{w^2}{r} \right) + \frac{\partial p}{\partial r} = \mu \left( \frac{\partial^2 v}{\partial x^2} + \frac{\partial^2 v}{\partial r^2} + \frac{1}{r} \frac{\partial v}{\partial r} - \frac{v}{r^2} + \frac{1}{r^2} \frac{\partial^2 v}{\partial \theta^2} - \frac{2}{r^2} \frac{\partial w}{\partial \theta} \right), \quad (6.3)$$

$$\begin{aligned} & \rho \left( \frac{\partial w}{\partial t} + u \frac{\partial w}{\partial x} + v \frac{\partial w}{\partial r} + \frac{w}{r} \frac{\partial w}{\partial \theta} + \frac{vw}{r} \right) + \frac{1}{r} \frac{\partial p}{\partial \theta} = \\ & \mu \left( \frac{\partial^2 w}{\partial x^2} + \frac{\partial^2 w}{\partial r^2} + \frac{1}{r} \frac{\partial w}{\partial r} - \frac{w}{r^2} + \frac{1}{r^2} \frac{\partial^2 w}{\partial \theta^2} + \frac{2}{r^2} \frac{\partial v}{\partial \theta} \right). \end{aligned} \quad (6.4)$$

are derived by applying Newton's second law to a set of constitutive equations which relate the viscosity  $\mu$  to the pressure field  $p$ . A derivation of these equations can be found in Appendix A. These equations together with the equation of conservation of mass (Equation 6.1) provide the governing equations for the most general case of fluid flow in cylindrical coordinates.

## 6.1.2 Simplifications

A number of assumptions are made in order to simplify the model (equations 6.1, 6.2, 6.3, and 6.4). First, we assume symmetry around the angular dimension  $\theta$ ,

$$w = \frac{\partial w}{\partial \theta} = \frac{\partial v}{\partial \theta} = \frac{\partial u}{\partial \theta} = \frac{\partial p}{\partial \theta} = 0. \quad (6.5)$$

Applying this assumption eliminates Equation 6.4, and reduces the number of terms in the other equations,

$$\rho \left( \frac{\partial u}{\partial t} + u \frac{\partial u}{\partial x} + v \frac{\partial u}{\partial r} \right) + \frac{\partial p}{\partial x} = \mu \left( \frac{\partial^2 u}{\partial x^2} + \frac{\partial^2 u}{\partial r^2} + \frac{1}{r} \frac{\partial u}{\partial r} \right),$$

$$\rho \left( \frac{\partial v}{\partial t} + u \frac{\partial v}{\partial x} + v \frac{\partial v}{\partial r} \right) + \frac{\partial p}{\partial r} = \mu \left( \frac{\partial^2 v}{\partial x^2} + \frac{\partial^2 v}{\partial r^2} + \frac{1}{r} \frac{\partial v}{\partial r} - \frac{v}{r^2} \right),$$

$$\frac{\partial u}{\partial x} + \frac{\partial v}{\partial r} + \frac{\rho v}{r} = 0.$$

The next assumptions are long-wave and fast-wave assumptions, which are defined by,

$$u \frac{\partial u}{\partial x}, v \frac{\partial u}{\partial r} \ll \frac{\partial u}{\partial t}, \quad (6.6)$$

$$u \frac{\partial v}{\partial x}, v \frac{\partial v}{\partial r} \ll \frac{\partial v}{\partial t}, \quad (6.7)$$

$$\frac{\partial^2 u}{\partial x^2} \ll \frac{\partial^2 u}{\partial r^2}, \quad (6.8)$$

$$\frac{\partial^2 v}{\partial x^2} \ll \frac{\partial^2 v}{\partial r^2}. \quad (6.9)$$

Applying these assumptions gives,

$$\rho \frac{\partial u}{\partial t} + \frac{\partial p}{\partial x} = \mu \left( \frac{\partial^2 u}{\partial r^2} + \frac{1}{r} \frac{\partial u}{\partial r} \right), \quad (6.10)$$

$$\rho \frac{\partial v}{\partial t} + \frac{\partial p}{\partial r} = \mu \left( \frac{\partial^2 v}{\partial r^2} + \frac{1}{r} \frac{\partial v}{\partial r} - \frac{v}{r^2} \right), \quad (6.11)$$

$$\frac{\partial u}{\partial x} + \frac{\partial v}{\partial r} + \frac{\rho v}{r} = 0. \quad (6.12)$$

In these equations, the pressure is a function of axial direction, radial direction, and time:  $p = p(x, r, t)$ ; and each component of velocity ( $u, v$ ) is also a function of axial direction, radial direction, and time:  $u = u(x, r, t)$ ,  $v = v(x, r, t)$ . The angular component of velocity,  $w$ , is not present because of the symmetry assumption.

### 6.1.3 One Dimensional Wave Equation

It is desired to have a model for the fluid flow expressed as a one dimensional wave equation. First, pressure and velocity are averaged along the radial dimension. Multiplying both sides of equations 6.10 and 6.12 by  $2\pi r$  and integrating from  $r = 0$  to  $r = a$ ,

$$2\pi\rho \int_0^a r \frac{\partial u}{\partial t} dr + 2\pi \int_0^a r \frac{\partial p}{\partial x} dr = 2\pi\mu \int_0^a r \left( \frac{\partial^2 u}{\partial r^2} + \frac{1}{r} \frac{\partial u}{\partial r} \right) dr,$$

$$2\pi \int_0^a r \frac{\partial u}{\partial x} dr + 2\pi \int_0^a r \left( \frac{\partial v}{\partial r} + \frac{v}{r} \right) dr = 0.$$

The radius of the tube is  $a$ , which is a function of time:  $a = a(t)$ . Equation 6.11 is no longer needed, since the radial dimension has been averaged out. The boundary condition is:  $v(x = a, t) = \frac{\partial a}{\partial t}$ . The flow rate ( $q$ ), wall shear stress ( $\tau_w$ ), and cross

sectional area ( $A$ ) are defined as,

$$q = 2\pi \int_0^a r u dr,$$

$$\tau_w = -\mu \left[ \frac{\partial u}{\partial r} \right]_{r=a},$$

$$A = \pi a^2.$$

The governing equations can now be written as,

$$\frac{\partial q}{\partial t} + \frac{A}{\rho} \frac{\partial p}{\partial x} = \frac{-2\pi a}{\rho} \tau_w,$$

$$\frac{\partial q}{\partial x} + \frac{\partial A}{\partial t} = 0.$$

Applying the inviscid flow assumption:  $\tau_w = 0$ ,

$$\frac{\partial q}{\partial t} + \frac{A}{\rho} \frac{\partial p}{\partial x} = 0, \tag{6.13}$$

$$\frac{\partial q}{\partial x} + \gamma \frac{\partial p}{\partial t} = 0, \tag{6.14}$$

where  $\gamma = \frac{\partial A}{\partial p}$ . Cross differentiating results in,

$$\frac{\partial^2 p}{\partial t^2} = \frac{A}{\rho \gamma} \frac{\partial^2 p}{\partial x^2}, \tag{6.15}$$

$$\frac{\partial^2 q}{\partial t^2} = \frac{A}{\rho \gamma} \frac{\partial^2 q}{\partial x^2}. \tag{6.16}$$

The solution of these equation for a single harmonic with amplitude  $p_o$  and frequency  $w$  is,

$$p(x, t) = p_o e^{j\omega\left(t - \frac{x}{c_o}\right)}, \quad (6.17)$$

$$q(x, t) = \frac{Ap_o}{\rho c_o} e^{j\omega\left(t - \frac{x}{c_o}\right)}, \quad (6.18)$$

where  $c_o^2 = \frac{A}{\rho} \frac{\partial p}{\partial A}$  is the wave speed.

These solutions can be readily verified by substituting back into equations 6.13 and 6.14. The initial pressure is  $p_o = p(x = 0, t = 0)$ , and is complex in general.

#### 6.1.4 Primary Reflection

If there is a reflection at the end of the tube, the pressure and flow are a sum of a forward moving wave ( $p_f(x, t) = p_o e^{j\omega\left(t - \frac{x}{c_o}\right)}$ ), and the reflected, backward moving wave ( $p_b(x, t) = Bp_o e^{j\omega\left(t + \frac{x}{c_o}\right)}$ ). The amplitude of the reflected wave can be expressed in terms of a reflection coefficient,  $R = \frac{p_b(x=l, t)}{p_f(x=l, t)}$ , where  $l$  is the length of the tube.

Thus,

$$p_b(x = l, t) = Rp_f(x = l, t) = Rp_o e^{j\omega\left(t - \frac{x}{c_o}\right)}.$$

Solving for the amplitude of the reflected wave,

$$Bp_o = Rp_o e^{-j2\omega \frac{l}{c_o}}.$$

Thus, the reflected wave is,

$$p_b(x, t) = Rp_o e^{j\omega\left(t + \frac{x}{c_o} - \frac{2l}{c_o}\right)}.$$

After a similar analysis for the flow rate, the solution to the wave equations 6.13 and 6.14 with the primary reflection is,

$$p(x, t) = p_f(x, t) + p_b(x, t) = p_o \left( e^{-j\omega \frac{x}{c_o}} + R e^{j\omega \frac{x-2l}{c_o}} \right) e^{j\omega t}, \quad (6.19)$$

$$q(x, t) = q_f(x, t) + q_b(x, t) = \frac{A p_o}{\rho c_o} \left( e^{-j\omega \frac{x}{c_o}} + R e^{j\omega \frac{x-2l}{c_o}} \right) e^{j\omega t}. \quad (6.20)$$

Equations 6.19 and 6.20 can be verified to be a solution of 6.13 and 6.14 by substitution.

### 6.1.5 Pressure in a Tree Structure

In a general tree structure (Figure 6.1), the goal is to find the pressure as a function of axial position and time in every tube of the structure. Equation 6.19 gives this pressure; however, it is necessary to compute the complex valued  $p_o$  for each tube. Using a subscript notation  $a, b$  to designate a particular tube, as shown in Figure 6.1, the notation  $\gamma_{a,b} = p_{o_{a,b}}$  is adopted. Using Equation 6.19, the pressure at the end of any tube, and the pressure at the entry of the next tube is,

$$p(x = 0_{a,b}, t) = \gamma_{a,b} \left( 1 + R_{a,b} e^{-j\omega \frac{2l_{a,b}}{c_{a,b}}} \right) e^{j\omega t},$$

$$p(x = l_{a-1,n}, t) = \gamma_{a-1,n} \left( e^{-j\omega \frac{l_{a-1,n}}{c_{a-1,n}}} + R_{a-1,n} e^{-j\omega \frac{l_{a-1,n}}{c_{a-1,n}}} \right) e^{j\omega t}.$$

The length, reflection coefficient, and wave speed of the tube  $j, k$  are  $l_{j,k}$ ,  $R_{j,k}$ , and  $c_{j,k}$  respectively. The index  $n$  is given by  $n = \begin{cases} \frac{b}{2} & , b \text{ even} \\ \frac{b+1}{2} & , b \text{ odd} \end{cases}$ , which is apparent

when examining Figure 6.1. Setting  $p(x = 0_{a,b}, t) = p(x = l_{a-1,n}, t)$ ,

$$\gamma_{a,b} \left( 1 + R_{a,b} e^{-j\omega \frac{2l_{a,b}}{c_{a,b}}} \right) = \gamma_{a-1,n} (1 + R_{a-1,n}) e^{-j\omega \frac{l_{a-1,n}}{c_{a-1,n}}}.$$

Solving for  $\gamma_{a,b}$ ,

$$\gamma_{a,b} = \gamma_{a-1,n} \frac{(1 + R_{a-1,n}) e^{-j\omega \frac{l_{a-1,n}}{c_{a-1,n}}}}{1 + R_{a,b} e^{-j\omega \frac{2l_{a,b}}{c_{a,b}}}}. \quad (6.21)$$

Equation 6.21 provides a means of computing  $\gamma_{a,b}$  for every tube in the tree, given the reflection coefficients of each tube, starting from the top of the tree and moving down the tree. The initial value  $\gamma_{0,0}$  must be known.

## 6.2 Models

In the analysis given above, the pressure at any point in the structure of bifurcating tubes is the superposition of an incident pressure wave, and a number of reflected waves. In order for this relationship to hold, the following assumptions were made about the fluid flow:

1. The vessel is symmetric about the angular dimension- this eliminates the angular dimension (Equation 6.5).
2. Long wave and fast wave assumptions (Equations 6.6-6.9).
3. Pressure and velocity are averaged along the radial dimension.
4. The flow is inviscid.

This analysis motivates a computable model that expresses the pressure as a linear combination of scaled and shifted wave functions. The wave function itself, along with the time shifts and amplitudes may be estimated from training data.

### 6.2.1 Model Description

We seek a model for a pressure waveform,  $p(t)$  recorded at a site  $x = x_0$ , assuming that there are a number of reflections at other points in the system. The wave equations derived in the previous section imply that there is an initial waveform that is reflected at each of the reflection sites, with some possibly frequency dependent coefficient. Thus, a copy of this waveform is filtered and then propagates back towards the measurement site. This motivates a model for the pressure where  $p(t)$  is a summation of scaled and shifted versions of some input waveform  $s(t)$ ,

$$p(t) \approx \sum_{i=1}^I a_i s(t - \tau_i). \quad (6.22)$$

The time shifts and amplitudes may be collectively written,

$$\mathbf{a} = (a_1, a_2, \dots, a_I), \quad (6.23)$$

$$\boldsymbol{\tau} = (\tau_1, \tau_2, \dots, \tau_I), \quad (6.24)$$

$$\mathbf{s} = (s(1), s(2), \dots, s(T)), \quad (6.25)$$

where  $T$  is the length of the waveform. This assumes that the reflection coefficients are frequency independent. Putting this in the form of a noise model, we write each waveform copy as,

$$p_i(t) = a_i s(t - \tau_i) + \omega_i(t), \quad (6.26)$$



where  $\omega_i(t) \sim \mathcal{N}(0, \sigma_i^2)$ . Then the whole pressure signal is,

$$p(t) = \sum_{i=1}^I p_i(t) + \omega_0(t), \quad (6.27)$$

with  $\omega_0(t) \sim \mathcal{N}(0, \sigma_0^2)$ .

This model can be viewed in terms of a Linear Time-Invariant (LTI) system with the input being the initial pressure wave, and the output is the pressure measured at any point along the arterial tree. The impulse response of this system is,

$$h[t] = \delta[t - \tau_0] + \sum_{i=1}^I a_i \delta[n - \tau_i], \quad (6.28)$$

where  $\tau_0$  is the time that the input wave takes to reach the measurement site,  $a_i$  is the reflection coefficient for the  $i^{\text{th}}$  reflection, and  $\tau_i$  is the time that the reflected wave takes to arrive at the measurement site. The frequency response, computed by taking the Fourier transform of  $h[t]$ , becomes,

$$H(e^{j\omega}) = e^{-j\omega\tau_0} + \sum_{i=1}^I a_i e^{-j\omega\tau_i}. \quad (6.29)$$

## 6.2.2 Estimation of Parameters

This model formulation suggests an Expectation Maximization algorithm, where  $p_i(t)$  are the complete data, and  $p(t)$  are the incomplete, or observed data. The loglikelihood of the complete data is

$$\ln f(p_1(t), p_2(t), \dots, p_I(t)) = \sum_{i=1}^I \sum_{t=1}^T \left( -\frac{1}{2} \ln 2\pi\sigma_i^2(t) - \frac{1}{2\sigma_i^2} (p_i(t) - a_i s(t - \tau_i))^2 \right). \quad (6.30)$$

In computing parameter estimates, we proceed by computing the expected value of the loglikelihood of the incomplete data given the complete data,

$$E [\ln f (p_1 (t), p_2 (t), \dots, p_I (t)) | p (t)] = \quad (6.31)$$

$$= E \left[ \sum_{i=1}^I \sum_{t=1}^T \left( -\frac{1}{2} \ln 2\pi\sigma_i^2 - \frac{1}{2\sigma_i^2} (p_i (t) - a_i s (t - \tau_i))^2 \right) | p (t) \right] \quad (6.32)$$

$$= \sum_{i=1}^I \sum_{t=1}^T \left( -\frac{1}{2} \ln 2\pi\sigma_i^2 (t) - \frac{1}{2\sigma_i^2} (E [p_i^2 (t) | p (t)]) \right) \quad (6.33)$$

$$- 2a_i s (t - \tau_i) E [p_i (t) | p (t)] + a_i^2 s^2 (t - \tau_i) \Big). \quad (6.34)$$

We can remove terms that do not involve the parameters to form the following objective function,

$$Q (\mathbf{a}, \boldsymbol{\tau}, \mathbf{s}) = \sum_{i=1}^I \sum_{t=1}^T \left( \frac{1}{\sigma_i^2} a_i s (t - \tau_i) E [p_i (t) | p (t)] - \frac{1}{2\sigma_i^2} a_i^2 s^2 (t - \tau_i) \right). \quad (6.35)$$

The derivatives are

$$\frac{\partial Q}{\partial a_i} = \frac{1}{\sigma_i^2} \sum_{t=1}^T s (t - \tau_i) E [p_i (t) | p (t)] - a_i s^2 (t - \tau_i), \quad (6.36)$$

$$\frac{\partial Q}{\partial \tau_i} = \frac{1}{\sigma_i^2} \sum_{t=1}^T a_i s (t - \tau_i) \frac{\partial s (t - \tau_i)}{\partial t} E [p_i (t) | p (t)] - a_i^2 s (t - \tau_i) \frac{\partial s (t - \tau_i)}{\partial t},$$

$$\frac{\partial Q}{\partial s (t)} = \sum_{i=1}^I \left( \frac{1}{\sigma_i^2} a_i E [p_i (t - \tau_i) | p (t)] - \frac{1}{\sigma_i^2} a_i s (t) \right). \quad (6.37)$$

Setting the above equations to zero, and solving for the parameters, we obtain the parameter updates,

$$\hat{a}_i = \frac{\sum_{t=1}^T \hat{s}(t - \hat{\tau}_i) E[p_i(t) | p(t)]}{\sum_{t=1}^T \hat{s}^2(t - \hat{\tau}_i)}, \quad (6.38)$$

$$\hat{s}(t) = \frac{\sum_{i=1}^I \frac{\hat{a}_i}{\sigma_i^2} E[p_i(t - \hat{\tau}_i) | p(t)]}{\sum_{i=1}^I \frac{\hat{a}_i}{\sigma_i^2}}. \quad (6.39)$$

The time shift estimate satisfies,

$$\sum_{t=1}^T \hat{a}_i \hat{s}(t - \hat{\tau}_i) \frac{\partial \hat{s}(t - \hat{\tau}_i)}{\partial t} E[p_i(t) | p(t)] - \hat{a}_i^2 \hat{s}(t - \hat{\tau}_i) \frac{\partial \hat{s}(t - \hat{\tau}_i)}{\partial t} = 0. \quad (6.40)$$

The conditional expectation  $E[p_i(t) | p(t)]$  is a function of the parameters,  $(\mathbf{a}_i, \tau_i, \mathbf{s})$ , and may be computed by,

$$E[p_i(t) | p(t)] = E[p_i(t)] + \frac{\sigma_i^2}{\sigma_0^2 + \sum_{i=1}^I \sigma_i^2} (p_i(t) - E[p_i(t)]), \quad (6.41)$$

$$= a_i s(t - \tau_i) + \frac{\sigma_i^2}{\sigma_0^2 + \sum_{i=1}^I \sigma_i^2} (p_i(t) - a_i s(t - \tau_i)). \quad (6.42)$$

For notational convenience, we define the function  $h((\mathbf{a}, \boldsymbol{\tau}, \mathbf{s})) \triangleq E[p_i(t) | p(t)]$ . The resulting estimation algorithm begins with an initialization and the parameters are updated during each iteration:

1. Initialize the parameters:  $\mathbf{a}^{(0)}, \hat{\boldsymbol{\tau}}^{(0)}, \hat{\mathbf{s}}^{(0)}$ .
2. E-Step: Compute  $h\left(\left(\hat{\mathbf{a}}^{(k)}, \hat{\boldsymbol{\tau}}^{(k)}, \hat{\mathbf{s}}^{(k)}\right)\right)$  using Equation 6.42. Set  $k \rightarrow k + 1$ .
3. M-Step: Compute one or more of the following,
  - (a) Compute parameter updates for  $\hat{\mathbf{a}}^{(k)}$  using Equation 6.38.

(b) Compute parameter updates for  $\hat{\boldsymbol{\tau}}^{(k)}$  by performing a linear search to find close solutions to Equation 6.40.

(c) Compute parameter updates for  $\hat{\boldsymbol{s}}^{(k)}$  using Equation 6.39.

4. Check for convergence. Go to step 2.

In the parameter updates for step 3, any of the three parameters may be computed. Updates for  $\hat{\boldsymbol{a}}^{(k)}$  and  $\hat{\boldsymbol{\tau}}^{(k)}$  may be computed simultaneously over several iterations. Once these parameters converge, several iterations are performed updating  $\hat{\boldsymbol{s}}^{(k)}$ , and so on.

### 6.3 Application to LDV

To apply the physics of fluid flow in elastic tubes from the previous chapter to the LDV signal, we need to make a connection between the underlying blood pressure and the LDV signal. From the resulting physics, the relationship between the tube radius and the pressure is logarithmic. This has been validated experimentally [76, 77]. A linear approximation is valid under small changes of the radius. The displacement of the skin surface as measured by the LDV is related to the changing radius of the carotid, but the nature of this relationship is largely unknown. This relationship depends on the material nature of the tissue that lies in between the carotid and the skin. The close proximity of the vessel to the skin, however, is motivation for constructing a model that uses the physics outlined in this chapter.

### 6.3.1 Pressure-Radius Relationship

We can approximate the pressure-radius relationship from the wave equation derived in the previous chapter. The square of the wave speed in a given segment is,

$$c^2 = \frac{A}{\rho} \frac{\partial p}{\partial A}. \quad (6.43)$$

Thus, the pressure as a function of the cross sectional area and the radius  $r$  is logarithmic,

$$p = c^2 \rho \ln A + z, \quad (6.44)$$

$$= c^2 \rho \ln \pi + 2c^2 \rho \ln r + z. \quad (6.45)$$

This can be approximated by a linear function around a nominal radius  $r_0$  as,

$$\hat{p} = \frac{2c^2 \rho}{r_0} (r - r_0) + c^2 \rho \ln \pi + 2c^2 \rho \ln r_0 + z. \quad (6.46)$$

The error as a function of  $r$  is,

$$p - \hat{p} = 2c^2 \rho \left( \ln \frac{r}{r_0} - \frac{r - r_0}{r_0} \right). \quad (6.47)$$

Typical values for the wave speed and density are:

$$c \approx 5 \text{ m/s}, \quad (6.48)$$

$$\rho \approx 1060 \text{ kg/m}^3. \quad (6.49)$$

Under the range of 80 mmHg to 120 mmHg for systolic and diastolic pressure, using Equation 6.45, the radius ranges from 2.7 mm to 3.0 mm. Figure 6.2 shows this error

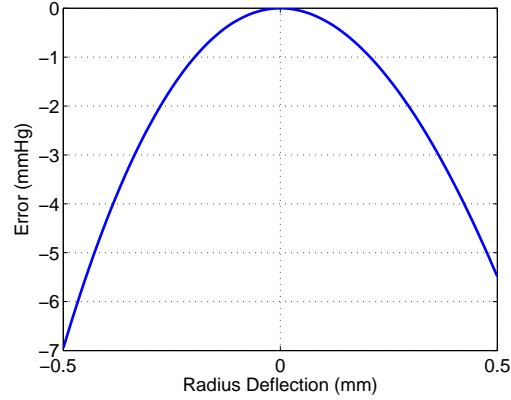


Figure 6.2: Linear approximation error as a function of radius change from 2.85 mm.

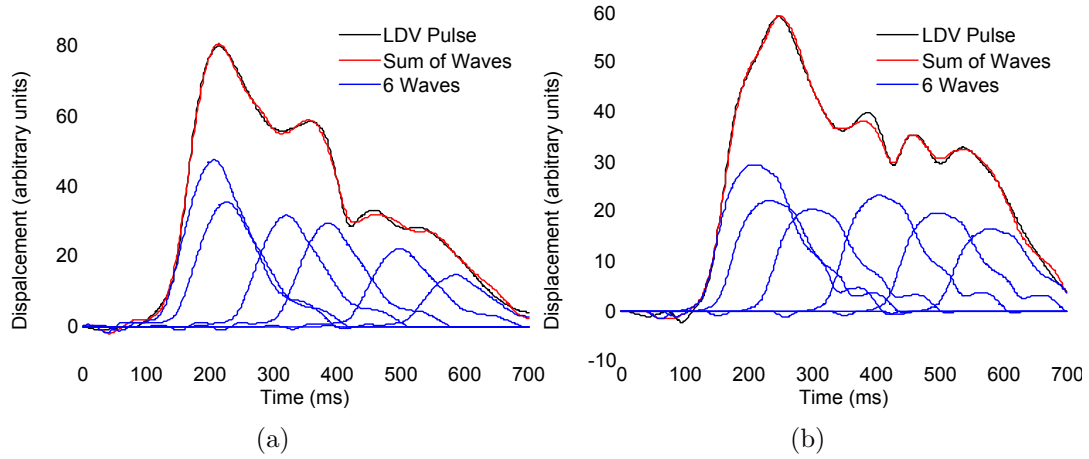


Figure 6.3: Model results for two subjects.

as a function of radius change from a nominal value of 2.85 mm. We can see that the linear approximation is an overestimate.

The model described in Section 6.2.1 was applied to the LDV data with six copies of the wave function. Amplitudes were set to a constant value, and time shifts were evenly distributed. Gaussian functions were used to initialize the wave function. Figure 6.3 shows the results of applying this model to two subjects.

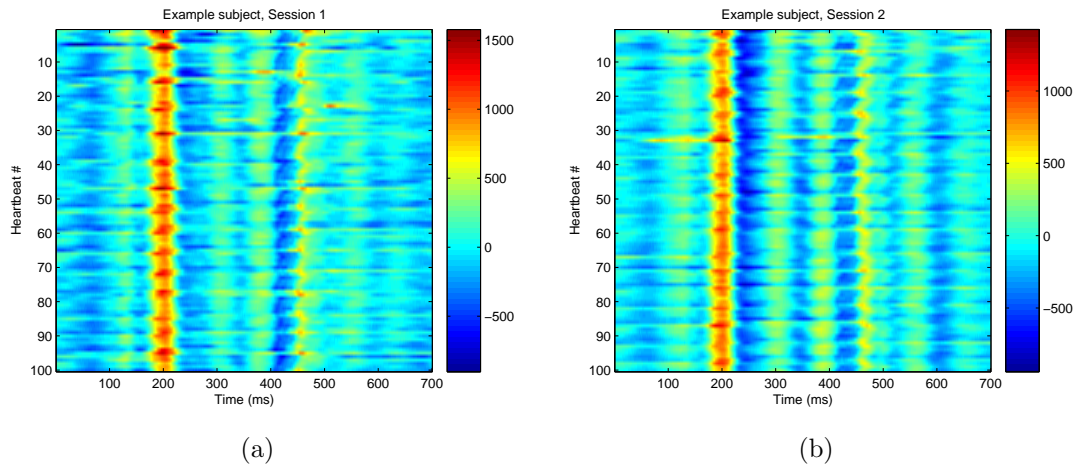


Figure 6.4: Data images for an individual across two sessions.

### 6.3.2 State Effects

One important aspect of the LDV heartbeats is that they are dependent on certain factors which may or may be directly measured in the signal. This is readily observed in the data. A major source of these confounding factors is thought to be the effects on blood pressure due to breathing. In this section, we discuss how the state (breathing, or other) may affect the models developed thus far.

A number of heartbeats may be simultaneously plotted as an image by applying an appropriate color mapping to the velocity LDV signals. Two such images are shown in Figure 6.4 for the same individual across two sessions. In each of these figures, 100 heartbeats are shown, with the vertical axis representing the heartbeat number, and the horizontal axis representing the time scale for every heartbeat.

Looking at Figure 6.4, which have the same color maps and pulses aligned, we can see some of the within session variability and the across session variability present in the signals. Both of the figures show variability within session that is approximately periodic, with a period of roughly 5 heartbeats. A similar type of periodicity is

present in many of the subjects we have in our database. Many features can be seen in the first subfigure that contribute to this periodicity. For example, the main peak changes in width and amplitude, and the time location of the trough around 400ms changes. We believe that the main sources for this periodicity are effects due to the breathing cycle and heart rate, which are correlated with each other. Across session, for this subject, we can see various discrepancies and similarities. The stability of the heartbeats across sessions is dependent on the subject.

The effect of state within session should be an important part of a model that describes how the LDV signal changes along the artery. A greater understanding of the phenomenology could lead to simpler and better models. This line of thought has motivated us to study LDV heartbeats using two simultaneous lasers targeted along the carotid, thus providing us with data to use in testing and discovering models that describe the dynamics of the signal. However, in these models, the dependence of state on the heartbeats should be considered. Here, we discuss how the state of each heartbeat might affect the model for the heartbeat.

For our application, we know that some of the assumptions that were necessary to obtain the simplified fluid model may be less suitable than others. For example, the carotid artery is not symmetric about its angular dimension. Determining the level of appropriateness of the above assumptions to our application is an important part of developing this model further. Nonetheless, it is informative to see how state might affect this simple, linear model. If the compliance of the vessel changes as a function of state (for example, breathing state), then the solution to the above model also changes, since the wave speed is affected by the compliance. All of the parameters of the model, in fact, may be a function of state in addition to any other dependencies they may have (time, axial position, etc.).



A good model, therefore, should incorporate the current state into its description of the signal dynamics. This requires an estimate of the state for each heartbeat, given the sequence of heartbeats. Another approach would be to select one state for each individual, and only process heartbeats from this state for the biometric recognition algorithms. Either approach requires state estimation.

We now look at how the model could be used to estimate state within a session. This is one possible approach; however there may be other more suited methods as well. Consider, the heartbeats shown in Figure 6.4. A periodic pattern can be seen by eye, with a period of approximately 5 heartbeats. Certain features in the heartbeats can help to classify the heartbeats into different states, assuming that these features determine the state. For example, the width of the peak at 200 ms and the presence or lack of the peaks at 380 ms and 450 ms can help determine the state of each heartbeat.

We will manually take two heartbeats that are presumably from two different states, and decompose them into a sum of scaled and shifted Gaussian functions. They are shown in blue and red in Figure 6.5. The mean heartbeat across all 100 heartbeats is shown in black. The algorithm was run to optimally (in the mean squared error sense) determine the time locations, amplitudes, and widths of ten Gaussian shaped functions for the three signals shown in Figure 6.5. The resulting modeled signals are shown on the right side of Figure 6.5. It should be noted that more accurate representations of the heartbeats is possible by increasing the number of copies to use in the model, however it seems that ten pulse copies may be enough for the following purpose.

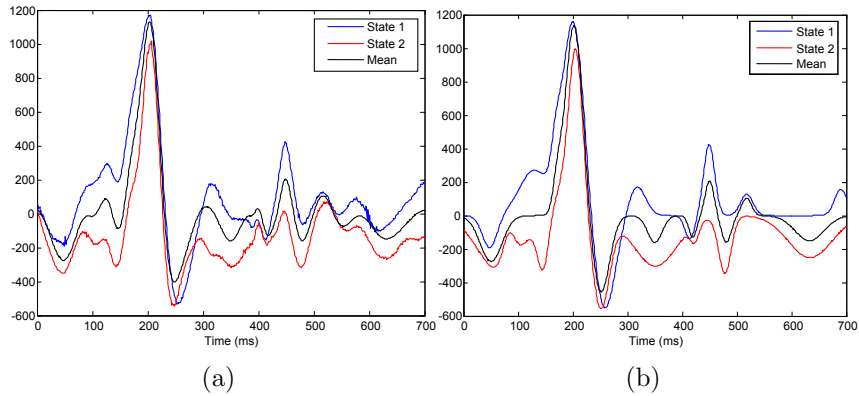
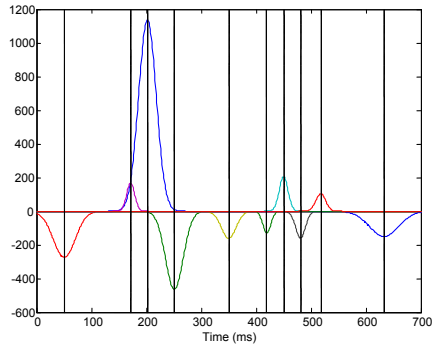


Figure 6.5: Figure (a) shows two pulses from different states, and the the mean pulse. Figure (b) shows the modeled signals from the two states and the mean.

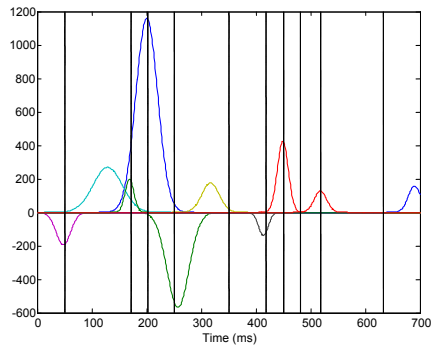
The mean signal is used as a reference to aid in comparing both of the other two heartbeats. Each of the copies for the mean signal are shown in Figure 6.6. The dotted lines show the time locations of each copy of the mean signal, and they are repeated in the same figure for the other two signals. The features mentioned earlier, namely: the width of the peak at 200 ms and the presence of the peaks at 450 ms and 510 ms are captured by this technique. This representation of the signal seems to be informative for the estimation of state of the heartbeat. Also, the copies can be used to model the dynamics of the heartbeats. It could also be beneficial to use the same signal representation for different related tasks.

### 6.3.3 Adjustments for Widening

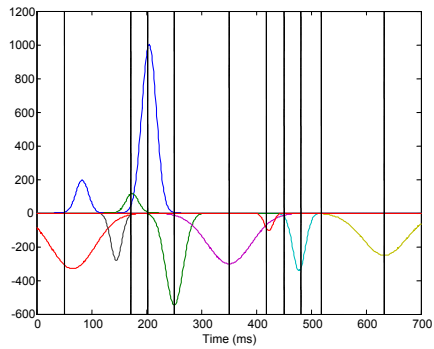
Contrary to the above model, a pressure wave may change not only in amplitude, but also in shape as it is reflected [75]. According to Nichols, et al. [75], the reflected wave is widened; this is thought to be due to dispersion effects of the blood. Figure 6.7 shows three examples of LDV displacement signals in which the initial and primary reflection waves show clearly distinct peaks (Nichols, et al. [75] also pick out the initial



(a)



(b)



(c)

Figure 6.6: Model estimates for (a) the mean pulse, (b) state 1, and (c) state 2.

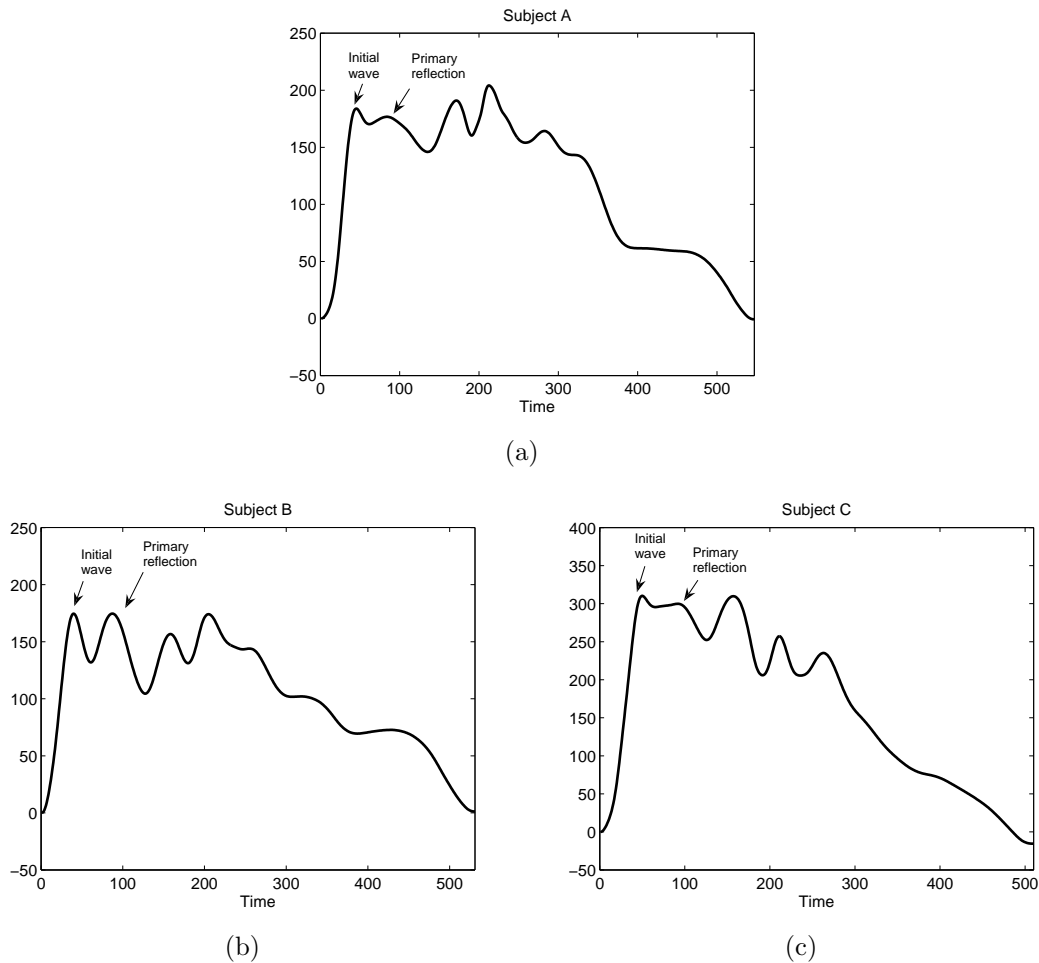


Figure 6.7: Examples of LDV displacement pulses.

reflection by eye). We also observe the widening effect- especially in the primary reflection, suggesting that the LDV pulse is directly related to the underlying blood pressure for these individuals. In other cases, the initial and primary reflection waves have merged into one peaks, likely caused by a wave velocity that is too high for them to be separated.

Figure 6.8 shows results of models that also accommodate for changing widths in the copies for the three examples of Figure 6.7. The initial part of the signal (roughly 50 ms) is used to initialize the input waveform, since during this time there likely

have not been any reflections yet. Here we use a Gaussian point spread function on each reflection to widen and smooth each copy. Each copy uses three parameters: the amplitude, time location, and the full width half maximum of the point spread function. Additionally, the input waveform must be specified.

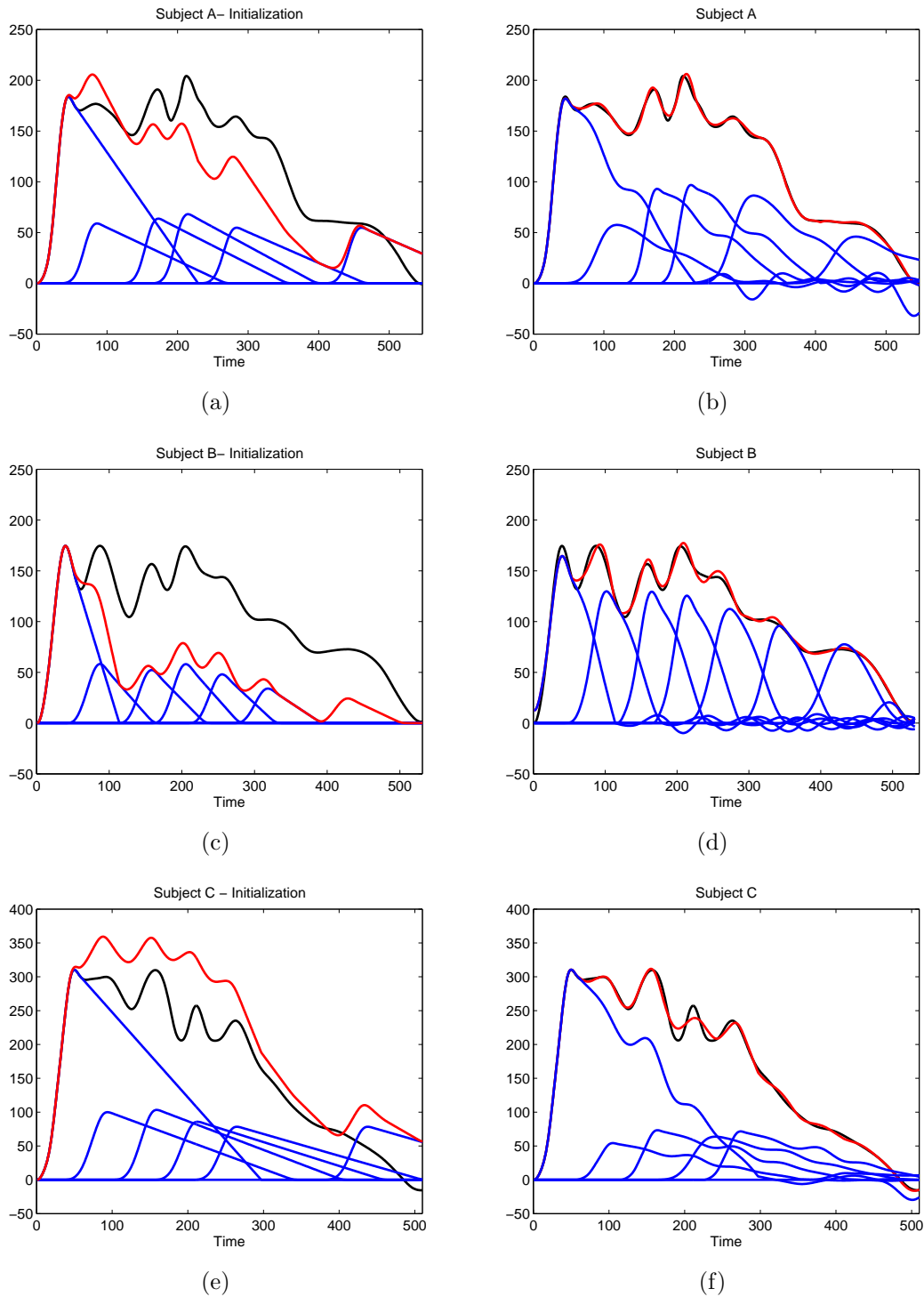


Figure 6.8: Initializations and final converged results of the algorithm for three subjects. The black curves are LDV data, the blue curves are individual waves, and the red curves are the sum of the individual waves.

# Chapter 7

## Identity Verification Using Laser Doppler Vibrometry

Identity recognition is an important and difficult security problem. Information, called an identity marker, is collected from an individual and used to access the identity of that individual at a later time, when the true identity is unknown. The initial phase, called the training phase, when the true identity is assumed to be known, may occur on one or several occasions. The goal is to design a system which can process the identity marker and make decisions about the identity of the individual.

More specifically, in the problem of identity verification, the system must either accept, resulting in a match decision, or reject, resulting in a nonmatch decision, the claimed identity of an individual. In this chapter, we assume that every individual is in the database, but this is not required, and a third decision may be made corresponding to this situation. A different, but related problem is that of identification, in which no identity is claimed. The system must determine the identity of the individual solely on the basis of the identity marker. This type of recognition is not considered in this work.

Generally, characteristics of a good identify marker include: robustness, distinctiveness, availability, and acceptability [2]. Robustness is the property that the measurements do not change over time, distinctiveness is the variety of the data within the population, availability is the ability and ease of data acquisition, and acceptability refers to the individual's consent to being measured (see Wayman, et al [2] for more details). These properties, and experimental verification and recognition error rates, are typically used to assess the utility of a specific biometric.

Different identity markers have differing levels of dependence on physiology. Some, including fingerprint, iris, and face, are not dependent on crucial physiological parameters. Others (for example, speaker verification) are more affected by both short term and long term changes in the human body. From the perspective of robustness, a deeper dependence on physiological traits is a drawback since human physiology is highly dynamic. However, physiologically dependent biometrics have several advantages over ones that are not affected by physiological factors:

1. They are difficult to counterfeit, because they are related to crucial body function.
2. They are of almost certain liveness. The existence of the biometric marker can be guaranteed.
3. They may provide useful supplementary information relating to factors such as stress and health in addition to information used principally for identity verification and recognition.

A major disadvantage of physiological methods is that they will often be dependent on many internal factors, which may or may not be directly measured. In addition,



the nature of this dependence may be complex or unknown. If the data being acquired have short term variations (i.e. changes within the course of a single measurement session), then a sequence of observations may be necessary to capture this variation.

This chapter describes the use of the LDV signal for identity verification, using the models developed in Chapters 3 and 5. Long term cross session variations of this signal have been addressed in Lai et al [78]. A related measurement, the electrocardiogram, has been recently proposed for biometrics [7, 79], however the methods discussed in this paper are based on mechanical effects, not electrical ones. Graphical models have been applied to ID verification problems in written signature [80, 81], keystroke [82], and gait recognition [83].

## 7.1 Motivation

The two fundamental traits of an identity marker are stability and discriminability. Stability refers to the trait that the marker remains constant over time, and discriminability refers to the differences in the marker for different individuals. The stability aspect may be evaluated using the results developed in Chapter 5, in which each model was tested on data from the same individual with varying training and testing schemes. It was shown that some individuals performed well across sessions with respect to the models, while other individuals did not perform as well. Thus, the stability is individual specific.

The notion of stability and discriminability may be defined relative to specific models. Indeed, the main objective of designing a model based ID verification system

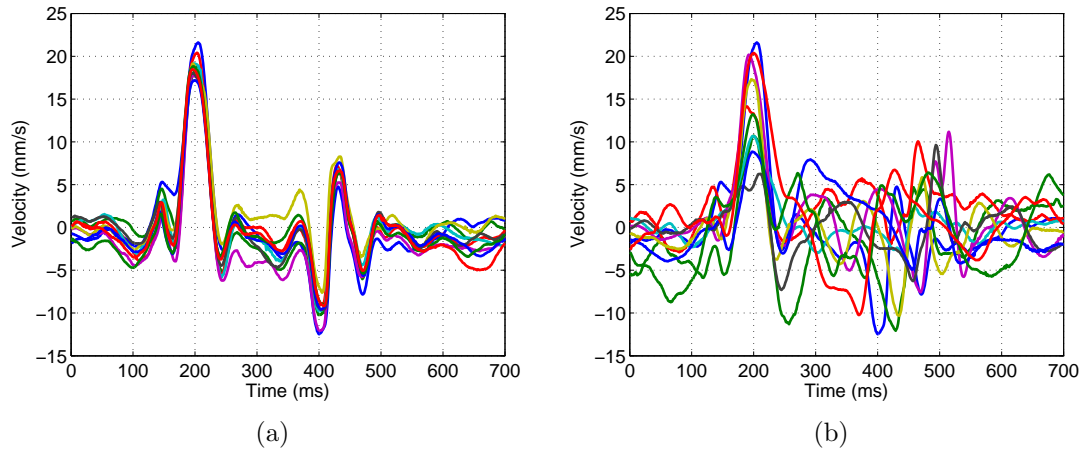


Figure 7.1: An example of stability within session (a), and discriminability across individuals, (b). The pulses are aligned by their main peaks.

is choosing the appropriate models. This may be done with respect to the underlying phenomenology, or dictated by experimentally verifying certain models. Model  $LDV_A$ , for example, indicated that the signal has a strong level of stability. However, it is also true that the discriminability is poor with respect to this model, thus ID verification will not perform well using  $LDV_A$ .

Discriminability is more difficult to access experimentally, because we need to compare combinations of training a model on an individual, and testing on another individual. Before systematically addressing this important issue in terms of recognition performance, we look at an example of stability and discriminability. Figure 7.1 shows ten consecutive pulses from one individual, and single pulses from ten different individuals. From this figure, it seems as though there may be enough discriminability to perform identity verification using the LDV. Thus, the results from Chapter 5 are relevant for this application.

## 7.2 System Design and Performance Prediction

The system is designed using a training phase, which may include multiple sessions. During this phase, one model is trained for each individual in the database. In addition to the individual models, a null model is also trained. This model represents the average individual, and is used for score normalization purposes. After the training phase is complete, the system is ready for operation, where an individual will claim a certain identity  $s$ . The system then computes a score according to,

$$g(\mathbf{y}, s) = \log f(\mathbf{y}|\boldsymbol{\theta}_s) - \log f(\mathbf{y}|\boldsymbol{\theta}_0). \quad (7.1)$$

This is the loglikelihood ratio between the claimed model with parameters  $\boldsymbol{\theta}_s$  and the null model with parameters  $\boldsymbol{\theta}_0$ . This score is then compared to a threshold,  $\tau$ , for the decision [84],

$$d(\mathbf{y}, s, \tau) = \begin{cases} 0, & g(\mathbf{y}, s) < \tau, \\ 1, & g(\mathbf{y}, s) \geq \tau, \end{cases} \quad (7.2)$$

where a 0 corresponds to a nonmatch decision and a 1 corresponds to match decision. The system is completely specified by the models (which include any preprocessing that may be needed), and the threshold.

### 7.2.1 Error Rates

When evaluating a recognition system, we compute empirical False NonMatch Rate (FNMR) and False Match Rates (FMR). In addition to these values, we would also like to have an idea of how accurate these rates are for the target population in the form of confidence intervals. The FNMR is the probability that an incorrect decision

is made when the query is truthful,

$$r_n = \Pr(d(\mathbf{y}, s, \tau) = 0 | s = s^*), \quad (7.3)$$

where  $s^*$  denotes the true identity. The FMR is the probability that an incorrect decision is made when the query is untruthful,

$$r_m = \Pr(d(\mathbf{y}, s, \tau) = 1 | s \neq s^*), \quad (7.4)$$

These error rates are estimated using experimental data by simulating the two cases:  $s = s^*$  and  $s \neq s^*$ . The experimental data consists of two data sets for each individual,

$$\tilde{\mathbf{y}}^{(s)} : \quad \text{training data for subject } s, \quad (7.5)$$

$$\mathbf{y}^{(s)} : \quad \text{testing data for subject } s. \quad (7.6)$$

Let  $N$  be the total number of individuals in the data set, and the score matrix is an  $N \times N$  matrix whose  $(i, j)$  entry is,

$$P_{i,j} = g(\mathbf{y}^{(i)}, j). \quad (7.7)$$

The decision matrix is a binary matrix of the same size that contains the decisions,

$$D_{i,j} = d(\mathbf{y}^{(i)}, j, \tau). \quad (7.8)$$

Thus, each entry in  $D$  is the system's decision for the simulated case where individual  $i$  claims to be individual  $j$ . The FNMR is estimated from the diagonal entries of  $D$

by counting the number of times that a true identity claim was rejected,

$$\hat{r}_n = \frac{1}{N} \sum_{s=1}^N (1 - D_{s,s}). \quad (7.9)$$

The FMR is estimated from the off-diagonal entries of  $D$  by counting the number of times that a false identity claim was accepted,

$$\hat{r}_m = \frac{1}{N^2 - N} \sum_{\substack{i,j \\ i \neq j}}^N D_{i,j}. \quad (7.10)$$

Note that there are significantly more tests involved in the computation of  $\hat{r}_m$  than  $\hat{r}_n$ . Both of these error rates may be viewed as functions of the threshold. The following properties hold true for  $\hat{r}_n(\tau)$  and  $\hat{r}_m(\tau)$ :

1.  $\hat{r}_n(\tau)$  is a nondecreasing function, and  $\hat{r}_m(\tau)$  is a nonincreasing function,
2.  $\hat{r}_n(\tau)$  and  $\hat{r}_m(\tau)$  are bounded below by 0 and bounded above by 1,
3. There exists a threshold  $\tau_{min}$  for which  $\hat{r}_n(\tau) = 0$  and  $\hat{r}_m(\tau) = 1$ ,
4. There exists a threshold  $\tau_{max}$  for which  $\hat{r}_n(\tau) = 1$  and  $\hat{r}_m(\tau) = 0$ .

For a given threshold, estimates of the two error types are computed. By sweeping the threshold and computing these estimates at every value of the threshold, we may obtain performance curves that show the tradeoff between the FNMR and FMR. One point of interest on these curves is the Equal Error Rate (EER). This is the error rate for which  $\hat{r}_n(\tau_{EER}) = \hat{r}_m(\tau_{EER}) \equiv \hat{r}_{EER}$ . Since  $\hat{r}_n(\tau)$  and  $\hat{r}_m(\tau)$  are computed by stepping the threshold through a discrete range of values,  $\tau_{EER}$  will not be one of the thresholds computed. Instead, linear interpolation between the thresholds

surrounding  $\tau_{EER}$  is used to approximate  $\hat{r}_{EER}$ . This improves as the number of discrete values for which the threshold is swept through increases.

## 7.2.2 Confidence Intervals

While we evaluate our recognition systems on a relatively small test sample of individuals, we would like to characterize their performance on a different (likely larger) target population. This is a difficult task without any further information on the target population. If the test population is independent of the target population, then we cannot gain any information on the target population. However this is not likely the case for us, since we have a wide variety of individuals in our database, covering many demographic and health brackets. We need to make assumptions about the relationship between the target and test populations, and draw clear statistical conclusions about the target population.

Now we would like to gain an understanding of how the error rates change as a function of the test population size,  $N$ . This will enable us to characterize the performance of our recognition system on a larger population, perhaps of size  $2N$ ,  $10N$ , or  $100N$ . We write  $\hat{r}_n(N)$  and  $\hat{r}_m(N)$  to emphasize the dependence on population size for a fixed threshold. In this report we will use a method for computing confidence intervals on the error rates following closely the analysis used in the paper by Schuckers [85]. The essential point of that paper is that we can compute the variance of the empirical error rates given certain assumptions about correlations between the recognition system outputs,  $D_{i,j}$ . This requires treating  $D_{i,j}$  as a random variable. Both variances  $Var(\hat{r}_n(N))$  and  $Var(\hat{r}_m(N))$  will be shown to approach 0 as the

test population size increases. Confidence intervals are computed in a straightforward manner under the additional assumption that  $\hat{r}_n(N)$  and  $\hat{r}_m(N)$  are normally distributed. Other methods for computing confidence intervals include bootstrapping [86] and nonparametric density estimation [87, 88, 89].

We use the following covariance structure for  $D_{i,j}$ :

$$Cov(D_{i,j}, D_{i',j'}) = \begin{cases} \sigma_n^2, & i = j = i' = j', \\ \sigma_m^2, & i = i' \neq j = j', \\ \rho, & i \neq j, i' \neq j', (i, j, i', j') \text{ share at least one common value,} \\ 0, & \text{otherwise.} \end{cases} \quad (7.11)$$

The “false nonmatch variance”,  $\sigma_n^2$ , represents the variability in the recognition system output when testing and training on the same individual. The assumption here is that this number is the same for every individual. Similarly, the “false match variance”,  $\sigma_m^2$ , represents the variability in the recognition system output when testing and training on different individuals. This value is the same for all pairs of different individuals. Finally, the “false match covariance”,  $\rho$ , is a measure of the covariance between two tests, each one using testing and training data from different individuals, where at least one individual’s data is used in both tests. See Table 7.1 for a summary of Equation 4. Note that each of the three parameters cannot be greater than 0.25. The covariance structure can be made more complicated if desired. In Schuckers [85], a total of 8 parameters are used. The method of estimating these parameters, as outlined below, remains the same.

We compute sample estimates of the covariance parameters  $\sigma_n^2, \sigma_m^2, \rho$  from the test population by averaging over the corresponding pairs of tests (see Table 7.1). For  $\sigma_n^2$ ,

$i$	$j$	$i'$	$j'$	$Cov(D_{i,j}, D_{i',j'})$
$a$	$a$	$a$	$a$	$\sigma_n^2$
$a$	$a$	$b$	$b$	0
$a$	$b$	$a$	$b$	$\sigma_m^2$
$a$	$b$	$a$	$c$	$\rho$
$a$	$b$	$b$	$a$	$\rho$
$a$	$b$	$b$	$c$	$\rho$
$a$	$b$	$c$	$a$	$\rho$
$a$	$b$	$c$	$b$	$\rho$
$a$	$b$	$c$	$d$	0

Table 7.1: All possible covariances between tests. The indices  $a, b, c, d$  are distinct.

we average over all  $N$  pairs of tests such that all of the training and testing data are from the same individual to get,

$$\hat{\sigma}_n^2 = \frac{1}{N-1} \sum_s (D_{s,s} - \hat{\mu}_n)^2, \quad (7.12)$$

where,

$$\hat{\mu}_n = \frac{1}{N} \sum_s D_{s,s}. \quad (7.13)$$

Similarly, we have,

$$\hat{\sigma}_m^2 = \frac{1}{N^2 - N - 1} \sum_{\substack{i,j \\ i \neq j}} (D_{i,j} - \hat{\mu}_m)^2, \quad (7.14)$$

where,

$$\hat{\mu}_m = \frac{1}{N^2 - N} \sum_{\substack{i,j \\ i \neq j}} D_{i,j}. \quad (7.15)$$

The main difficulty in computing  $\rho$  is counting how many pairs we have that match the criterion for this covariance. Let us first define an indicator function,  $R(i, j, i', j')$ , whose arguments are indices. This function is defined to be 1 when the arguments



meet the criterion for  $\rho$  defined in Table 3, and is 0 otherwise. We have,

$$\hat{\rho} = \frac{1}{\sum_{i,j,i',j'} R(i,j,i',j') - 1} \sum_{i,j,i',j'} R(i,j,i',j') (D_{i,j} - \hat{\mu}_m) (D_{i',j'} - \hat{\mu}_m). \quad (7.16)$$

The number of cases where  $R(i,j,i',j') = 1$  is equal to  $(N^2 - N)(4N - 7)$ . Now we compute the variance of the empirical false nonmatch rate,

$$\text{Var}(\hat{r}_n(N)) = \text{Var}\left(\frac{1}{N} \sum_{s=1}^N (1 - D_{s,s})\right) \quad (7.17)$$

$$= \frac{1}{N^2} \sum_{i,j} \text{Cov}(D_{i,i}, D_{j,j}) \quad (7.18)$$

$$= \frac{\sigma_n^2}{N}. \quad (7.19)$$

We see that the variance approaches 0 with increasing population size,  $N$ . The rate of this decrease is controlled by  $\sigma_n^2$ . The variance of the empirical false match rate is,

$$\text{Var}(\hat{r}_m(N)) = \text{Var}\left(\frac{1}{N^2 - N} \sum_{\substack{i,j \\ i \neq j}}^N D_{i,j}\right) \quad (7.20)$$

$$= \frac{1}{(N^2 - N)^2} \sum_{\substack{i,j \\ i \neq j}} \sum_{\substack{i',j' \\ i' \neq j'}} \text{Cov}(D_{i,j}, D_{i',j'}) \quad (7.21)$$

$$= \frac{\sigma_m^2 + \rho(4N - 7)}{N^2 - N}. \quad (7.22)$$

Now the role of  $\rho$  can be interpreted. Setting  $\rho = 0$  is equivalent to assuming that the  $N^2 - N$  tests used in computing  $\hat{r}_m$  are independent. Otherwise,  $\rho$  represents the correlation between false match tests involving the same individual. We plug in the sample estimates into these equations to compute the sample error rate variances.

Then, we can compute 95% confidence intervals as,

$$\hat{r}_n \pm \frac{2\hat{\sigma}_n}{\sqrt{N}}, \quad (7.23)$$

$$\hat{r}_m \pm \frac{2\sqrt{\hat{\sigma}_m + \hat{\rho}(4N - 7)}}{\sqrt{N^2 - N}}. \quad (7.24)$$

### 7.2.3 LDV

The same models that were developed in Chapter 5 may be used for the ID verification problem, with the same training and testing schedules. This time, however, the testing data will be used to predict the performance of an ID verification system using the models trained on the training data. The results from Chapter 5 are useful in this domain as well, where we are primarily interested in three scenarios:

- Performance within session (schedules  $S_{1,1}$ ,  $S_{2,2}$ ,  $S_{3,3}$ ),
- Performance across sessions, training on one session (schedules  $S_{1,2}$ ,  $S_{1,3}$ ,  $S_{2,3}$ ),
- Performance across sessions, training on two sessions (schedule  $S_{12,3}$ ).

The cases of training on multiple sessions, and testing within session are not of great interest for this problem, since the performance is quite good within session training on one session. Also, as shown in Chapter 5, the model fit does not improve on average in this scenario. In this chapter, we consider the  $LDV_B$  and  $LDB_{BD}$  models. In addition to these models, we use describe a cepstral based HMM system.

The sequence of steps that are performed to generate performance curves are:

1. Train one model each each individual using the training data,

2. Train the null model,
3. Compute the score matrix  $P$  from Equation 7.7,
4. Sweep through the threshold  $\tau$ ,
  - (a) Compute the decision matrix  $D(\tau)$  from Equation 7.8,
  - (b) Compute the error rate estimates,  $\hat{r}_n(\tau)$  and  $\hat{r}_m(\tau)$ ,
  - (c) Compute a 95% confidence interval using Equations 7.23 and 7.24,
5. Compute the EER.

### 7.3 Models $LDV_B$ and $LDV_{BD}$

In model  $LDV_B$ , each pulse is assumed to be drawn from a Gaussian distribution with independent components. Model  $LDV_{BD}$  adds transitions from pulse to pulse, which are primarily due to the breathing cycle during resting conditions. These models are tested for use in an ID verification system, resulting in a prediction of performance. From a physiological point of view, the hypotheses being tested are:

1.  $LDV_B$ : *The morphology of the carotid pulse, as captured over several heart beats using the LDV, contains information related to the functioning of the heart and cardiovascular system, and is of rich enough detail to provide a basis for ID verification.*
2.  $LDV_{BD}$ : *The morphology of the carotid pulse and the dynamics due to breathing and other short term effects, as captured over several heart beats using the LDV,*

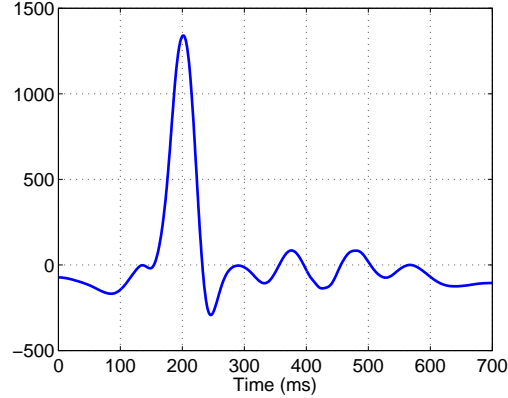


Figure 7.2: The grand mean LDV pulse used in the null model.

*contains information related to the functioning of the heart and cardiovascular system, and is of rich enough detail to provide a basis for ID verification.*

Quantitative answers are provided through experimental tests, and the results are interpreted in terms of empirical error rates and confidence intervals. The results may also be considered with respect to a specific application. This may entail computing the error rate trade-off at specific points other than the EER.

The null model used for these tests is a grand average pulse model B, from Chapter 3. The grand mean that is used in this model is shown in Figure 7.2.

The resulting EERs within session are 1% or less, but performance degrades as we test across sessions. Performance curves for  $LDV_B - S_{1,1}$ ,  $LDV_B - S_{1,2}$ , and  $LDV_B - S_{12,3}$  are given in Figure 7.3. The decreasing curves are the FMR estimates, and the increasing curves are the FNMR estimates. Note that the FMR are smooth compared to the FNMR curves. This is due to the increased sample size from which they are computed.

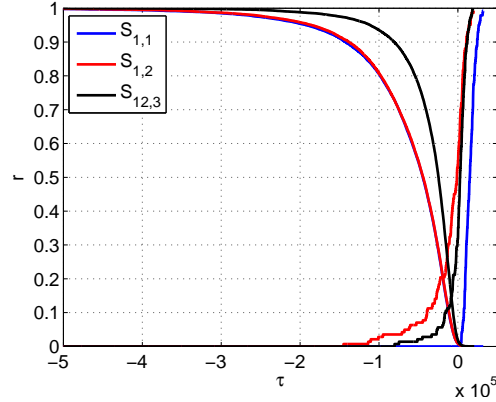


Figure 7.3: Empirical FNMR and FMR curves for the  $LDV_B - S_{1,1}$ ,  $LDV_B - S_{1,2}$ , and  $LDV_B - S_{12,3}$  systems.

From this figure, we can evaluate how the stability and discriminability changes with respect to the three cases outlined in Section 7.2.3. Namely, the within session, across sessions training on one session, and the across sessions training on two sessions performance. The two FMR curves from  $S_{1,1}$  and  $S_{1,2}$  are nearly overlapping. This indicates that the level of discriminability has not changed from session 1 to session 2. The degradation in performance comes entirely from the FNMR curve shifting to the left. This indicates that the stability has decreased, as expected from the results in Chapter 5. The FNMR curve from  $S_{12,3}$  is in between the FNMR curves from  $S_{1,1}$  and  $S_{1,2}$ . Thus, the stability has improved by training on an additional session. Also, the FMR curve has shifted to the right, indicating that the discriminability has decreased by training on two sessions. There is a tradeoff between stability and discriminability that becomes apparent when examining these curves.

More detailed error curves are shown in Figure 7.4 for the same scenarios. Confidence intervals were computed for 20 values of the threshold, and they are shown as bands in the figure in dashed black lines. The bands widen towards the middle of the curves and become narrow towards the ends. Of course, at the endpoints, where

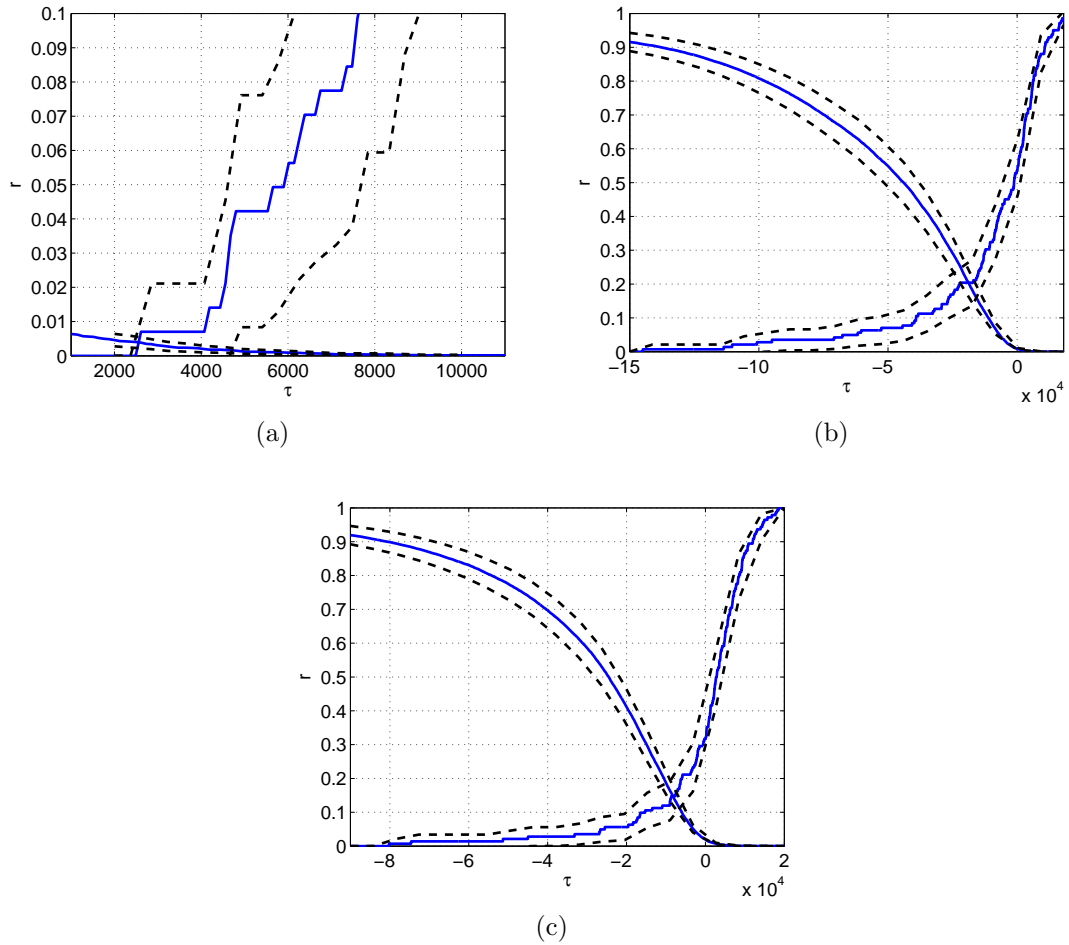


Figure 7.4: Performance curves with 95% confidence bands for model (a)  $LDV_B - S_{1,1}$ , (b)  $LDV_B - S_{1,2}$ , and (c)  $LDV_B - S_{12,3}$ .

$r_n = 0, r_{m=1} = 1$  and  $r_n = 1, r_{m=1} = 0$ , the confidence bands have no width. In the zone where the confidence bands intersect, an EER confidence region appears. For both the  $LDV_B$  and  $LDV_{BD}$  systems, this zone ranges approximately 5% above and below the computed EER when testing across sessions. When testing within session, the zone is much narrower and spans approximately 0.5%.

Table 7.2 shows the empirical EERs for all 11 schedules. Training on session 1, we see that testing on session 2 performs better than testing on session 3. This may be due

Model	$S_{1,1}$	$S_{1,2}$	$S_{1,3}$	$S_{2,2}$	$S_{2,3}$	$S_{3,3}$	$S_{12,2}$	$S_{12,3}$	$S_{13,3}$	$S_{23,3}$	$S_{123,3}$
$LDV_B$	>0.00	0.20	0.25	0.01	0.22	>0.00	0.03	0.15	0.02	0.02	0.04
$LDV_{BD}$	>0.00	0.21	0.27	0.01	0.24	0.01	0.02	0.19	0.01	0.01	0.02

Table 7.2: Empirical equal error rates for models  $LDV_B$  and  $LDV_{BD}$  over the 11 training and testing schedules.

to the longer gap between training and testing sessions. More data is necessary to determine the cause precisely. From Table 7.2, model  $LDV_{BD}$  performs better than  $LDV_B$  within session, except for session 3. Across sessions, model  $LDV_B$  performs better. FNMR and FMR curves for model  $LDV_{BD}$  are presented in Figure 7.5. The additional information captured by model  $LDV_{BD}$  helps to uniquely identify each individual. However, across sessions, this model is too detailed for use in ID verification. When breathing patterns change across sessions, the model interprets this as an indication that the data are from a different individual.

In screening applications, we may not be as interested in the EER as in low FMR operation points. The purpose of a screening is to quickly reduce the total number of people that need to undergo additional verification. It is important in this application that the probability that someone is untruthful about his/her identity is not passed through to the next stage. This may be a useful technique in public places with high volumes of people, where it is known beforehand that most of the people are truthful about their identity. Table 7.3 shows the FNMRs for FMRs of 1%, 0.5% and 0.1% on across session tests. Training on a single session, we may reduce the number of people that go to the next stage by approximately 20%. At an FMR of 1%, almost half of the people will not need to go through additional screening. The table also shows performance for the  $S_{12,3}$  schedule.

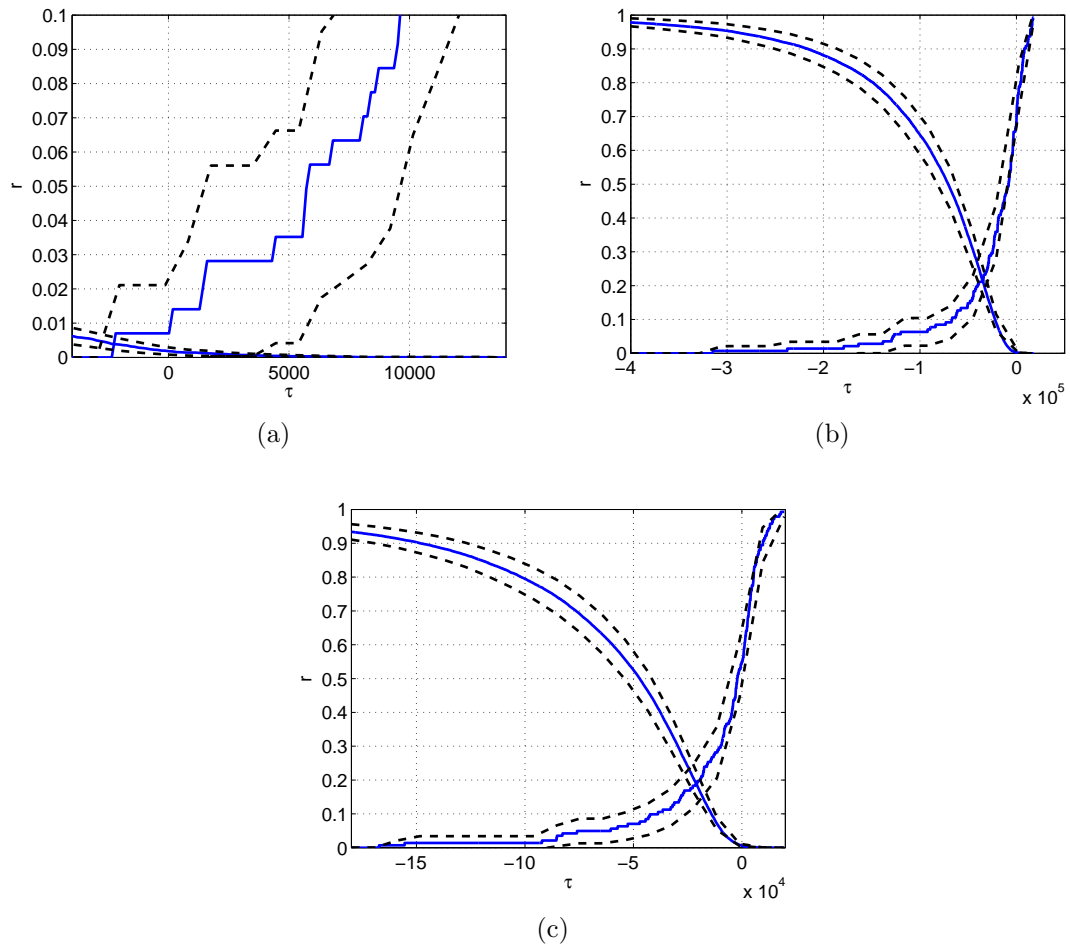


Figure 7.5: Performance curves with 95% confidence bands for model (a)  $LDV_{BD} - S_{1,1}$ , (b)  $LDV_{BD} - S_{1,2}$ , and (c)  $LDV_{BD} - S_{12,3}$ .

	1%	0.5%	0.1%
$LDV_B - S_{1,2}$	53%	61%	80%
$LDV_B - S_{12,3}$	42%	54%	78%
$LDV_{BD} - S_{1,2}$	54%	66%	79%
$LDV_{BD} - S_{12,3}$	51%	56%	82%

Table 7.3: FNMRs for set FMRs of 1%, 0.05%, and 0.01%.



## 7.4 Cepstral HMM

### 7.4.1 Background

STFT representations of the LDV data have been used for ID verification with the LDV [58, 90], using a similar system design. In these methods, the log magnitude STFT is performed on each pulse using a Hamming window of length 96 ms, and an overlap of 80 ms. A template,  $c$ , is computed by averaging the log magnitude STFT matrices across the training pulses for each individual. During testing, the following score is computed for each testing pulse,  $b$ ,

$$g = - \sum_{i,j} (c(i,j) - b(i,j))^2 - (c(i,j) - b_0(i,j))^2, \quad (7.25)$$

where  $b_0$  is a null spectrogram. If multiple testing pulses are used, then the mean of their scores is used. This score is then compared to a threshold for the decision. It was found that the performance was steady after four testing pulses. Across sessions, the estimated EER was 11%. Several additional improvements were made to this system, including:

- Training on two sessions,
- Informative component selection,
- Separating the pulse into two portions based on the incisura location.

After these improvements, the across sessions EER was lowered to 6%. See the paper by Chen [90] for more details.

Signal variability is a major issue in speaker recognition [91], and in recognition based on LDV data. Spectral features [92], and the combination of HMMs with spectral features [91, 93, 94] has been found to be useful to combat this variability in speaker recognition. Among the 15 methods and papers surveyed by Campbell [93], none published before 1991 use HMMs and all published after 1991 do, showing the prevalence of HMMs for speaker recognition in more recent years. The success of these models in speaker recognition provides a motivation to pursue similar methods for LDV data.

The STFT has also been successful in applications of speech recognition. In those systems, a HMM is used on a modified STFT called cepstral coefficients. Within each window, the cepstrum is computed instead of the magnitude FFT. Several definitions of the cepstral coefficients exist. The one that is used here is,

$$\mathcal{F}^{-1} \{ \log (|\mathcal{F} \{ \mathbf{y} \}|) \}. \quad (7.26)$$

The system presented in this section use cepstral coefficients combined with an HMM (model  $LDV_{BD}$ ).

## 7.4.2 Results

Here we describe some results using a cepstral based HMM for LDV. Within each pulse we compute cepstral coefficients in a sliding Hamming window with 50% overlap. Five window lengths are considered: 700ms, 350ms, 175ms, 70ms, and 35ms. The models are trained on session 1, and tested on session 2, and the scored are normalized using a null model that represents the average individual. Keeping the number of states

Window length	Time bins per pulse	EER (%)	95% FNMR	FNMR overlap	95% FMR	FMR overlap
700 ms	1	14.41	[8.55, 20.27]	39%	[12.20, 16.62]	1%
350 ms	3	13.33	[7.60, 19.07]	43%	[11.44, 15.23]	3%
175 ms	7	11.27	[5.94, 16.59]	-	[9.79, 12.74]	-
70 ms	19	12.68	[7.07, 18.28]	45%	[10.79, 14.56]	9%
35 ms	39	16.90	[10.59, 23.21]	32%	[13.66, 20.15]	2%

Table 7.4: Equal error rates with varying window lengths and 2 states. Also, 95% confidence intervals are given for the false nonmatch and false match rates. The overlap indicates the probability of the error rate being lower than that of the best performing model with a window length of 175ms.

constant (2 states), the models with 175ms length windows resulted in the lowest EER of 11.27% (see Table 7.4). Then, keeping the window length constant at 175ms, we vary the number of states, from 1 to 5 (models with 1 state assume that the pulses are independent). From this experiment, the best performing model is one with 3 states, resulting in an EER of 10.04% (see Table 7.5).

Also included in Tables 7.4 and 7.5 are 95% confidence intervals on the error rates, along with the probability that each error rate is less than the best performing model's error rate in that group (we call this the overlap). This helps us to decide if one model should be preferred to another model. If the overlap is large, then the performance between the two models cannot be distinguished. If the overlap is small, then the model with the lower error rate should be preferred.

The confidence intervals for the false nonmatch rate (FNMR) are wider than those for the false match rate (FMR). Generally, this is because there are more tests involved in determining the FMR than the FNMR. As described later in this report, correlations

Number of states	EER (%)	95% FNMR	FNMR overlap	95% FMR	FMR overlap
1	10.56	[5.39, 15.74]	48%	[9.12, 12.01]	23%
2	11.27	[5.94, 16.59]	45%	[9.79, 12.74]	5%
3	10.04	[5.02, 15.06]	-	[8.65, 11.43]	-
4	10.88	[5.70, 16.06]	46%	[9.42, 12.34]	12%
5	11.43	[6.10, 16.76]	44%	[9.89, 12.97]	4%

Table 7.5: Equal error rates with varying number of states using a window length of 175ms. Also, 95% confidence intervals are given for the false nonmatch and false match rates. The overlap indicates the probability of the error rate being lower than that of the best performing model with 3 states.

between false matches widen the FMR confidence interval. Consulting with Tables 7.4 and 7.5, we see that the overlap percentage of the FNMR is too large to help us decide between the models; instead we will use the FMR to help use decide between the models. In Table 7.4, we see that none of the overlaps are greater than 10%. This leads us to have high confidence that the 175ms is best among those considered, at least for the FMR. In Table 7.5, we see significant overlap among the FMR as well as the FNMR, so we do not claim to decide the best number of states. Figure 7.6 shows the performance curves for the best performing model, along with the confidence bands.

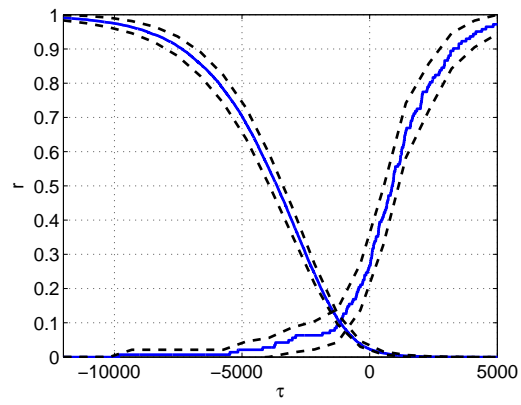


Figure 7.6: The performance curves for the cepstral HMM and 95% confidence bands.

# Chapter 8

## Conclusions and Future Work

Biological signals are often indirect measurements of desired quantities. Using these types of signals either for clinical applications or security applications may require the use of empirically tested models. A commonality between many biological signals is they are semi-periodic, and dependent on the state of the individual. The models that were developed in this dissertation are designed to track the state of the individual. Doing so requires an appropriate time frame to consider variability in the signal.

An LDV system was used as a novel method for sensing cardiovascular activity through mechanical movements of the skin surface overlying the carotid. Models for the pulse and models that incorporated state changes across pulses were evaluated on three sessions of data. The fit of the pulse models decreased as tests were made across sessions. This is due to longer term state changes that were occurring in the individual, although for some individuals, the pulses did not show great variability across sessions. Models that include transitions from pulse to pulse generally track the breathing phase when trained under resting conditions. These models performed better than the pulse models within session, but worse across sessions. This is due

to the added changes in breathing patterns that may be occurring across sessions. Within session, the breathing patterns were fairly constant.

Models were also trained across multiple sessions of data. Training Gaussian models using two sessions effectively averages the pulses across those sessions. These models performed better than models that treated each session as a separate state. This is because there were not enough long term states to accurately predict future sessions. An interesting question is to determine whether adding more sessions will improve these models.

In the log-magnitude STFT domain, models were constructed to include short term variability in the LDV pulse. These models utilize a left to right state topology in which each pulse must transition from the first state to the last state, passing through all states in between. Considering other topologies that allow for skipping states is a possible future direction. These models were used to segment raw sequences of LDV signals by determining when the final states were reached for each pulse.

The LDV signal is related to the underlying physics of blood flow. This line of analysis was explored within the fluid dynamics of elastic tubes. Under certain assumptions of symmetry and wave properties, the resulting pressure wave follows a one dimensional wave equation. Additional assumptions are necessary to relate the skin displacement to the carotid's radius, which in term is nearly proportional to the underlying pressure. Testing these assumptions is an area of future work. Under experimental settings, the LDV displacement pulse is representative of typical blood pressure waveforms.

Modeling the LDV pulses in the STFT domain holds the greatest promise for ID verification using the LDV. An HMM was used to models changes across pulses. Similar models are used for speech recognition problems. An EER of 10% was obtained

training on one session using a three state HMM. From the work of Chen [58] on this problem, an EER of 11% was obtained by training on one session using a lognormal model of STFT coefficients. Splitting the pulse into two parts, the first centered on the main peak, and the second centered on the incisura dropped the EER down to 9%. Training on two sessions reduced the EER to 6%. Similar methods may improve performance on the HMM models as well.

Reporting confidence levels is especially important when sample sizes are small. Confidence was reported using a correlation method that does not assume that all tests are independent. Only tests involving different individuals are assumed independent. Using this method, a 95% confidence range of approximately  $\pm 5\%$  was computed. This number seems to be roughly equivalent for all of the methods that were attempted.

## **8.1 Future Work**

### **8.1.1 Modeling for LDV and Biological Signals**

The models that were explored in this dissertation were shown to track physiologically relevant states within a pulse and across pulses. However, the multisession models that treat each session as a separate state did not yield interesting results, other than to point out that there were not enough sessions for data driven modeling of long term state effects. If more sessions were recorded, would it be possible to develop models that track long term state changes? This may be experimentally performed through shorter intervals between sessions, perhaps daily or a few times a day. Learning the signal variability with such a data set would prove invaluable for clinical and security



applications. Also, this may enable models to be built for specific clinical conditions across individuals.

The number of states used in the graphical models was manually selected based on our physiological understanding of the underlying dynamics. Since the data were recorded from individuals at rest, this was a satisfying choice. There may be other dynamics which we do not expect, however, especially in non-resting conditions. One approach to selecting the number of states could be to implement a penalized loglikelihood. The penalty could be linear in the number of states, as suggested by the Bayesian Information Criterion [95, 96].

HMMs are versatile models. The hidden Markov chain may be constructed of higher order, but a higher order Markov chain can always be made equivalent to a first order Markov chain by expanding the state space. The Gaussian model for the observed variables given the hidden state has been experimentally shown to be useful for the LDV signal, but a different model may also be beneficial. One example is the learning of a tree structure for each pulse. The Chow and Liu algorithm [97] gives a consistent algorithm for learning the structure of a tree when the true distribution is a tree by computing pairs of sample mutual information. These pairs are then used as the weights in a maximum-weight spanning tree problem. This algorithm may be used on the LDV pulse to potentially uncover interesting patterns within a pulse.

### **8.1.2 Underlying Physics of LDV Signals**

In this work, the link between the LDV signal and the blood pressure in the carotid was explored. This is an important aspect of the development of this technology for clinical use, and perhaps for security applications as well. There is a large body of

work on the physiological function of the cardiovascular system, which can be accessed if this link is well understood.

One possible step could be to design a simulation of the LDV pulse based on physical parameters, such as the heart rate, and elasticity of the carotid walls. Then, models may be estimated on the simulated data initially. The simulated data may also be compared to the real data to see if the models are realistic.

The assumptions that were presented in this work have not been tested. Some of them are more reasonable than others, but this may be tested in a number of ways. Simulated data may be generated by controlling which assumptions are relaxed, and then compared with real data. Another possible direction could be to measure the blood pressure simultaneously, possibly on animals.

### **8.1.3 ID Verification Using the LDV**

The LDV may be especially useful in pre-screening applications. This requires a different operating point for the system, other than that which produces the EER. A systematic assessment of the system sensitivity to threshold changes would be beneficial to this application. Systems that do not require pulse segmentation would also be beneficial, since errors that are made in pulse extraction will propagate to the system decision.

Assessing a wider variety of subject conditions, including varying postures is also important for this problem. All of the data used in this dissertation were made from the seated position, but the standing position may cause significant changes in the signal. Also, the data may be recorded while the subjects are walking. In addition,

the data were recorded using a piece of reflective tape. Analyzing the performance using LDV signals collected directly from the skin is important future work.

Another direction for future work is to address the dependence of the proposed ID verification system on the state of the individual. Perhaps controlling for heart rate or blood pressure may improve performance. This may be experimentally quantified by classifying the subjects according to state before evaluating system performance.

# Appendix A

## Fluid Dynamics

The Navier-Stokes equations are derived from the conservation of mass and a set of constitutive equations. This derivation follows along the lines of Zamir [57].

### A.1 Conservation of Mass

Cylindrical coordinates are a natural choice for this problem, since the tubes will be approximated as cylinders. The three axes: axial, radial, and angular are represented by the symbols:  $x$ ,  $r$ ,  $\theta$ . Components of a velocity vector in the cylindrical space are represented by the corresponding symbols:  $u$ ,  $v$ ,  $w$ . The volume of an arbitrary volume element with infinitesimal dimensions ( $\delta x$ ,  $\delta r$ ,  $\delta\theta$ ) located at a radial distance of  $r$  is,

$$V = (\pi (r + \delta r)^2 - \pi r^2) \frac{\delta\theta}{2\pi} \delta x = \pi (r^2 + 2r\delta r + \delta r^2 - r^2) \frac{\delta\theta}{2\pi} \delta x \approx r \delta r \delta\theta \delta x.$$

The mass of this volume is equal to its volume multiplied by its density:  $M = \rho V$ . Since, in general, the density is a function of time, the partial derivative of the mass

with respect to time is:  $\frac{\partial M}{\partial t} = \frac{\partial \rho}{\partial t} r \delta x \delta r \delta \theta$ . Without going into the details, applying conservation of mass by balancing the flow of mass in and out of each dimension of the volume element gives,

$$-\left(\frac{\partial(\rho u)}{\partial x} + \frac{\partial(\rho v)}{\partial r} + \frac{\rho v}{r} + \frac{1}{r} \frac{\partial(\rho w)}{\partial \theta}\right) r \delta \theta \delta r \delta x \approx \frac{\partial \rho}{\partial t} r \delta \theta \delta r \delta x.$$

As the infinitesimal dimensions approach a point,

$$\frac{\partial \rho}{\partial t} + \frac{\partial(\rho u)}{\partial x} + \frac{\partial(\rho v)}{\partial r} + \frac{\rho v}{r} + \frac{1}{r} \frac{\partial(\rho w)}{\partial \theta} = 0.$$

Making the assumption that the density is constant in space and time:  $\frac{\partial \rho}{\partial t} = 0$ ,  $\frac{\partial \rho}{\partial x} = 0$ ,  $\frac{\partial \rho}{\partial r} = 0$ ,  $\frac{\partial \rho}{\partial \theta} = 0$ ,

$$\frac{\partial u}{\partial x} + \frac{\partial v}{\partial r} + \frac{\rho v}{r} + \frac{1}{r} \frac{\partial w}{\partial \theta} = 0. \quad (\text{A.1})$$

Equation A.1 is the equation of conservation of mass that will be used in this analysis.

## A.2 Navier-Stokes Equations in Cylindrical Coordinates

Newton's second law of motion, for each dimension in cylindrical coordinates is,

$$m a_x = F_x,$$

$$m a_r = F_r,$$

$$ma_\theta = F_\theta.$$

Here,  $a_x$ ,  $a_r$ ,  $a_\theta$  are components of an acceleration vector, and  $F_x$ ,  $F_r$ ,  $F_\theta$  are components of an applied force vector. Dividing both sides by the volume ( $V$ ) gives,

$$\rho a_x = f_x,$$

$$\rho a_r = f_r,$$

$$\rho a_\theta = f_\theta,$$

The right-hand side is now in units of force per unit volume,  $f_x = \frac{F_x}{V}$ ,  $f_r = \frac{F_r}{V}$ ,  $f_\theta = \frac{F_\theta}{V}$ . The acceleration components are equal to the derivative of corresponding velocity components with respect to time together with terms that take into account the curvature of the geometry,

$$a_x = \frac{Du}{Dt} = \frac{\partial u}{\partial t} + u \frac{\partial u}{\partial x} + v \frac{\partial u}{\partial r} + \frac{w}{r} \frac{\partial u}{\partial \theta},$$

$$a_r = \frac{Dv}{Dt} - \frac{w^2}{r} = \frac{\partial v}{\partial t} + u \frac{\partial v}{\partial x} + v \frac{\partial v}{\partial r} + \frac{w}{r} \frac{\partial v}{\partial \theta} - \frac{w^2}{r},$$

$$a_\theta = \frac{Dw}{Dt} - \frac{vw}{r} = \frac{\partial w}{\partial t} + u \frac{\partial w}{\partial x} + v \frac{\partial w}{\partial r} + \frac{w}{r} \frac{\partial w}{\partial \theta} - \frac{vw}{r},$$

The forces per unit volume ( $f_x$ ,  $f_r$ ,  $f_\theta$ ) are expressed in terms of nine stresses

$$\tau_{x\theta}, \tau_{xr}, \sigma_{xx}, \tau_{r\theta}, \sigma_{rr}, \tau_{rx}, \sigma_{\theta\theta}, \tau_{\theta x}, \tau_{\theta r},$$

three that act on each of the three dimensions. They are not discussed in detail here for the sake of brevity, but their relationship to the forces are given by,

$$f_x = \frac{\partial \sigma_{xx}}{\partial x} + \frac{\partial \tau_{xx}}{\partial r} + \frac{\tau_{rx}}{r} + \frac{1}{r} \frac{\partial \tau_{\theta x}}{\partial \theta},$$

$$f_r = \frac{\partial \tau_{xr}}{\partial x} + \frac{\partial \sigma_{rr}}{\partial r} + \frac{\sigma_{rr}}{r} + \frac{1}{r} \frac{\partial \tau_{\theta r}}{\partial \theta},$$

$$f_\theta = \frac{\partial \tau_{x\theta}}{\partial x} + \frac{\partial \tau_{r\theta}}{\partial r} + \frac{\tau_{r\theta}}{r} + \frac{1}{r} \frac{\partial \sigma_{\theta\theta}}{\partial \theta}.$$

This formulation is in terms of stresses, which are difficult to measure in practice. We would like to find a relationship between the stresses and the pressure field to derive a more practical model. A set of empirically derived equations, the “constitutive equations”, are used for this purpose, which formulate a linear relationship between the stresses and the pressure, involving partial derivatives of the velocity components. They are given by,

$$\sigma_{xx} = -p + 2\mu \frac{\partial u}{\partial x},$$

$$\sigma_{rr} = -p + 2\mu \frac{\partial v}{\partial r},$$

$$\sigma_{\theta\theta} = -p + 2\mu \left( \frac{1}{r} \frac{\partial w}{\partial \theta} + \frac{v}{r} \right),$$

$$\tau_{xr} = \tau_{rx} = \mu \left( \frac{\partial u}{\partial r} + \frac{\partial v}{\partial x} \right),$$

$$\tau_{x\theta} = \tau_{\theta x} = \mu \left( \frac{\partial w}{\partial x} + \frac{1}{r} \frac{\partial u}{\partial \theta} \right),$$

$$\tau_{r\theta} = \tau_{\theta r} = \mu \left( \frac{\partial w}{\partial r} - \frac{w}{r} + \frac{1}{r} \frac{\partial v}{\partial \theta} \right).$$

In these equations, the pressure field is denoted by  $p$ . When the velocity components are equal to zero, the pressure satisfies  $-p = \sigma_{xx} = \sigma_{rr} = \sigma_{\theta\theta}$ . When the velocity

components are not equal to zero, then the following is assumed:  $p = -\frac{\sigma_{xx} + \sigma_{rr} + \sigma_{\theta\theta}}{3}$ . Combining the equations for the components of acceleration and the equations for the forces into Newton's second law of motion gives the Navier-Stokes equations in cylindrical coordinates,

$$\rho \left( \frac{\partial u}{\partial t} + u \frac{\partial u}{\partial x} + v \frac{\partial u}{\partial r} + \frac{w}{r} \frac{\partial u}{\partial \theta} \right) + \frac{\partial p}{\partial x} = \mu \left( \frac{\partial^2 u}{\partial x^2} + \frac{\partial^2 u}{\partial r^2} + \frac{1}{r} \frac{\partial u}{\partial r} + \frac{1}{r^2} \frac{\partial^2 u}{\partial \theta^2} \right), \quad (\text{A.2})$$

$$\rho \left( \frac{\partial v}{\partial t} + u \frac{\partial v}{\partial x} + v \frac{\partial v}{\partial r} + \frac{w}{r} \frac{\partial v}{\partial \theta} - \frac{w^2}{r} \right) + \frac{\partial p}{\partial r} = \quad (\text{A.3})$$

$$\mu \left( \frac{\partial^2 v}{\partial x^2} + \frac{\partial^2 v}{\partial r^2} + \frac{1}{r} \frac{\partial v}{\partial r} - \frac{v}{r^2} + \frac{1}{r^2} \frac{\partial^2 v}{\partial \theta^2} - \frac{2}{r^2} \frac{\partial w}{\partial \theta} \right),$$

$$\rho \left( \frac{\partial w}{\partial t} + u \frac{\partial w}{\partial x} + v \frac{\partial w}{\partial r} + \frac{w}{r} \frac{\partial w}{\partial \theta} + \frac{vw}{r} \right) + \frac{1}{r} \frac{\partial p}{\partial \theta} = \quad (\text{A.4})$$

$$\mu \left( \frac{\partial^2 w}{\partial x^2} + \frac{\partial^2 w}{\partial r^2} + \frac{1}{r} \frac{\partial w}{\partial r} - \frac{w}{r^2} + \frac{1}{r^2} \frac{\partial^2 w}{\partial \theta^2} + \frac{2}{r^2} \frac{\partial v}{\partial \theta} \right).$$

These equations together with the equation of conservation of mass (Equation A.1) provide the governing equations for the most general case of fluid flow in cylindrical coordinates.



# Bibliography

- [1] R. A. Fisher, “The biometric society,” *Biometrics*, vol. 4, pp. 216–219, 1948.
- [2] J. Wayman, A. Jain, D. Maltoni, and D. Maio, *Biometric Systems: Technology, Design and Performance Evaluation*. Springer-Verlag, 2005.
- [3] R. P. Wildes, “Iris recognition: An emerging biometric technology,” *Proceedings of the IEEE*, vol. 85, pp. 1348–1363, 1997.
- [4] K. W. Bowyer, K. Hollingsworth, and P. J. Flynn, “Image understanding for iris biometrics: A survey,” *Computer Vision and Image Understanding*, vol. 110, pp. 281–307, 2008.
- [5] K. W. Bowyer, S. E. Baker, A. Hentz, K. Hollingsworth, T. Peters, and P. J. Flynn, “Factors that degrade the match distribution in iris biometrics,” in *Identity in the Information Society*, Springer, 2009.
- [6] S. E. Baker, K. W. Bowyer, and P. J. Flynn, “Empirical evidence for correct iris match score degradation with increased time-lapse between gallery and probe matches,” in *Advances in Biometrics*, Springer, 2009.
- [7] S. Israel, J. Irvine, A. Cheng, M. Wiederhold, and B. Wiederhold, “ECG to identify individuals,” *Pattern Recognition*, vol. 38, no. 1, pp. 133–142, 2005.
- [8] L. Biel, O. Pettersson, L. Philipson, and P. Wide, “ECG analysis: A new approach in human identification,” *IEEE Transactions on Instrumentation and Measurement*, vol. 50, pp. 808–812, 2001.
- [9] G. Wubbeler, M. Stavridis, D. Kreiseler, R.-D. Boussejot, and C. Elster, “Verification of humans using the electrocardiogram,” *Pattern Recognition*, vol. 28, pp. 1172–1175, 2007.
- [10] K. Phua, J. Chen, T. H. Dat, and L. Shue, “Heart sound as a biometric,” *Pattern Recognition*, vol. 41, pp. 906–919, 2008.

- [11] M. J. Wainwright and M. I. Jordan, “Graphical models, exponential families, and variational inference,” *Foundations and Trends in Machine Learning*, vol. 1, pp. 1–305, 2008.
- [12] S. L. Lauritzen, *Graphical Models*. Oxford University Press, 1996.
- [13] M. I. Jordan, *Learning in Graphical Models*. The MIT Press, 1998.
- [14] L. R. Bahl, J. Cocke, F. Jelinek, and J. Raviv, “Optimal decoding of linear codes for minimizing symbol error rate,” *IEEE Transactions on Information Theory*, vol. 20, pp. 284–287, 1974.
- [15] R. G. Gallager, *Low-Density Parity Check Codes*. MIT Press, 1963.
- [16] R. J. McEliece, D. J. C. McKay, and J. F. Cheng, “Turbo decoding as an instance of pearl’s belief propagation algorithm,” *IEEE Journal on Selected Areas in Communications*, vol. 16, pp. 140–152, 1998.
- [17] R. Durbin, S. R. Eddy, A. Krogh, and G. Mitchison, *Biological Sequence Analysis*. Cambridge University Press, 1999.
- [18] H. Nielson, S. Brunak, and G. von Heijne, “Machine learning approaches for the prediction of signal peptides and other protein signals,” *Protein Engineering*, vol. 12, pp. 3–9, 1999.
- [19] B. H. Juang and L. R. Rabiner, “Hidden Markov Models for Speech Recognition,” *Technometrics*, vol. 33, no. 3, pp. 251–272, 1991.
- [20] S. Renals, N. Morgan, H. Bourlard, M. Cohen, and H. Franco, “Connectionist probability estimators in hmm speech recognition,” *IEEE Transactions on Speech and Audio Processing*, vol. 2, pp. 161–174, 1994.
- [21] B. Juang, W. Chou, and C. Lee, “Minimum classification error rate methods for speech recognition,” *IEEE Transactions on Speech and Audio Processing*, vol. 5, pp. 257–265, 1997.
- [22] F. Jelinek, L. R. Bahl, and R. L. Mercer, “Design of a linguistic statistical decoder for the recognition of continuous speech,” *IEEE Transactions on Information Theory*, vol. 21, pp. 250–256, 1975.

- [23] G. R. Cross and A. K. Jain, "Markov random field texture models," *IEEE Transactions on Pattern Analysis and Machine Intelligence*, vol. PAMI-5, pp. 25–39, 1983.
- [24] S. Geman and D. Geman, "Stochastic relaxation, gibbs distributions, and the bayesian restoration of images," *IEEE Transactions on Pattern Analysis and Machine Intelligence*, vol. 6, pp. 721–741, 1984.
- [25] M. Hassner and J. Sklansky, "The use of markov random fields as models of texture," *Computer Graphics and Image Processing*, vol. 12, pp. 357–370, 1980.
- [26] J. Woods, "Markov image modeling," *Automatic Control, IEEE Transactions on*, vol. 23, pp. 846 – 850, Oct. 1978.
- [27] X. Liao, P. Runkle, and L. Carin, "Identification of ground targets from sequential high-range-resolution radar signatures," *IEEE Transactions on Aerospace and Electronic Systems*, vol. 38, no. 4, pp. 1230–1242, 2002.
- [28] P. Runkle, L. Carin, and L. Nguyen, "Multi-aspect target classification using hidden Markov models for data fusion," *IEEE Transactions on Signal Processing*, pp. 2123–2125, 2000.
- [29] P. Runkle, L. H. Nguyen, J. H. McClellan, and L. Carin, "Multi-Aspect Target Detection for SAR Imagery Using Hidden Markov Models," *IEEE Transactions on Geoscience and Remote Sensing*, 2001.
- [30] R. Andreao and B. Dorizzi, "ECG Signal Analysis Through Hidden Markov Models," *IEEE Transactions on Biomedical Engineering*, vol. 53, no. 8, pp. 1541–1549, 2006.
- [31] D. A. Caost, R. M. Stern, G. G. Cano, and S. A. Brillier, "An approach to cardiac arrhythmia analysis using hidden markov models," *IEEE Transactions on Biomedical Engineering*, vol. 37, pp. 826–836, 1990.
- [32] F. Kschischang, B. Frey, and H. Loeliger, "Factor graphs and the sum-product algorithm," *Information Theory, IEEE Transactions on*, vol. 47, no. 2, pp. 498–519, 2001.
- [33] S. Aji and R. McEliece, "The generalized distributive law," *Information Theory, IEEE Transactions on*, vol. 46, no. 2, pp. 325–343, 2000.

- [34] M. J. Wainwright, *Stochastic Processes on Graphs with Cycles: Geometric and Variational Approaches*. PhD thesis, Massachusetts Institute of Technology, 2002.
- [35] J. Besag, “Spatial interaction and the statistical analysis of lattice systems,” *Journal of the Royal Statistical Society. Series B (Methodological)*, vol. 36, pp. 192–236, 1974.
- [36] G. R. Grimmett, “A theorem about random fields,” *Bulletin of the London Mathematical Society*, vol. 84, pp. 5–81, 1973.
- [37] L. R. Rabiner, “A tutorial on hidden markov models and selected applications in speech recognition,” *Proceedings of the IEEE*, vol. 77, pp. 257–286, 1989.
- [38] A. J. Viterbi, “Error bounds for convolutional codes and an asymptotically optimum decoding algorithm,” *IEEE Transactions on Information Theory*, vol. IT-13, pp. 260–269, 1967.
- [39] G. D. Forney, “The viterbi algorithm,” *Proceedings of the IEEE*, vol. 61, pp. 268–278, 1973.
- [40] M. Wainwright, T. Jaakkola, and A. Willsky, “Tree consistency and bounds on the performance of the max-product algorithm and its generalizations,” *Statistics and Computing*, vol. 14, pp. 143–166, 2004.
- [41] F. C. Hoppensteadt and C. S. Peskin, *Modeling and Simulation in Medicine and the Life Sciences*. Springer, 2000.
- [42] T. L. Johnson, S. C. Wright, and A. Segall, “Filtering of muscle artifact from the electroencephalogram,” *Biomedical Engineering, IEEE Transactions on*, vol. BME-26, no. 10, pp. 556–563, 1979.
- [43] C. Meyer and H. Keiser, “Electrocardiogram baseline noise estimation and removal using cubic splines and state-space computation techniques,” *Computers and Biomedical Research*, vol. 10, no. 5, pp. 459–470, 1977.
- [44] L. Sornmo and P. Laguna, *Biological Signal Processing in Cardiac and Neurological Applications*. Elsevier Academic Press, 2005.

- [45] “Recent advances in heart rate variability signal processing and interpretation,” *IEEE Transactions on Biomedical Engineering, special issue.*, vol. 53, pp. 1–143, 2006.
- [46] A. P. Dempster, N. M. Laird, and D. B. Rubin, “Maximum likelihood from incomplete data via the EM algorithm,” *Journal of the Royal Statistical Society. Series B (Methodological)*, vol. 39, pp. 1–38, 1977.
- [47] L. E. Baum, T. Petrie, G. Soules, and N. Weiss, “A maximization technique occurring in the statistical analysis of probabilistic functions of markov chains,” *The Annals of Mathematical Statistics*, vol. 41, pp. 164–171, 1970.
- [48] M. D. Stern, “In vivo evaluation of microcirculation by coherent light scattering,” *Nature*, vol. 254, pp. 56–58, 1975.
- [49] A. P. Shepherd and G. L. Riedel, “Continuous Measurement of Intestinal Mucosal Blood Flow by Laser-Doppler Velocimetry,” *American Journal of Physiology - Gastrointestinal and Liver Physiology*, vol. 242, no. 6, pp. 668–672, 1982.
- [50] R. Maniewski, E. Szuffadowicz, A. Nosek, and F. Walczak, “Laser Doppler Method in Evaluation of Vasovagal Syncope Induced by Tilt Table Test,” in *Proceedings of the 26th Annual International Conference of the IEEE EMBS*, pp. 2315–2317, 2004.
- [51] A. Stefanovska, M. Bracic, and H. D. Kvernmo, “Wavelet Analysis of Oscillations in the Peripheral Blood Circulation Measured by Laser,” *IEEE Transactions on Biomedical Engineering*, vol. 46, no. 10, pp. 1230–1239, 1999.
- [52] N. Stasche, H.-J. Foth, K. Hormann, A. Baker, and C. Huthoff, “Middle Ear Transmission Disorders- Tympanic Membrane Vibration Analysis by Laser-Doppler-Vibrometry,” *Acta Oto-laryngologica*, vol. 114, no. 1, pp. 59–63, 1994.
- [53] K. R. Whittemore, S. N. Merchant, B. B. Poon, and J. J. Rosowski, “A normative study of tympanic membrane motion in humans using a laser doppler vibrometer (ldv),” *Hearing Research*, vol. 187, pp. 85–104, 2004.
- [54] A. L. Nuttall, D. F. Dolan, and G. Avinash, “Laser Doppler Velocimetry of Basilar Membrane Vibration,” *Hearing Research*, vol. 51, pp. 203–214, 1991.

- [55] H. Hong and M. Fox, “Noninvasive detection of cardiovascular pulsations by optical doppler techniques,” *Journal of Biomedical Optics*, vol. 2, pp. 382–390, 1997.
- [56] U. Morbiducci, L. Scalise, M. D. Melis, and M. Grigioni, “Optical vibrocardiography: A novel tool for the optical monitoring of cardiac activity,” *Annals of Biomedical Engineering*, vol. 35, pp. 45–58, 2007.
- [57] M. Zamir, *The Physics of Pulsatile Flow*. Springer, 2000.
- [58] M. Chen, *Laser Doppler Vibrometry Measures of Physiological Function: Evaluation of Biometric Capabilities*. PhD thesis, Washington University in St. Louis, 2009.
- [59] A. Vander, J. Sherman, and D. Luciano, *Human Physiology: The Mechanics of Body Function*. McGraw-Hill, 2001.
- [60] R. M. Berne and M. N. Levy, *Cardiovascular Physiology*. The C.V. Mosby Company, 1981.
- [61] M. Sugawara, K. Niki, H. Furuhashi, S. Ohnishi, and S. Suzuki, “Relationship between the pressure and diameter of the carotid artery in humans,” *Heart Vessels*, vol. 15, pp. 49–51, 2000.
- [62] D. J. Patel, D. P. Schilder, and A. J. Mallos, “Mechanical properties and dimensions of the major pulmonary arteries,” *J Appl Physiol*, vol. 15, no. 1, pp. 92–96, 1960.
- [63] S. H. Nawab, T. F. Quatieri, and J. S. Lim, “Signal reconstruction from short-time fourier transform magnitude,” *IEEE Transactions on Acoustics, Speech and Signal Processing*, vol. ASSP-31, pp. 986–998, 1983.
- [64] A. D. Kaplan, J. A. O’Sullivan, E. J. Sirevaag, S. D. Kristjansson, P.-H. Lai, and J. W. Rohrbaugh, “Hidden state dynamics in laser doppler vibrometry measurements of the carotid pulse under resting conditions,” in *IEEE International Conference of the Engineering in Medicine and Biology Society*, (Buenos Aires, Argentina), 2010.
- [65] P. S. Nandi, V. M. Pigott, and D. H. Spodick, “Sequential Cardiac Responses during the Respiratory Cycle: Patterns of Change in Systolic Intervals,” *Chest*, vol. 63, pp. 380–385, 1973.

- [66] K. Karlocai, G. Jokkel, and M. Kollai, “Changes in left ventricular contractility with the phase of respiration,” *Journal of the Autonomic Nervous System*, vol. 73, pp. 86–92, 1998.
- [67] M. J. Drinnan, J. Allen, and A. Murray, “Relation between heart rate and pulse transit time during paced respiration,” *Physiological Measurement*, vol. 22, pp. 425–432, 2001.
- [68] P. V. Leeuwen and H. C. Keummell, “Respiratory modulation of cardiac time intervals,” *British Heart Journal*, vol. 58, pp. 129–135, 1987.
- [69] A. Johansson, C. A. T. Lanne, and P. Ask, “Pulse wave transit time for monitoring respiration rate,” *Medical and Biological Engineering and Computing*, vol. 44, pp. 471–478, 2006.
- [70] N. Westerhof, N. Stergiopoulos, and M. Noble, *Snapshots of hemodynamics: an aid for clinical research and graduate education*. Springer, 2005.
- [71] D. Berger, J. K. Li, W. K. Laskey, and A. Noordergraaf, “Repeated reflection of waves in the systemic arterial system,” *Am J Physiol Heart Circ Physiol*, vol. 264, pp. 269–281, 1993.
- [72] F. Pythoud, N. Stergiopoulos, N. Westerhof, and J.-J. Meister, “Method for determining distribution of reflection sites in the arterial system,” *American Journal of Physiology-Heart and Circulatory Physiology*, vol. 271, pp. H1807–H1813, 1996.
- [73] K. B. Campbell, L. C. Lee, H. F. Frasch, and A. Noordergraaf, “Pulse reflection sites and effective length of the arterial system,” *American Journal of Physiology-Heart and Circulatory Physiology*, vol. 256, pp. H1684–H1689, 1989.
- [74] J. Wang and K. H. Parker, “Wave propagation in a model of the arterial circulation,” *Journal of Biomechanics*, vol. 37, pp. 457–470, 2003.
- [75] W. Nichols, F. Michael, and D. McDonald, *McDonald’s blood flow in arteries*. Arnold, 1998.
- [76] J. Meinders and A. Hoeks, “Simultaneous assessment of diameter and pressure waveforms in the carotid artery,” *Ultrasound in Medicine & Biology*, vol. 30, no. 2, pp. 147–154, 2004.

- [77] S. Vermeersch, E. Rietzschel, M. De Buyzere, D. De Bacquer, G. De Backer, L. Van Bortel, T. Gillebert, P. Verdonck, and P. Segers, “Determining carotid artery pressure from scaled diameter waveforms: comparison and validation of calibration techniques in 2026 subjects,” *Physiological Measurement*, vol. 29, no. 11, pp. 1267–1280, 2008.
- [78] P.-H. Lai, J. A. O’Sullivan, M. Chen, E. J. Sirevaag, A. D. Kaplan, and J. W. Rohrbaugh, “A robust feature selection method for noncontact biometrics based on laser doppler vibrometry,” in *Biometrics Symposium 2008*, (Tampa, FL), pp. 65–70, 2008.
- [79] S. Israel, J. Irvine, B. Wiederhold, and M. Wiederhold, “Identification based on fusion of cardiovascular function measurements,” in *Proceedings of SPIE*, 2008.
- [80] D. Muramatsu and T. Matsumoto, “An hmm on-line signature verifier incorporating signature trajectories,” in *Proceedings of the Seventh International Conference on Document Analysis and Recognition (ICDAR03)*, 2003.
- [81] J. Fierrez, J. Ortega-Garcia, D. Ramos, and J. Gonzalez-Rodriguez, “Hmm-based on-line signature verification: feature extraction and signal modeling,” *Pattern Recognition Letters*, vol. 28, pp. 2325–2334, 2007.
- [82] R. N. Rodrigues, G. F. G. Yared, C. R. do N. Costa, J. B. T. Yabu-Uti, F. Violaro, and L. L. Ling, “Biometric access control through numerical keyboards based on keystroke dynamics,” *Lecture Notes on Computer Science*, vol. 3823, pp. 640–646, 2005.
- [83] M. Chen, J. A. O. Sullivan, A. D. Kaplan, P.-H. Lai, E. J. Sirevaag, and J. W. Rohrbaugh, “Biometrics with physical exercise using laser doppler vibrometry measurements of the carotid pulse,” in *IEEE International Conference on Biometrics, Identity and Security 2009*, (Tampa Bay, FL), 2009.
- [84] H. L. V. Trees, *Detection, Estimation, and Modulation Theory: Part 1*. John Wiley & Sons, 2001.
- [85] M. E. Schuckers, “A parametric correlation framework for the statistical evaluation and estimation of biometric-based classification performance in a single environment,” *IEEE Transactions on Information Forensics and Security*, vol. 4, pp. 231–241, 2009.



- [86] R. Bolle, S. Pankanti, and N. K. Ratha, "Error analysis of pattern recognition systems: The subsets bootstrap," *Computer Vision and Image Understanding*, vol. 93, pp. 1–33, 2004.
- [87] J. B. Tilbury, P. W. J. V. Eetvelt, J. M. Garibaldi, J. S. H. Curnow, and E. C. Ifeachor, "Receiver operating characteristic analysis for intelligent medical systems: A new approach for finding confidence intervals," *IEEE Transactions on Biomedical Engineering*, vol. 47, pp. 952–963, 2000.
- [88] J. Kerekes, "Receiver operating characteristic curve confidence intervals and regions," *IEEE Geoscience and Remote Sensing Letters*, vol. 5, pp. 251–255, 2008.
- [89] R. A. Hilgers, "Distribution-free confidence bounds for roc curves," *Methods of Information in Medicine*, vol. 30, pp. 96–101, 1991.
- [90] M. Chen, J. A. O'Sullivan, N. Singla, E. J. Sirevaag, S. D. Kristjansson, P.-H. Lai, A. D. Kaplan, and J. W. Rohrbaugh, "Laser doppler vibrometry measures of physiological function: Evaluation of biometric capabilities," *IEEE Transactions on Information Forensics and Security*, vol. 5, no. 3, pp. 449–460, 2010.
- [91] S. Furui, "An overview of speaker recognition technology," in *Automatic Speech and Speaker Recognition*, Kluwer Academic Publishers, 1996.
- [92] S. Furui, "Cepstral analysis technique for automatic speaker verification," *IEEE Transactions on Acoustics, Speech and Signal Processing*, 1981.
- [93] J. J. P. Campbell, "Speaker recognition: A tutorial," *Proceedings of the IEEE*, 1997.
- [94] K. Yu, J. Mason, and J. Oglesby, "Speaker recognition using hidden markov models, dynamic time warping, and vector quantisation," *IEE Processings- Vision, Image, and Signal Processing*, 1995.
- [95] G. E. Schwarz, "Estimating the dimension of a model," *Annals of Statistics*, vol. 6, pp. 461–464, 1978.
- [96] A. Lanterman, "Schwarz, Wallace, and Rissanen: Intertwining themes in theories of model selection," *International Statistical Review*, vol. 69, no. 2, pp. 185–212, 2001.

- [97] C. K. Chow and C. N. Liu, “Approximating discrete probability distributions with dependence trees,” *IEEE Transactions on Information Theory*, vol. IT-14, pp. 462–467, 1968.

# Vita

Alan D. Kaplan

<b>Date of Birth</b>	March 24, 1983
<b>Place of Birth</b>	Springfield, Illinois
<b>Degrees</b>	B.Sc., Electrical Engineering, University of Illinois, Urbana, Illinois May 2005  M.Sc., Electrical Engineering, Washington University in St. Louis, May 2007  Ph.D., Electrical Engineering, Washington University in St. Louis, May 2011
<b>Affiliations</b>	Institute of Electrical and Electronics Engineers (IEEE)  Society of Industrial and Applied Mathematics (SIAM)  American Association for the Advancement of Science (AAAS)
<b>Certifications</b>	Health Insurance Portability and Accountability Act (HIPAA)
<b>Publications</b>	A. D. Kaplan, J. A. O’Sullivan, E. J. Sirevaag, P.-H. Lai, J. W. Rohrbaugh, “Hidden State Models for Laser Doppler Vibrometry Measurements of the Carotid Pulse,” submitted to <i>IEEE Transactions on Biomedical Engineering</i> .  I. Odinaka, P.-H. Lai, Alan D. Kaplan, J. A. O’Sullivan, E. J. Sirevaag, S. Kristjansson, A. Sheffield, and J. W. Rohrbaugh, “ECG Biometrics: A Robust Short-Time Frequency Analysis,” <i>IEEE WIFS 2010</i> .  I. Odinaka, P.-H. Lai, Alan D. Kaplan, and J. A. O’Sullivan, “On estimating biometric capacity: An example based on LDV biometrics,” <i>Allerton Conference 2010</i> .  A. D. Kaplan, J. A. O’Sullivan, E. J. Sirevaag, S. Kristjansson, and J. W. Rohrbaugh, “Hidden State Dynamics in Laser

Doppler Vibrometry Measurements of the Carotid Pulse Under Resting Conditions,” *IEEE EMBC 2010*.

M. Chen, J. A. O’Sullivan, N. Singla, E. J. Sirevaag, S. Kristjansson, P.-H. Lai, A. D. Kaplan, and J. W. Rohrbaugh, “Laser Doppler Vibrometry Measures of Physiological Function: Evaluation of Biometric Capabilities,” *IEEE Transactions on Information Forensics and Security*, Sep 2010.

M. Chen, J. A. O’Sullivan, A. D. Kaplan, P.-H. Lai, E. J. Sirevaag, and J. W. Rohrbaugh, “Biometrics with Physical Exercise Using Laser Doppler Vibrometry Measurements of the Carotid Pulse,” *IEEE International Conference on Biometrics, Identity and Security 2009*.

A. D. Kaplan, J. A. O’Sullivan, E. J. Sirevaag, and J. W. Rohrbaugh, “Laser Doppler Vibrometry Measurements of the Carotid Pulse: Biometrics Using Hidden Markov Models,” *SPIE DSS 2009*.

P.-H. Lai, J. A. O’Sullivan, M. Chen, E. J. Sirevaag, A. D. Kaplan, and J. W. Rohrbaugh, “A Robust Feature Selection Method for Noncontact Biometrics Based on Laser Doppler Vibrometry,” *Biometrics Symposium 2008*.

May 2011

**Modeling of Biological Signals, Kaplan, Ph.D. 2011**